



UNIVERSIDADE ESTADUAL DE CAMPINAS

Faculdade de Engenharia Química

RICARDO LUIZ FERNANDES OLIVEIRA

BEHAVIOUR OF THE TEMPERATURE FIELD AROUND POOL  
FIRES IN CONTROLLED EXPERIMENT AND NUMERICAL  
MODELLING

COMPORTAMENTO DO CAMPO DE TEMPERATURAS AO  
REDOR DE INCÊNDIOS EM POÇA EM EXPERIMENTOS  
CONTROLADOS E MODELAGEM NUMÉRICA

CAMPINAS

2018

RICARDO LUIZ FERNANDES OLIVEIRA

BEHAVIOUR OF THE TEMPERATURE FIELD AROUND POOL  
FIRES IN CONTROLLED EXPERIMENT AND NUMERICAL  
MODELLING

COMPORTAMENTO DO CAMPO DE TEMPERATURAS AO  
REDOR DE INCÊNDIOS EM POÇA EM EXPERIMENTOS  
CONTROLADOS E MODELAGEM NUMÉRICA

Dissertation presented to the Faculty of  
Chemical Engineering of the University  
of Campinas in partial fulfillment of the  
requirements for the degree of Master in  
Chemical Engineering.

Dissertação apresentada à Faculdade de En-  
genharia Química da Universidade Estadual  
de Campinas como parte dos requisitos para  
a obtenção do título de Mestre em Engen-  
haria Química.

Orientador: Gustavo Doubek

Coorientador: Sávio S. S. Vianna

ESTE EXEMPLAR CORRESPONDE À VERSÃO FINAL  
DA DISSERTAÇÃO DEFENDIDA PELO ALUNO RI-  
CARDO LUIZ FERNANDES OLIVEIRA, E ORIENTADA  
PELO PROF. DR. GUSTAVO DOUBEK.

CAMPINAS

2018

**Agência(s) de fomento e nº(s) de processo(s):** Não se aplica.

**ORCID:** <https://orcid.org/0000-0002-8848-8180>

Ficha catalográfica  
Universidade Estadual de Campinas  
Biblioteca da Área de Engenharia e Arquitetura  
Rose Meire da Silva - CRB 8/5974

OL4b Oliveira, Ricardo Luiz Fernandes, 1986-  
Behaviour of the temperature field around pool fires in controlled experiment and numerical modelling / Ricardo Luiz Fernandes Oliveira. – Campinas, SP : [s.n.], 2018.

Orientador: Gustavo Doubek.

Coorientador: Sávio Souza Venâncio Vianna.

Dissertação (mestrado) – Universidade Estadual de Campinas, Faculdade de Engenharia Química.

1. Fluidodinâmica Computacional (CFD). 2. Produtos Químicos - Incêndios e prevenção de incêndios. 3. Incêndios. I. Doubek, Gustavo, 1984-. II. Vianna, Sávio Souza Venâncio, 1975-. III. Universidade Estadual de Campinas. Faculdade de Engenharia Química. IV. Título.

#### Informações para Biblioteca Digital

**Título em outro idioma:** Comportamento do campo de temperaturas ao redor de incêndios em poça em experimentos controlados e modelagem numérica

**Palavras-chave em inglês:**

Computational Fluid Dynamics (CFD)

Chemicals - Fire and fire prevention

Pool fire

**Área de concentração:** Engenharia Química

**Titulação:** Mestre em Engenharia Química

**Banca examinadora:**

Gustavo Doubek [Orientador]

Carla Neves Costa

José Roberto Nunhez

**Data de defesa:** 05-11-2018

**Programa de Pós-Graduação:** Engenharia Química

Dissertação de mestrado defendida por Ricardo Luiz Fernandes Oliveira e aprovada em 05 de dezembro de 2018 pela banca examinadora constituída pelos doutores:

---

Prof. Dr. Gustavo Doubek – Orientador  
FEQ/UNICAMP

---

Prof. Dr. José Roberto Nunhez  
FEQ/UNICAMP

---

Profa. Dra. Carla Neves Costa  
FEC/UNICAMP

A Ata da defesa com as respectivas assinaturas dos membros encontra-se no SIGA/Sistema de Fluxo de Tese e na Secretaria do Programa da Unidade.

*"The answer, my friend, is blowing in the wind."*

*Bob Dylan*

*To my parents.*

# Acknowledgment

The accomplishment of this work was only possible due to the collaboration of several people, to which I must express my sincere gratitude.

I feel very grateful to have worked with my advisers Prof. Gustavo Doubek and Prof. Sávio Souza Venâncio Vianna. I would like to thank Prof. Sávio for introducing me to the interesting world of process safety engineering. As for Prof. Gustavo, I am grateful for his guidance and encouragement, and mostly for enlightening my discovery of how to build a scientific research WITH all its steps and possibilities.

I thank my fellow labmates in L4r1s4 and LPDC laboratories: Mara, Eder, Juliana, Raphael and Elmo for sharing with me all their experiences and knowledge, which has been essential and invaluable.

To my family, especially my parents Graça and Silvério, for believing in me; encouraging me to go beyond and giving me all the opportunities they could afford. To my siblings Luiza and Eduardo, my nephews João and Miguel, and my aunt Cláudia, I cannot imagine being the person I am today without all their contributions and support.

To my colleagues from Petrobras, I am very grateful for their technical contributions and encouragement, my heavy routine was much lighter with your support.

To my friends from Campinas, Belo Horizonte, and so many other places around the world, they have made the difficult times more bearable and life more joyful and complete.

## RESUMO

A descrição e predição confiáveis de cenários de incêndio tem fundamental importância na engenharia de segurança e análise de riscos. Dentre as ferramentas em CFD disponíveis para simulação de incêndios, o Fire Dynamics Simulator (FDS) tem recebido grande atenção da comunidade de segurança e tem sido utilizado em uma larga gama de aplicações. O presente estudo avalia como o FDS correlaciona com alturas de chama e perfis de temperatura experimentais ao redor de incêndios em poça de pequena escala, com três combustíveis líquidos amplamente utilizados na indústria: hexano comercial, etanol e gasolina tipo C. A avaliação explora as ferramentas disponíveis no FDS tais como a sua biblioteca de substâncias, os modelos de turbulência, o modelo de Pirólise Líquida e as taxas de formação de CO e fuligem, que são testadas e discutidas. Os resultados demonstram que a descrição da gasolina com base na biblioteca de substâncias do FDS gera uma concordância pobre com os perfis de temperatura. Para as simulações com o hexano e o etanol hidratado, mesmo quando a concordância quantitativa com os dados experimentais não é boa, as tendências são bem reproduzidas pelas simulações.

## **ABSTRACT**

Trustful description and prediction of a fire scenario has a major importance in safety engineering and risk analysis. Among the available CFD software for fire simulation, Fire Dynamics Simulator (FDS) has been receiving great attention in the safety community and it has been applied in a broad range of applications. The present study evaluates how FDS correlates with experimental flame heights and temperature profiles around a small scale pool fire, with three liquid fuels largely used in industry: commercial hexane, hydrous ethanol and type C gasoline. The evaluation explores the tools available on FDS such as the software substance library, the turbulence models, the Liquid Pyrolysis Model and the CO and Soot yields, which are tested and discussed. The results demonstrate that the gasoline description based on FDS substance library yields poor agreement with the temperature profiles. For commercial hexane and hydrous ethanol simulations, even when quantitative agreement with experimental data is not good, the trends are well reproduced in the simulations.

# List of Figures

1.1	Chemicals warehouse with drums and IBCs. . . . .	21
2.1	Physical Phenomena in pool fires (Hu, 2017). . . . .	25
2.2	Five-zone flame structure (Venkatesh et al., 1996). . . . .	27
2.3	Comparison of experimentally measured mass fluxes and Hamins' model (Hamins et al., 1999). . . . .	28
2.4	Burning rate stages for thin layer pool fires. . . . .	30
2.5	Illustration of the flame height definition. . . . .	31
2.6	Features of a turbulent fire plume, including axial variations on the centerline (Heskestad, 1984). . . . .	33
2.7	Structure of a diffusion flame in a candle fire (Gottuk & Lattimer, 2016). . . . .	34
2.8	Zones of a diffusion flame (Gottuk & Lattimer, 2016). . . . .	35
2.9	Stress components of a fluid element in the three orthogonal directions (Versteeg & Malalasekera, 1995). . . . .	43
2.10	Energy cascade of turbulent flows. . . . .	45
3.1	Experimental apparatus composed of a scale and a burner inside of a standard fume hood. . . . .	54
3.2	Schematic of the experiment set up considered. . . . .	55
3.3	Sketch of the thermocouple tree. . . . .	57
3.4	Apparatus for flame height measurement. . . . .	59
3.5	Smokeview visualization of the computational domain. . . . .	60
3.6	Comparison of D86 distillation curves (type C Gasoline). . . . .	63
4.1	Experimental mass loss curves for the three fuels (a) hexane, (b) hydrous ethanol, (c) gasoline. . . . .	68

4.2	Experimental mass loss curves for the three fuels (a) hexane, (b) hydrous ethanol, (c) gasoline. . . . .	69
4.3	Experimental MLRPUA curves for the three fuels (a) hexane, (b) hydrous ethanol, (c) gasoline. . . . .	71
4.4	Frames of the hexane fire during the quasi-steady burning period. . . . .	73
4.5	Intermittency curves for the three fuels (a) hexane, (b) hydrous ethanol, (c) gasoline. . . . .	74
4.6	Experimental temperature measurements at positions (a) T002 and (b) T302. . . . .	76
4.7	Process to obtain time-averaged temperatures. . . . .	77
4.8	Temperature standard deviation analysis for (a) hexane, (b) hydrous ethanol and (c) gasoline. . . . .	78
4.9	Mean temperatures for hexane experiments during steady burning period (from $t = 60$ s to $t = 110$ s) - Horizontal profiles. . . . .	80
4.10	Mean temperatures for hexane experiments during steady burning period (from $t = 60$ s to $t = 110$ s) - Vertical profiles. . . . .	81
4.11	Mean temperatures for ethanol experiments during steady burning period (from $t = 120$ s to $t = 200$ s) - Horizontal profiles. . . . .	82
4.12	Mean temperatures for ethanol experiments during steady burning period (from $t = 120$ s to $t = 200$ s) - Vertical profiles. . . . .	83
4.13	Mean temperatures for gasoline experiments during steady burning period (from $t = 70$ s to $t = 120$ s) - Horizontal profiles. . . . .	84
4.14	Mean temperatures for gasoline experiments during steady burning period (from $t = 70$ s to $t = 120$ s) - Vertical profiles. . . . .	85
4.15	Experimental temperature map (hexane). . . . .	87
4.16	Experimental temperature map (hydrous ethanol). . . . .	88
4.17	Experimental temperature map (gasoline). . . . .	89
4.18	Simulated flame heights. . . . .	90
4.19	Comparison of simulated, experimental and Heskestad flame heights (a) hexane, (b) hydrous ethanol, (c) gasoline. . . . .	92
4.20	Time-averaged temperature profiles (hexane). . . . .	94
4.20	Cont. Time-averaged temperature profiles (hexane). . . . .	95
4.21	Time-averaged temperature profiles (hydrous ethanol). . . . .	96

4.21	Cont. Time-averaged temperature profiles (hydrous ethanol). . . . .	97
4.22	Time-averaged temperature profiles (gasoline). . . . .	98
4.22	Cont. Time-averaged temperature profiles (gasoline). . . . .	99
4.23	Time averaged temperature contours at the middle plane of the domain (left side) and experimental (right side) for (a) commercial hexane, (b) hydrous ethanol and (c) type C gasoline. . . . .	100
4.24	Comparison between experimental temperature profiles with the simulated pro- files obtained with zero CO and soot yields and with modelled CO and soot yields (hexane). . . . .	102
4.24	cont. Comparison between experimental temperature profiles with the simulated profiles obtained with zero CO and soot yields and with modelled CO and soot yields (hexane). . . . .	103
4.25	Simulated temperature profiles with three turbulence models: Deardorff (DTM), Smagorinsky (SM) and Dynamic Smagorinsky (DSM). . . . .	104
4.25	cont. Simulated temperature profiles with three turbulence models: Deardorff (DTM), Smagorinsky (SM) and Dynamic Smagorinsky (DSM). . . . .	105
4.26	Comparison of mass loss curves (hexane). . . . .	106
4.27	Mass loss rate per unit area (hexane). . . . .	107
4.28	Comparison between experimental temperature profiles with simulated profiles obtained with the prescribed burning rate model (PBR) and with the liquid pyrolysis model (LPM). . . . .	108
4.28	cont. Comparison between experimental temperature profiles with simulated profiles obtained with the prescribed burning rate model (PBR) and with the liquid pyrolysis model (LPM). . . . .	109
A.1	Average temperature curves for the hexane flame for $X/D=0.0$ . . . . .	118
A.2	Average temperature curves for the hexane flame for (a) $X/D=0.25$ , (b) $X/D=0.50$ and (c) $X/D=0.75$ . . . . .	119
A.3	Average temperature curves for the hexane flame for (d) $X/D=1.00$ , (e) $X/D=1.50$ and (f) $X/D=2.50$ . . . . .	120
A.4	Average temperature curves for the hydrous ethanol flame for (a) $X/D=0.0$ , and (b) $X/D=0.25$ , (b) $X/D=0.50$ . . . . .	121

A.5	Average temperature curves for the hydrous ethanol flame for (a) $X/D=0.75$ , and (b) $X/D=1.00$ , (b) $X/D=1.50$ . . . . .	122
A.6	Average temperature curves for the hydrous ethanol flame for $X/D=2.50$ . . . . .	123
A.7	Average temperature curves for the gasoline flame for (a) $X/D=0.0$ , and (b) $X/D=0.25$ , (b) $X/D=0.50$ . . . . .	124
A.8	Average temperature curves for the gasoline flame for (a) $X/D=0.75$ , and (b) $X/D=1.00$ , (b) $X/D=1.50$ . . . . .	125
A.9	Average temperature curves for the gasoline flame for $X/D=2.50$ . . . . .	126

# List of Tables

2.1	Pool fire burning modes . . . . .	28
2.2	Mass loss rate per unit area for a large pool fire . . . . .	29
3.1	Fuel properties . . . . .	54
3.2	Indexes used for temperature tags . . . . .	58
3.3	Simulation parameters and boundary conditions . . . . .	61
3.4	Modeled gasoline composition. . . . .	63
3.5	Mesh descriptions. . . . .	64
4.1	General results of evaporation measurements . . . . .	71
4.2	Average flame heights and heats of combustion . . . . .	75
4.3	Computational cost . . . . .	90
4.4	Global Temperature Errors (GTE) . . . . .	92
4.5	Computational cost for the simulations with different CO and soot modelling conditions . . . . .	101
4.6	Computational cost for the simulations with different turbulence models . .	105
4.7	GTE, Flame height and Computational cost . . . . .	107

# Nomenclature

$A$  Pool area

$C_s$  Smagorinsky constant

$C_v$  Deardorff constant

$c_v$  Specific heat coefficient at constant volume

$c_p$  Specific heat coefficient at constant pressure

$d$  Pool depth

$D$  Pool Diameter

$D_{l,g}$  Diffusion coefficient

$E$  Energy in the fluid element

$E_i$  Internal energy

$Err_i$  Error between experimental and simulated temperatures

$g$  Acceleration of gravity

$GTE$  Global temperature error

$HRR$  Heat release rate

$\Delta H_c$  Heat of combustion

$\Delta h_{f,\alpha}$  Heat of formation of specie

$h_m$  Mass transfer coefficient

$h_v$  Heat of vaporization of the fuel

$l$  Pool lip height

$L$  Length scale

$L_f$  50% intermittency flame height

$L_v$  Heat of vaporization of the fuel

$\dot{m}''$  Mass burning rate

$\dot{m}'''_\alpha$  Rate of formation of specie

$\bar{u}_j$  Filtered velocity

$R$  Gas constant

$S_E$  Rate of increase of energy due to the sources within the control volume

$S_{M_x}$  Field forces increment to the x-direction momentum

$p$  Pressure

$\bar{p}$  Pressão filtrada

$\bar{p}_m$  Pressure above the pool surface

$\dot{Q}$  Total heat release rate

$\dot{Q}^*$  Froude Number

$\dot{q}'''$  Heat release rate per unit volume

$Q''_F$  Heat flux supplied by the flame to the pool

$Q''_L$  Pool heat losses

$\bar{S}_{ij}$  Filtered deformation rate tensor

**Sh** Sherwood number

**T** Temperature

$T_{\text{inf}}$  Ambient temperature

$T_b$  Boiling temperature of the fuel

$T_{exp,i}$  Experimental measurement of temperature at point i

$T_g$  Temperature above the pool surface

$T_s$  Surface temperature

$T_{sim,i}$  Simulated of temperature at point i

$\Delta T_0$  Temperature rise

$\mathbf{u}$  Tridimensional velocity vector

$u_0$  Plume velocity

$u_{ijk}^n$  X-direction velocity component at cell ijk in time step n

$v_{ijk}^n$  Y-direction velocity component at cell ijk in time step n

$w_{ijk}^n$  Z-direction velocity component at cell ijk in time step n

$W_F$  Molecular weight of the fuel gas

$X_{F,g}$  Volume fraction of fuel vapor in the grid cell adjacent to the pool surface

$X_{F,l}$  Volume fraction of the fuel vapor above the surface

### **Greek letters**

$\mu$  Molecular viscosity

$\mu_{SGS}$  Subgrid-scale eddy viscosity

$\rho$  Density

$\rho_{ijk}^n$  Density at cell ijk in time step n

$\rho_{inf}$  Ambient density

$\tau_{ii}$  Normal stress in face i

$\tau_{ij}$  Shear stress in the face i and in direction j

$\hat{\tau}_{ij}$  Subgrid-scale strain tensor

# Contents

<b>1</b>	<b>Introduction</b>	<b>20</b>
1.1	Objective . . . . .	22
1.1.1	Specific objectives . . . . .	22
<b>2</b>	<b>Literature review</b>	<b>24</b>
2.1	Pool Fires . . . . .	25
2.1.1	Fire size and burning rates . . . . .	27
2.1.2	Flame height . . . . .	30
2.1.3	Fire Plume . . . . .	32
2.1.4	Structure of diffusion flames . . . . .	33
2.1.5	FDS modelling of pool fires . . . . .	35
2.2	Computational Fluid Dynamics . . . . .	38
2.2.1	Finite Differences Method . . . . .	40
2.2.2	Governing Equations . . . . .	40
2.2.3	Turbulence . . . . .	44
2.2.4	FDS modelling . . . . .	49
<b>3</b>	<b>Materials and Methods</b>	<b>53</b>
3.1	Experimental Work . . . . .	53
3.1.1	Experimental setup . . . . .	53
3.1.2	Pan burner . . . . .	56
3.1.3	Weight measurements (evaporation rate) . . . . .	56
3.1.4	Temperature measurements . . . . .	56
3.1.5	Data acquisition system . . . . .	58
3.1.6	Flame height measurements . . . . .	58

3.2	Simulations . . . . .	59
3.2.1	Computational setup . . . . .	59
3.2.2	Computational Methods . . . . .	60
3.2.3	Boundary Conditions . . . . .	60
3.2.4	Burning rates . . . . .	62
3.2.5	Fuel descriptions . . . . .	62
3.2.6	Mesh . . . . .	64
3.2.7	Temperature Measurement . . . . .	64
3.2.8	Flame Heights . . . . .	64
3.2.9	Mesh sensitivity analysis . . . . .	65
<b>4</b>	<b>Results and Discussion</b>	<b>66</b>
4.1	Experimental work . . . . .	66
4.1.1	Evaporation results . . . . .	66
4.1.2	Mass Loss Rate per Unit Area . . . . .	70
4.1.3	Flame height results . . . . .	72
4.1.4	Temperature results . . . . .	75
4.2	Simulation results . . . . .	89
4.2.1	Prescribed MLRPUA results . . . . .	89
4.2.2	Influence of CO and soot modelling . . . . .	101
4.2.3	Influence of the turbulence sub-grid model . . . . .	103
4.2.4	Analysis of the Liquid Pyrolysis Model . . . . .	105
<b>5</b>	<b>Conclusions</b>	<b>110</b>
<b>A</b>	<b>Average temperature curves</b>	<b>118</b>

# Chapter 1

## Introduction

Industrial fires tend to be localized, nonetheless they are very intense emitters of heat, smoke and combustion products. This is particularly true if the fuel is a petroleum-based substance, with high energy density and potential for soot formation (Baum & McGrattan, 1999).

Handling flammable and combustible liquids involves noteworthy risk. Risk which is not only present in the industrial processes where these products are used, but also in their storage. Chang e Lin(2006) have presented a revision of 242 accidents in storage tanks that have occurred in industrial facilities between 1960 and 2003. The results show that 74% of the accidents occurred in petroleum refineries and oil terminals or storage areas. Besides that, 85% of the accidents have involved fire and/or explosion.

Flammable and combustible liquids are frequently stored in drums and IBC containers (Intermediate Bulk Container). These recipients are stored in warehouses in piles in configurations that maximize the area usage (Figure 1.1). Under such conditions, a fire initiated in a recipient can propagate to others around it leading to a domino effect that can causes damage to the installation and to the workers' lives. Therefore, among the risks associated to the storage of flammable and combustible liquids, fire is the most worrisome of them.

Reliable prediction and description of a fire scenario has a major importance in safety engineering and risk analysis. The knowledge of the temperature field around a



Figure 1.1: Chemicals warehouse with drums and IBCs.

pool fire has great value on the study of the safety conditions of a facility. It affects the design of the fire-fighting system, the distances between tanks of flammable liquids and escape routes. A number of experimental techniques have been applied in the study of the fire phenomenon. However, full scale experiments for most of the relevant scenarios involve high costs and are often impracticable or even impossible to replicate.

Fire systems have been traditionally simulated by means of zone models (Quintiere, 1984). These models divide the study domain in different zones, each of them described by a set of parameters and semi-analytic approaches. Zone models are characterised by low costs and easy applicability, however, their range of application is limited to relatively simple fire scenarios that can be described in terms of a set of idealised components (Hurley et al., 2015). With the increase of processing power of modern computers, CFD (Computational Fluid Dynamics) models became more accessible and they have emerged as a promising simulation tool to be used in a broad range of engineering fields, including fire modelling (Novozhilov, 2001).

Sufficient validation of fire models is necessary to ensure that the user has enough information on the adequacy of the model, the appropriateness of its use and the confidence level of its predictions (Hurley et al., 2015). CFD models are typically validated by comparing its results to experimental measurements. This process is performed by the selection of appropriate experiments and then by the quantification of the accuracy of the model prediction (Hurley et al., 2015).

Among the available CFD software for fire simulation, Fire Dynamics Simulator (FDS), developed by the National Institute of Standards and Technology (NIST), has been receiving great attention in the fire community and it has been applied in a broad range of applications. FDS is an open source CFD code that uses a large-eddy simulation (LES) approach to solve the Navier-Stokes equations adapted for low-Mach number flows (McGrattan et al., 2015a).

Even though FDS has not been firstly designed to simulate pool fires, review of the literature on the validation of FDS suggests that the software is an emerging tool to predict the fire behaviour of such scenarios. There is a variety of studies where FDS, in its default form or in modified forms, have been compared to pool fires experiments (Xin et al., 2005; Kang & Wen, 2004; Ma & Quintiere, 2003; Wen et al., 2007; Hostikka et al., 2003; Wahlqvist & van Hees, 2016; McGrattan et al., 2015a). However, most of the work for validation of the FDS temperature field address room ceiling, room corners and pool centreline temperatures. In the present work, FDS is tested to predict the temperature profile in 49 positions around a pool fire for three fuels largely used in industry and with different burning behaviour: hexane, hydrous ethanol and type C gasoline.

## 1.1 Objective

The main objective of this work is to clarify how adequately FDS model correlates with the experimental flame heights and temperature fields of a small pool fires in controlled experiment.

### 1.1.1 Specific objectives

- Analyze the qualitative and quantitative agreement between experimental and simulated temperatures and flame heights.
- Compare the main turbulence models available on FDS.
- Analyze the effect of CO and Soot yield in the simulated temperature field.

- Compare the simulation results with the two burning modes available in FDS: the burning rates prescribed by the user and calculated by the software.

The work is organized as follows: chapters 2 and 3 addresses the bibliography review on the pool fire concepts and the computational fluid dynamics (CFD), respectively. Chapters 4 and 5 describes the methodology and results for the experimental work and the simulations. Finally, chapter 6 draw the conclusions.

## Chapter 2

### Literature review

Fire can be defined as the rapid oxidation of a combustible material liberating heat, light and reaction products. When appropriately controlled, fire supplies excellent benefits such as energy and heat to satisfy our industrial and domestic necessities. However, uncontrolled, it can cause immeasurable material damage and human suffering (Drysdale, 2011).

The understanding of fire is not a simple matter. There is no doubt it is one of the most complex phenomena considered in combustion science. It encompasses nearly all effects encountered in subsonic chemical reactive flows: fluid dynamics, combustion, kinetics, radiation and, frequently, multiphase flows, forming an extremely complex physical and chemical phenomenon (Novozhilov, 2001).

Fire is a gaseous state phenomenon; hence, the burning of a combustible liquid or solid must involve its conversion to the gaseous form. For liquids, this process is generally the simple evaporation of the fuel, but for solids, it must involve the chemical decomposition or pyrolysis to generate molecules with sufficiently low molecular weights that can volatilize and enter the flame (Drysdale, 2011).

The gaseous fuel must combine with oxygen from the air to form a flammable mixture that, ignited, creates the flame. In most fires, the mixture of fuel vapor and oxygen is obtained mainly by diffusion and has a much larger time scale than the combustion reaction itself. Therefore, the diffusion of species is the phenomenon that controls the

flame behavior (Hurley et al., 2015).

## 2.1 Pool Fires

Among numerous possible fire scenarios, pool fires are characterized by the establishment of a diffusive flame over a horizontal combustible surface within defined limits. In a pool fire, the flame is controlled by buoyancy and is sustained by the gasification of the liquid fuel that occurs through heat transfer to the surface (Joulain, 1998). Industrial accidents resulting from fuel spills and tank explosions are examples of systems that commonly burn as pool fires (Xin et al., 2005).

Figure 2.1 shows a schematic drawing of a pool fire and indicates the major physical phenomena that take place in this sort of fires.

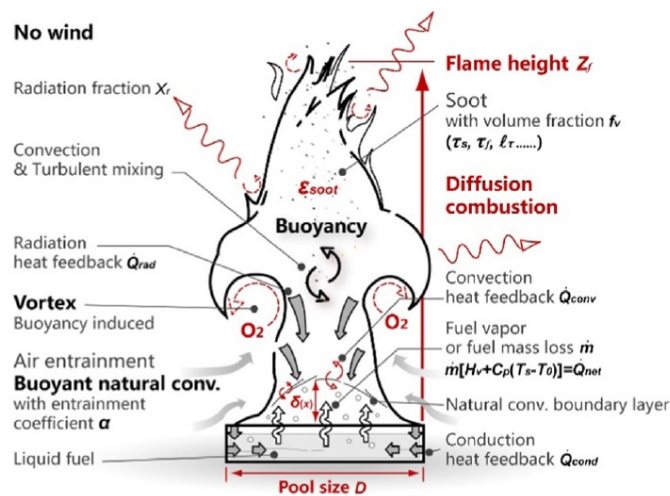


Figure 2.1: Physical Phenomena in pool fires (Hu, 2017).

Pool fires typically burn as non-pre-mixed flames, also called diffusion flames. The fuel and the oxygen are initially separated and burn as they mix. In this sort of fires, a shortage of oxidizer often takes place, which restrains the completion of the reaction, and the flame tends to burn slower and to produce more soot than premixed flames. In such fires, the soot produced becomes incandescent from the heat of the flame, which gives the flame a perceptible orange-yellow color. Diffusion flames have characteristically

less-defined flame shape than pre-mixed flames.

In liquid pool fires, the rate of supply of volatiles from the fuel surface is directly linked to the rate of heat transfer from the flame to the fuel. The mass burning rate of fuel<sup>1</sup> ( $\dot{m}'''$ ) can be expressed as:

$$\dot{m}'' = \frac{Q'_F - Q'_L}{L_v} \quad (2.1.1)$$

Where  $Q'_F$  is the heat flux supplied by the flame,  $Q'_L$  accounts for the heat losses and  $L_v$  is the heat required to produce the volatiles, which, for a liquid, is simply the latent heat of evaporation.

Pool fires are frequently divided in three-zone structures as proposed by McCaffrey (1983) and Cox & Chitty (1980): a continuous flame zone at the base of the flame, which is followed by an intermittent flame zone where active turbulent mixing takes place, and above it a plume zone where the centerline temperature begins to decrease.

Small pool fires have particular characteristics, which were studied by Venkatesh et al. (1996). Those authors divided the continuous flame zone of such fires into three subzones: the quenching zone, the primary anchoring zone (PAZ), and the post-PAZ, as illustrated in Figure 2.2. The quenching zone is just above the pool rim and has a sub-millimeter size. In this area, fuel and air premix by molecular diffusion. Above that, PAZ is believed to be a diffusion-controlled zone where air entrainment likely occurs to satisfy mass conservation because of the rapid acceleration of the buoyant gases in the flame interior. Due to the premixing in the quenching zone, the visible flame is not attached directly to the burner rim, but anchored at PAZ, which, according to Kang & Wen (2004), is the unique characteristic that distinguishes small pool fires from medium/large-scale fires. In post-PAZ region, the flame is a pseudo-laminar continuous flame, where air stream-

---

<sup>1</sup>The mass burning rate in a pool fire measures the rate at which the fuel vaporizes and leave the liquid pool.

lines are parallel to the visible flame surface, and air transport to the flame is by diffusion.

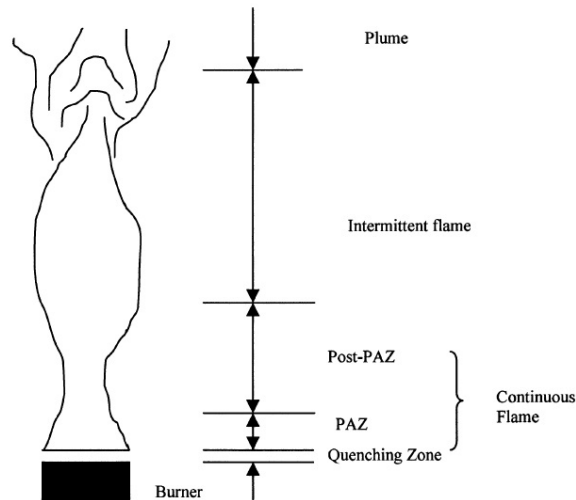


Figure 2.2: Five-zone flame structure (Venkatesh et al., 1996).

### 2.1.1 Fire size and burning rates

The fire size is a fundamental information to quantify the hazard associated with fire. It is mainly characterized by the heat release rate, HRR, and the flame height. HRR can be calculated with equation 2.2.1, where  $\dot{m}''$  is the mass burning rate (or mass loss rate) per unit area of the fuel,  $A$  is the pool area and  $\Delta H_c$  is the fuel heat of combustion.

$$HRR = \dot{m}'' \times A \times \Delta H_c \quad (2.1.2)$$

In the case of a pool fire, the size of the pool fire is directly related to the diameter of the pool. Babrauskas (1983) have distinguished four burning modes that can be observed for pool fires, accordingly to their sizes. Table 2.1 shows the burning modes as a function of the pool diameter.

In the burning process of a liquid pool fire, the fuel must first vaporize, and then diffuse toward the oxygen from the environment. Therefore, the fuel-burning rate

Table 2.1: Pool fire burning modes

Pool fire diameter (m)	Burning mode
<0.05 (2 in)	Convective, laminar
<0.2 (8 in)	Convective, turbulent
0.2 to 1.0 (8in to 3.3 ft)	Radiative, optically thin
> 1.0 (3.3 ft)	Radiative, optically thick

can be modelled through the evaporation rate of the fuel.

As reported in previous studies (Babrauskas, 1983; Jiang et al., 2016), the burning rate is a function of the pool size and increases with the increasing of the pool diameter. Hamins et al. (1999) have studied the burning rate of different fuels and proposed a model to predict the mass burning flux consuming liquid fuels in a quiescent environment. Figure 2.3, obtained from Hamins et al. (1999), shows the mass flux relation with diameter for hexane burning.

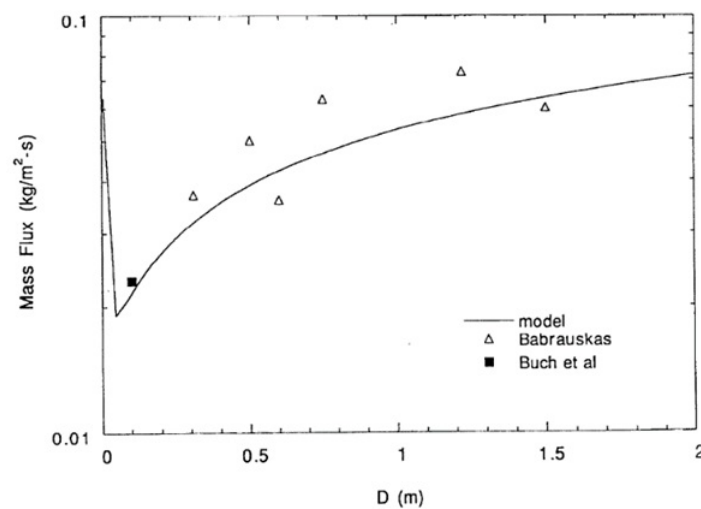


Figure 2.3: Comparison of experimentally measured mass fluxes and Hamins' model (Hamins et al., 1999).

Babrauskas (1983) has reported mass burning rates for large pool fires. Table 2.2 shows the burning rates obtained by Babrauskas for fuels similar to those studied in the present work.

Table 2.2: Mass loss rate per unit area for a large pool fire

	Hexane	Ethanol	Gasoline
MLRPUA (Kg/m <sup>2</sup> s) (Babrauskas, 1983)	0.074 ± 0.005	0.015 ± 0.001	0.055 ± 0.002

According to Z. Chen, Wu, et al. (2014), a pool fire development process can be divided into three stages. The first stage is characterized by accelerated burning rate and temperature rising. As the heat obtained by the fuel from the flame approaches the heat transmitted from the fuel to the ambient medium, the fire reaches a steady-state combustion where the burning rate is stable. The third state is reached as the fuel supply becomes inadequate and the burning rate falls continuously.

Hayasaka (1997) has performed experiments with thin pool fires and observed that the burning rate presents two steady state values. The first steady burning rate is reached rapidly after the fuel is ignited whereas the second is observed when bulk ebullition takes place in the liquid fuel; which leads to a higher burning rate stage. Wang et al. (2015) and B. Chen et al. (2012) also have found five stages for the burning rate, including initial growth (I), quasi-steady burning with surface boiling (II), transition to bulk boiling (III), bulk boiling burning (IV), and decay to extinction (V), as in Figure 2.4. However when the fuel thickness is decreased, the fuel is consumed completely before the bulk-boiling occurs, which leads to the disappearance of two stages of transition and only three stages are left: initial growth (I), quasi-steady burning with surface boiling (II) and decay to extinction (V).

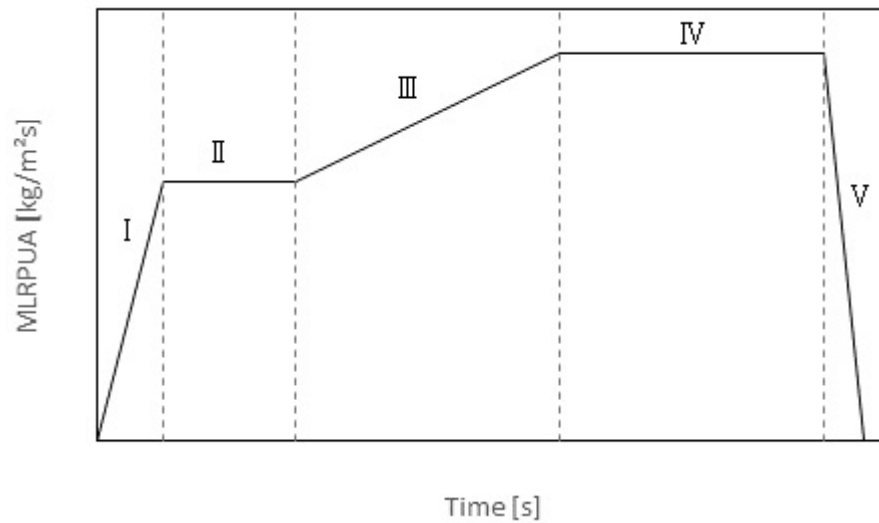


Figure 2.4: Burning rate stages for thin layer pool fires.

As a consequence of the dynamic behaviour of the burning rates, the temperatures, velocities and other flow properties around a pool fire also evolves with time. As an example, standardized time-temperature curves, such as ISO 834; the hydrocarbon curve (HC) or the RWS curve, are widely used to evaluate the heat exposure to a tunnel construction (Li & Ingason, 2018).

### 2.1.2 Flame height

Flame height is usually defined as the vertical dimension from the burning material surface to the tip of the luminous flame. Figure 2.5 shows a sketch of the flame height definition, where  $H_{fl}$  stands for flame height,  $D$  is the pool diameter,  $d$  is the pool depth and  $l$  is the lip height.

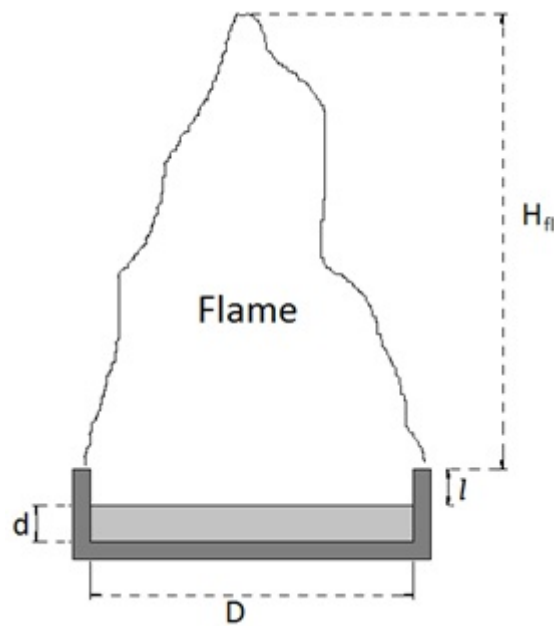


Figure 2.5: Illustration of the flame height definition.

As shown in Figure 2.2, flames are typically divided in a continuous flame region and an intermittent flame region. Flame fluctuations that occurs in the intermittent region are caused by the instability induced by buoyancy. Barr (1953) described this process as a progressive necking formation which eventually causes the separation of the flame in two pieces. The upper flame bubble burns itself out, whereas the lower part of the flame remains anchored and continues to grow in length.

Since there are considerable fluctuations of the flame at the intermittent region, an average flame height was defined by Zukoski et al. (1985). The concept of flame appearance probability or intermittency ( $I$ ), is introduced and is defined as the fraction of time over which at least part of the flame lies above a horizontal plane at elevation  $H$  above the pool. Average flame height ( $H_{fl}$ ) is usually defined as the height that yields intermittency of 50%.

The flame height of a pool fire can be estimated based on a number of experimental correlations such as those proposed by Zukoski et al. (1985) and Heskestad (1983). The correlation proposed by Heskestad (1983) has been shown to be quite robust and provides satisfactory predictions for different fuels over a wide range of pool fire sizes:

$$L_f = 3.7\dot{Q}^{*2/5} - 1.02D \quad (2.1.3)$$

where  $L_f$  is the 50% intermittence flame height (m),  $D$  is the diameter of the pool (m) and  $\dot{Q}^*$  is the Froude number, defined by Eq. 2.1.4:

$$\dot{Q}^* = \frac{\dot{Q}}{\rho_\infty c_p T_\infty \sqrt{gD} D^2} \quad (2.1.4)$$

where  $\dot{Q}$  is the total heat release rate,  $\rho_\infty$  and  $T_\infty$  are ambient density and temperatures,  $c_p$  is the specific heat of air at constant pressure and  $g$  is the acceleration of gravity.

### 2.1.3 Fire Plume

The buoyant gas stream of a fire is always turbulent, except when the source is very small and smoldering (Heskestad, 1984). The fire plume can be defined as the buoyant flow formed by the combustion gases movement, which may include portions of the flame itself.

Figure 2.6 shows a schematic representation of a fire plume originating at a flaming source. A diffusion flame is formed by the mixture of air with volatile molecules driven off from the combustible source by the heat feedback from the fire. The dashed boundary confines the entire buoyant flow of combustion products and entrained air. Inside this region, the flow profile can be described in terms of time-averaged temperature rise above the ambient temperature, the concentration of a gas, such as  $CO_2$ , generated by the fire, or the axial velocity in the fire plume (Heskestad, 1984).

The temperature rise,  $\Delta T_0$ , and velocity,  $u_0$ , profiles on the centerline of the fire are shown in the right side of Figure 2.6. These are qualitative representations of those quantities based on experimental observations (Xin et al., 2008; Z. Chen, Wen, et al., 2014a).

In this example, the lower portion of the flame is characterized by high temperatures, which are nearly constant. Temperatures decay in the upper portion of the flame, where the intermittent flame occurs and combustion is depleted and air entrained from the surrounding cools the flow. The velocities at the centerline have their maximum slightly below the mean flame height,  $L$ , and always decay with height (Heskestad, 1984).

The total heat release rate of a fire source is transmitted by convection and radiation. In liquid pool fires and other horizontal-surface fires, convection rarely accounts for less than 60-70% of the total heat release rate (Z. Chen, Wen, et al., 2014b). The convective flux is carried away by the plume above the flames while the radiative flux is transferred in all directions.

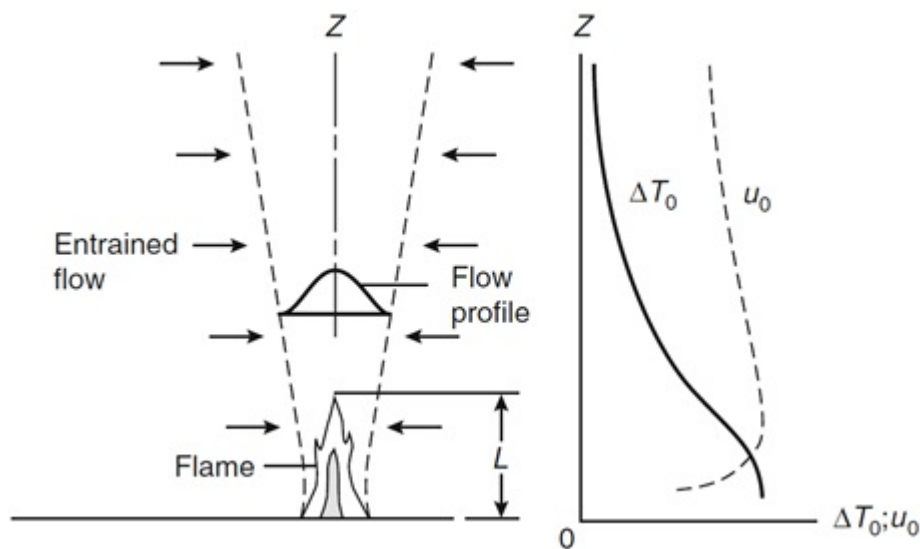


Figure 2.6: Features of a turbulent fire plume, including axial variations on the centerline (Heskestad, 1984).

#### 2.1.4 Structure of diffusion flames

Figure 2.7 illustrates the structure of a diffusion flame, which is formed in the intersection of a fuel-rich zone and an oxidizer-rich zone. In the flame (or reaction zone), as the fuel and the oxidizer are consumed by the reaction, their concentrations almost disappear although some leakage still occurs in both sides. This is also the region where temperature reaches its maximum value, as a consequence of the heat released by the

flame.

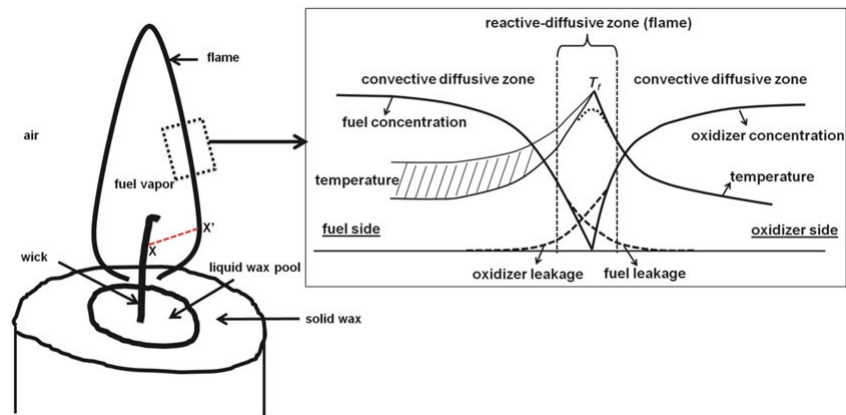


Figure 2.7: Structure of a diffusion flame in a candle fire (Gottuk & Lattimer, 2016).

Hydrocarbon fires are often associated with yellow flames. This is specially true in the case of sooty fuels, which can be explained by Figure 2.8. The reaction zone normally produce blue emissions which are due to the excited CH radicals. The radiation of  $\text{CO}_2$  and water are responsible for the reddish glow commonly observed in such fires. The yellow radiation are associated with the presence of carbon particles or soot.

Figure 2.8 shows a cracking zone in the fuel side which is responsible for the cracking and polymerizing reactions where lighter fuel molecules are formed. This molecules chemically react with the oxygen in the reaction zone and produce carbonaceous in the soot formation zone, which is between the reaction zone and the cracking zone. Soot is then formed by a nucleation and surface growth mechanism (Gottuk & Lattimer, 2016). Soot formation is specially important in the energy balance of fires, in fact, in many cases of real fires, soot is the dominant source and sink of thermal radiation. A sooty fire typically radiates approximately one-third of the total combustion energy (McGrattan et al., 2015b).

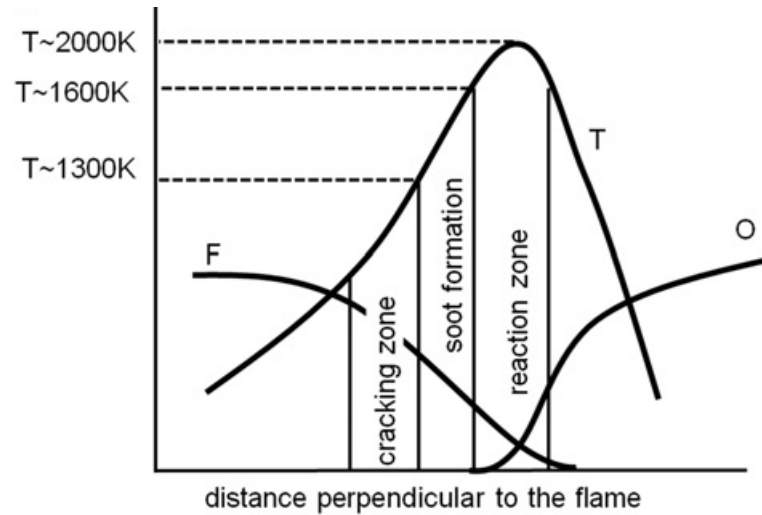


Figure 2.8: Zones of a diffusion flame (Gottuk & Lattimer, 2016).

In a pool fire, CO and soot yields are affected by the oxygen availability, compartment geometry, ventilation, flow characteristics, thermal environment, chemistry, and mode of burning. Among these fire conditions, the mode of burning and ventilation are specially important in the product formation (Gottuk & Lattimer, 2016).

### 2.1.5 FDS modelling of pool fires

First fire models developed were zone models, which are still broadly used because of the low computational demand. These models divide the study domain in different zones, each of them described by a set of parameters and semi-analytic laws. The parameters describe averaged physical quantities, such as temperature and concentrations, of each zone (Novozhilov, 2001).

With the increase of processing power of modern computers, CFD models became more accessible and they have been used in a broad range of engineering fields, including fire modeling. This approach is based on the conservation laws for physical quantities such as mass, momentum, energy and species concentration. These equations are resolved for points in space and time and generate a distribution of the quantities of interest. As a result, CFD yields a whole history of the fire evolution including local characteristics in any point in time and space. This sort of modeling is only possible by numeric methods and the associated computational cost is considerably higher than that for zone models (Novozhilov, 2001).

Along with rapid improvements in computer technology in recent years, CFD models have already been implemented in computer simulation software, such as the NIST's FDS, ANSYS FLUENT or FIREFOAM developed between CFD Direct and FM-Global. These CFD models have been successful in describing several scenarios for practical applications.

The Fire Dynamics Simulator (FDS) is an open source CFD code used worldwide in fire engineering applications and research that was first released to the public in February 2000. As described in the FDS Validation Guide, the software release was the result of two decades of NIST studies on CFD codes for different applications and for research.

FDS package consists of three parts: pre-processing, processing and post-processing. In the first, a text file is written in a text editor where fire case is described (input values, boundaries, mesh grid, etc). The processing part is the calculation itself, performed by the software. The post-processing is undertaken by Smokeview, software where animations and images of output values can be visualized and analyzed.

The main purpose of FDS is to study smoke spreading, smoke venting and the activation of detector in natural building fires. Since its release, the software has been tested and validated for numerous scenarios. The validation work in literature involves several approaches such as: comparisons with full-scale tests conducted especially for the chosen evaluation, comparisons with previously published full-scale test data, comparisons with standard tests, comparisons with documented fire experience and comparison with engineering correlations.

Review of the literature on experimental studies and numerical investigations based on FDS suggest that the software is a promising tool to predicting the fire behavior of pool fires. Hostikka et al. (2003) tested the numerical modelling used by FDS radiation solver for low-sooting pool fires (methane, natural gas and methanol). The authors conclude that the model can qualitatively predict the pool size dependence of the burning

rate, but the predicted radiative fluxes were higher than measured values, especially at small heat release rates, due to an over-prediction of the gas temperature.

Ma & Quintiere (2003) have compared FDS (version 2.0) to benchmark correlations and found that the flame height prediction fit well with flame height correlations. Temperature and mixture fraction are also compared and found to be close to the empirical estimations at flame tips. Kang & Wen (2004) have applied a previous version of FDS to predict the behavior of a small-scale pool fire experimentally tested by Weckman & Strong (1996) where temperature and velocities were measured in PAZ region. Two modified SGS combustion models were used and compared with experimental data and both have shown good agreement with the experimental temperature and velocity fields. For the mean temperature field, the prediction with both models have shown good agreement with experimental data. However, considerable discrepancies between the models have been found in the predictions of the velocity and temperature fields. Kang's paper highlights the importance of SGS combustion modelling in capturing the fine details of small pool fires.

Xin et al. (2005) used a previous version of FDS to simulate a 7.1 cm buoyant turbulent diffusion flame using a mixture-fraction-based combustion model. The fire was produced by methane burning with a flow rate of 84.3 mg/s, which yields a Froude number, which matches that of a liquid toluene pool fire with the same size. The temperature profile was analyzed for elevations ranging from 0.07 to 1.41 diameters and 15 radius distances (0 to 4 cm). The mean flame surface positions are displaced toward the flame axis at lower elevations.

Discrepancies are observed and reach up to 500 K in the temperature estimates for lower elevations. Discrepancies were smaller at the farthest downstream locations (errors below 250 K). Besides that, it is concluded that FDS can qualitatively capture the instantaneous fire structures and quantitatively reproduces the averaged scalars and velocities.

Wen et al. (2007) have applied FDS to simulate a medium-scale methanol pool

fire and compare two combustion models with the experimental data obtained by Weckman & Strong (1996) for a 30.5 cm pool. Temperatures were measured in four elevations (6 to 30 cm) and seven radius distances (0 to 0.16 m). The results have shown that FDS can deliver accurate predictions for most important parameters of pool fires such as mean temperatures and axial velocity distributions as well as air entrainment ratios.

Recent work where FDS was used to simulate fire scenarios include Yuan and Smith's paper (2015) where the authors simulate the water spray suppression of conveyor belt fires in a large-scale tunnel and investigate the effects of sprinkler configuration on the suppression of the fire. Brzezinska & Markowski (2017) have performed full scale tests of LPG release from a car installation and compared experimental results with FDS simulations of gas emission and dispersion. Loy et al. (2018) have proposed a surrogate modelling of net radiation flux from pool fires applicable to hydrocarbon storage facilities. The authors present an effective Quantitative risk assessment (QRA) methodology which is tested in a case study of a hydrocarbon pool fire in a storage facility. However, studies such as this relies on the simulation quality, which can only be confirmed by the validation work.

Beyond the papers described above there is a variety of other studies where FDS, in its default form or in modified forms, have been compared to pool fires experiments (Skarsbø, 2011; Wahlqvist & van Hees, 2016; Sahu et al., 2016; McGrattan et al., 2015a). However, most of the work for validation of the FDS temperature field address room ceiling, room corner and pool centerline temperatures. In the present work, FDS is tested to predict the temperature profile in 49 positions around a pool fire for three fuels largely used in industry and with different burning behaviours.

## 2.2 Computational Fluid Dynamics

The prediction of flow and heat transfer processes can be obtained through two routes: experimental or theoretical calculus (Patankar, 1980). The experimental route is generally the most trustworthy course; however, experiments have high costs and

are often impracticable. Besides that, even in reduced scales, experiments costs increase proportionally to the number of measurement points and tested configurations (Versteeg & Malalasekera, 1995). The analysis of systems using mathematical models permit the reproduction of numerous scenarios and generate an amount of data that would be impractical experimentally.

Theoretical predictions are undertaken by solving a mathematical model, instead of a physical model. For flow and heat transfer processes, the most sophisticated mathematical models consist of a set of differential equations. If analytical methods were to be used to solve these equations, few phenomena of practical interest could be predicted. With the development of numerical methods and the availability of high processing power of computers in modern society, there is an expectation that mathematical models could be solved for nearly any practical problem (Patankar, 1980).

Versteeg & Malalasekera (1995) define Computational Fluid Dynamics (CFD) as the analysis of systems involving flow, heat transfer and associated phenomena, such as chemical reactions, by means of computational simulations.

The methodology used by CFD consists of transforming the differential equations that describe the flow into algebraic equations, which are then solved numerically in a field of discretized points in time and space. By discretizing the study field, CFD transforms the problem of solving the differential equations into a problem of finding the values of physical quantities (temperature, velocities, etc) in a finite number of points.

These quantities are obtained by the resolution of a system of algebraic equations which, being derived from the differential equations that describe the system, expresses the same information as those equations. As the number of mesh points increases, the solution of the discretized equations becomes closer to the exact solution of the corresponding differential equation (Patankar, 1980).

There is a number of techniques to obtain the numerical discretization. Finite differences, finite elements and finite volumes are the most commonly used ones. Accord-

ing to Fortuna (2000), regardless of the technique, all the solutions of CFD simulations have three types of errors:

- Inherent to the discretization process
- Rounding caused by the computer calculation
- Numerical approximation of auxiliary conditions.

### 2.2.1 Finite Differences Method

Finite differences method employs the expansion of the Taylor series to transform the derivative of the equation into algebraic analogues. As an example, the discretization of mass conservation equation can be written as:

$$\rho_{ijk}^{n+1} = \rho_{ijk}^n - \delta t \left( \frac{\rho_{i+1/2jk}^n u_{ijk}^n - \rho_{i-1/2jk}^n u_{i-1jk}^n}{\delta x} + \frac{\rho_{ij+1/2k}^n v_{ijk}^n - \rho_{ij-1/2k}^n v_{ij-1k}^n}{\delta y} + \frac{\rho_{ijk+1/2}^n w_{ijk}^n - \rho_{ijk-1/2}^n w_{ijk-1}^n}{\delta z} \right) \quad (2.2.1)$$

At the beginning of the simulation, an initial value is imputed to each grid cell. As simulation progresses in time, these values are updated with every time step.

### 2.2.2 Governing Equations

The governing equations of fluid dynamics represent mathematical declarations of the conservation laws:

- The fluid mass is conserved
- The rate of change of momentum is equal to the sum of the forces in a fluid particle (Newton's second law)
- The rate of change of energy is equal to the sum of the rates of added heat and work done in a fluid particle (first law of thermodynamics)

These laws are expressed in the form of differential equations, each of them carrying a physical quantity as dependent variable.

### Continuity equation

The mass conservation principle states that matter cannot be created or destroyed. The principle implies that any increase in the mass inside the control volume is equal to the net mass flow into the control surface (Abbott & Basco, 1989). The continuity equation is a consequence of the principle of mass conservation and can be expressed by eq 2.2.2. The first term of the equation represents the mass accumulated within the system, whereas the second describes the net mass flux leaving the fluid element, called convective term.

$$\delta\rho/\delta t + \nabla \cdot (\rho\mathbf{u}) = 0 \quad (2.2.2)$$

### Momentum equation

The differential equation that governs the momentum conservation is derived from Newton's second law. Equation 2.2.3 represents the momentum conservation equation in the x-direction for a Newtonian fluid:

$$\frac{\delta}{\delta t}(\rho u) + \nabla \cdot (\rho u\mathbf{u}) = -\frac{\delta p}{\delta x} + \frac{\delta\tau_{xx}}{\delta x} + \frac{\delta\tau_{yx}}{\delta y} + \frac{\delta\tau_{zx}}{\delta z} + S_{M_x} \quad (2.2.3)$$

The left side of the equation represents the rate of change of momentum in the x-direction for a fluid particle. The right side of the equation represents the resulting force in the x-direction in a fluid element due to the friction forces summed by the increase of momentum in the x-direction due to the field forces, such as gravity, (Versteeg & Malalasekera, 1995).

Equations such as equation 2.2.3 can be written for the momentum conservation in the y and z-directions.

### Energy equations

Derived from the first law of thermodynamics, the energy equation is obtained equating the rate of change of energy in a fluid element to the sum of the rate of net work done in the fluid, the rate of heat added to the system and the rate of increase of energy due to the sources within the control volume (Versteeg & Malalasekera, 1995). Equation 2.2.4 presents the energy equation in its differential form:

$$\begin{aligned} \frac{\delta}{\delta t}(\rho E) + \nabla \cdot (\rho E \mathbf{u}) = & \left[ \frac{\delta u \tau_{xx}}{\delta x} + \frac{\delta u \tau_{yx}}{\delta y} + \frac{\delta u \tau_{zx}}{\delta z} + \frac{\delta v \tau_{xy}}{\delta x} + \frac{\delta v \tau_{yy}}{\delta y} + \frac{\delta v \tau_{zy}}{\delta z} \right. \\ & \left. + \frac{\delta w \tau_{xz}}{\delta x} + \frac{\delta w \tau_{yz}}{\delta y} + \frac{\delta w \tau_{zz}}{\delta z} \right] + \nabla \cdot (k \Delta T) + S_E \end{aligned} \quad (2.2.4)$$

### State equation

The tridimensional movement of the fluid is described by the five differential equations described above: the continuity equation, Eq. 2.2.2, the three momentum equations, Eq. 2.2.3 and its analogues in the directions y and z, and the energy equation, Eq. 2.2.4. However, it is possible to correlate some of the unknown variables using concepts of thermodynamics. The speed of the flow is generally not large enough to prevent it from adjusting thermodynamically. Therefore, the fluid can be considered in thermodynamic equilibrium for most of the systems (Versteeg & Malalasekera, 1995).

The state of a substance in thermodynamic equilibrium can be described by state equations. For a perfect gas, equations 2.2.5 and 2.2.6 are applicable:

$$p = \rho RT \quad (2.2.5)$$

$$E_i = c_v T \quad (2.2.6)$$

## Newtonian fluids

The state of tension of a fluid element can be described by a set of normal and shear stresses, as in Figure 2.10. Shear stresses are related to the rate of strain of fluid element while normal stresses are related to the rate of change of the volume (Wendt, 2008).

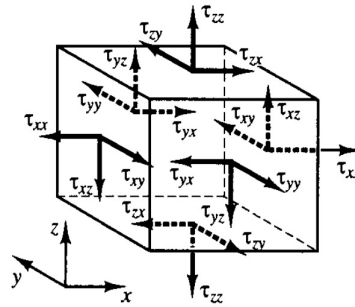


Figure 2.9: Stress components of a fluid element in the three orthogonal directions (Versteeg & Malalasekera, 1995).

Fluids are defined as Newtonian when shear stress is proportional to the fluid's rate of strain. This relation, proposed by Isaac Newton for parallel and laminar flows, was extended to three dimensional flows by George G. Stokes, originating equations 2.2.7, 2.2.8 and 2.2.9.

$$\tau_{xy} = \tau_{yx} = \mu \left( \frac{\delta u}{\delta y} + \frac{\delta v}{\delta x} \right) \quad (2.2.7)$$

$$\tau_{yz} = \tau_{zy} = \mu \left( \frac{\delta v}{\delta z} + \frac{\delta w}{\delta y} \right) \quad (2.2.8)$$

$$\tau_{zx} = \tau_{xz} = \mu \left( \frac{\delta w}{\delta x} + \frac{\delta u}{\delta z} \right) \quad (2.2.9)$$

Likewise, normal stresses can be related to the rate of strain, according to equations 2.2.10, 2.2.11 and 2.2.12, also obtained by Stokes.

$$\tau_{xx} = \mu \left( 2 \frac{\delta u}{\delta x} - \frac{2}{3} \nabla \cdot \mathbf{u} \right) - P \quad (2.2.10)$$

$$\tau_{yy} = \mu \left( 2 \frac{\delta v}{\delta y} - \frac{2}{3} \nabla \cdot \mathbf{u} \right) - P \quad (2.2.11)$$

$$\tau_{zz} = \mu \left( 2 \frac{\delta w}{\delta z} - \frac{2}{3} \nabla \cdot \mathbf{u} \right) - P \quad (2.2.12)$$

Even with the simplification of perfect gas and Newtonian fluids, governing equations of fluid dynamics have analytic solutions only for very simple cases of laminar flows. The modelling of more complex systems requires a numerical treatment of these equations. In the case of turbulent systems, turbulence must be modelled and included in the numerical model.

### 2.2.3 Turbulence

Reynolds number is a measurement of the relative importance between inertia forces, associated to convective effects, and viscous forces. As inertial forces gain importance, the flow transitions from a laminar to a turbulent regime. The flow assumes a random behavior. This unstable behavior is observed in the fluid velocity and in all other properties (Versteeg & Malalasekera, 1995).

Turbulent fluctuations have a tridimensional character and form rotational structures, named eddies, which have variable length scales. The vortices movement can approximate fluid particles that are separated by large distances. As a consequence, heat, mass and momentum are changed very effectively (Versteeg & Malalasekera, 1995). Larger eddies interact with the mean flow and extract energy from it. This energy is progressively transferred from larger eddies to the smaller ones by means of a process known as energy cascade. In the small scale, viscosity becomes more relevant and kinetic energy is dissipated and converted into intern energy of the fluid. The energy cascade of turbulent flows is illustrated in Figure 2.10

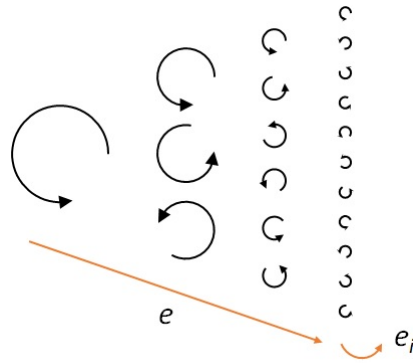


Figure 2.10: Energy cascade of turbulent flows.

Direct and complete resolution of real turbulent systems that vary with time by means of the Navier-Stokes equations requires impractical computational resources even today. This approach, called Direct Numerical Simulation (DNS) is restricted to flows with small Reynolds numbers due to the high mesh resolution required for its complete resolution. However, for the majority of practical engineering problems, it is not necessary to solve all the details of turbulent fluctuations but only account for the effect of these fluctuations in the mean flow (Versteeg & Malalasekera, 1995).

In Reynolds Averaged Navier-Stokes or RANS model, instantaneous quantities (velocity, temperature, etc) are substituted by their time-averaged values and Navier-Stokes basic equations are written as a function of these mean quantities and their fluctuations. These fluctuations are expressed mathematically in terms of Reynolds stresses. The most commonly adopted and broadly disseminated solution to solve the closure of the turbulence is based on the hypothesis of eddy viscosity and the  $k-\epsilon$  model, evolving two extra partial differential equations: for kinetic energy,  $k$ , and for energy dissipation,  $\epsilon$ .

Whereas the DNS approach is still limited to low Reynolds numbers, on the other hand, RANS model is incapable of simulating the interaction between time and length scales that exists in turbulent flows. Large Eddy Simulation, LES, is a promising alternative. In the LES model, large-scale quantities are solved directly, as in the DNS model. However, the small scales are filtered out and solved by subgrid scale (SGS) models (Kang et al., 2001). This way, LES is less computationally costly than DNS, but it is still capable of tracking the scale-dependent dynamic behavior (Wen et al., 2007).

LES avails that larger eddies are usually more energetic and effective in the transport of conservative properties than the smaller ones. Therefore, it is feasible to solve the large scales more precisely than the small scales (Novozhilov, 2001). Besides that, small eddies tend to have more universal characteristics (Cook & Riley, 1998), and it is possible to find generic models that describe their behavior or, at least, find models whose veracity is not so crucial to the whole simulation confiability (Abbott & Basco, 1989).

The approach of turbulent systems by means of spatial-averages in a fixed point in time, instead of the time-averaged as in the RANS methodology, can be interpreted as a redefinition of the concept of turbulence. By this alternative definition, turbulence comprehends all the fluctuations occurring in the small-scales other than those solved directly by a numerical model (Abbott & Basco, 1989). This is the definition of turbulence used in LES models.

### LES formalism

The filtered equation of mass conservation can be written as:

$$\frac{\delta}{\delta t}(\rho\bar{u}_i) + \frac{\delta}{\delta x_j}(\rho\bar{u}_i\bar{u}_j) = -\frac{\delta\bar{p}}{x_i} + 2\frac{\mu\bar{S}_{ij}}{x_j} + \frac{\delta\hat{\tau}_{ij}}{x_j} \quad (2.2.13)$$

where  $(S_{ij})$  is the strain rate tensor of the resolved scale, and  $(\hat{\tau}_{ij})$  is the unknown stress tensor, that represents all the effects of subgrid scale (SGS) movements in the resolved field. These tensors are defined by equations 2.2.14 and 2.2.15:

$$\bar{S}_{ij} = \frac{1}{2} \left( \frac{\delta u_j}{\delta x_i} + \frac{\delta u_i}{\delta x_j} \right) \quad (2.2.14)$$

$$\hat{\tau}_{ij} = \rho(\overline{u_i u_j} - \bar{u}_i \bar{u}_j) \quad (2.2.15)$$

## SGS modelling

In order to solve equation 2.2.15, it is necessary to model the tensor ( $\hat{\tau}_{ij}$ ). There are numerous SGS models and most of them use the supposition of eddy viscosity (Boussinesq hypothesis) to model  $\hat{\tau}_{ij}$  as:

$$\hat{\tau}_{ij} = 2\mu_t \overline{S_{ij}} + \frac{1}{3} \delta_{ij} \tau_{ll} \quad (2.2.16)$$

Hence, the problem is resumed to the modelling of eddy viscosity. Different approaches have been proposed in the literature. The most basic model was proposed by Smagorinsky (1963), which defines the eddy viscosity as a function of the characteristic length scale ( $\Delta$ ) and a constant ( $C_s$ ), which is a characteristic of the flow:

$$\mu_t = \rho(C_s \overline{\Delta})^2 S \quad (2.2.17)$$

$$S = \rho(2\overline{S_{ij}S_{ij}})^{\frac{1}{2}} \quad (2.2.18)$$

$$\Delta = (\Delta x \Delta y \Delta z)^{\frac{1}{3}} \quad (2.2.19)$$

FDS uses  $C_s=0,2$  as default for its fixed-constant model. An important limitation of the Smagorinsky model is due the fact that  $C_s$  is a characteristic of the flow. Hence, it is impossible to define a universal value for the constant for different flow fields (rotational, transitional or near-wall flows, for example). Proposed by Germano et al. (1991), the dynamic Smagorinsky model allows  $C_s$  to be computed locally based on information of the smaller resolved scales. Therefore,  $C_s$  is a function of time and space.

Deardorff Turbulence model, which is the default model used in FDS 6, solves a simple algebraic model for the subgrid kinetic energy based on the scale similarity. Viscosity is then calculated by equation 2.2.20:

$$\mu_t = \rho C_v \overline{\Delta} \sqrt{k_{sgs}} \quad (2.2.20)$$

where  $k_{sgs}$  is defined by:

$$k_{sgs} = \frac{1}{2} \left( (\bar{u} - \hat{u})^2 + (\bar{v} - \hat{v})^2 + (\bar{w} - \hat{w})^2 \right) \quad (2.2.21)$$

where  $\bar{u}$  is the mean value of  $u$  in the center of the grid cell and  $\hat{u}$  is the average value of  $u$  in the adjacent cells, defined by equation 2.2.22:

$$\bar{u}_{ijk} = \frac{u_{ijk} - u_{i-1jk}}{2} \quad (2.2.22)$$

$$\hat{u} = \frac{u_{ijk}}{2} + \frac{u_{i-1jk} + u_{i+1jk}}{4} \quad (2.2.23)$$

$\hat{v}$  and  $\hat{w}$  are defined analogously. FDS adopts a default value of  $C_v=0,1$  for the Deardorff model.

Wall flows Wall flows are notoriously challenging for large-eddy simulation (McDermott, 2009). The sophisticated method used by LES codes are resigned to model the wall shear stress rather than resolving the important length scales near the wall. This might be a challenge in cases where the walls have a relevant impact in the flow, such as tunnel fires, smoke transport in complex architectures, and wildland-urban interface (WUI) fires.

When a solid boundary is present, there is usually a substantial region where the inertial forces are dominant far from the wall and a thin layer of viscous-dominated flow. The dimensionless group  $y^+$  can be defined as:

$$y^+ = \frac{\rho u_\tau y}{\mu} \quad (2.2.24)$$

where  $u_\tau = (\tau_w/\rho)^{\frac{1}{2}}$  is the friction velocity. According to Versteeg & Malalasekera (1995), the viscous-dominated layer is in practise extremely thin ( $y^+ < 5$ ). Outside the viscous sublayer ( $30 < y^+ < 500$ ), there is a region where viscous and inertial forces are both important.

According to the work developed by McDermott (2009), FDS is second order accurate in the modelling of laminar flows when running with the DNS option, even though there is no specific treatment for the viscous layer in FDS model.

## 2.2.4 FDS modelling

FDS is a LES - Large Eddy Simulation code that solves numerically a form of the Navier-Stokes equations appropriate for low-speed thermally driven flow, with emphasis on smoke and heat transport in fires. Conservation equations of mass, energy and momentum are discretized by finite differences method on a three-dimensional, rectilinear grid and the solution is updated in time (Xin et al., 2005).

### Governing equations applied to FDS model

In FDS 6.6.0, the Navier-Stokes equations are solved using a second-order finite differences numerical scheme with a low Mach number approximation (McGrattan et al., 2015b). This approach is based on Rehm & Baum (1978) work, who observed that the spatially and temporally resolved pressure,  $p$ , can be decomposed into a "background" pressure,  $\bar{p}(z, t)$ , plus a perturbation,  $\tilde{p}(x, y, z, t)$ . For low speed applications, only the background pressure is needed to be retained in the equation of state of the ideal gas. As a consequence, the internal energy,  $e$ , and enthalpy,  $h$ , may be related in terms of the thermodynamic (background) pressure:  $h = e + \bar{p}/\rho$ . The energy conservation equation used in FDS model is then written in terms of the sensible enthalpy,  $h_s$ :

$$\frac{\delta}{\delta t}(\rho h_s) + \nabla \cdot (\rho h_s \mathbf{u}) = \frac{D\bar{p}}{Dt} + \dot{q}''' - \nabla \cdot \dot{\mathbf{q}}'' \quad (2.2.25)$$

The conductive, diffusive and radiative heat fluxes are represented in equation 2.2.25 by the term  $\dot{\mathbf{q}}''$  which is calculated by equation 2.2.26.

$$\dot{\mathbf{q}}'' = -k \nabla T - \sum_{\alpha} h_{s,\alpha} \rho D_{\alpha} \nabla Z_{\alpha} + \dot{\mathbf{q}}_{\mathbf{r}}'' \quad (2.2.26)$$

The transport equation for each of the lumped species (i.e. the continuity

equation) is given by:

$$\frac{\delta}{\delta t}(\rho Z_\alpha) + \nabla \cdot (\rho Z_\alpha \mathbf{u}) = \nabla \cdot (\rho D_\alpha \nabla Z_\alpha) + \dot{m}_\alpha''' + \dot{m}_{b,\alpha}''' \quad (2.2.27)$$

Defining the stagnation energy per unit mass,  $H \equiv |u|^2 + \tilde{p}/\rho$ , the momentum equation can be written in the form of Eq. 2.2.28 (McGrattan et al., 2015b):

$$\frac{\delta \mathbf{u}}{\delta t} - \mathbf{u} \times \boldsymbol{\omega} + \nabla H - \tilde{p} \nabla (1/\rho) = \frac{1}{\rho} [(\rho - \rho_0)\mathbf{g} + \mathbf{f}_b + \nabla \cdot \boldsymbol{\tau}] \quad (2.2.28)$$

## Combustion

The application of LES to combustion problems is a challenging task. Reactions typically take place within diffusion zones that are too much thinner than practical computational mesh; therefore, it is required to model the entire reaction, a considerably difficult task.

Combustion, as well as radiation, is introduced into the governing equations of FDS via a source term in the energy transport equation. FDS's default combustion model is based on the mixing-limited, infinitely fast reaction of lumped species. Lumped species are defined as quantities that represent a mixture of species and they are used in FDS to simplify the traceability of the system components.

For the default infinitely-fast reaction, reactant species in a given grid cell are converted to products at a rate determined by a characteristic mixing time,  $\tau_{min}$ . The grid cell is modelled as a batch reactor and the amount of the fuel that will react in a time step depends only on the stoichiometry (i.e. fuel will be unburned if there is insufficient oxygen) and the mixing time.

The heat release rate per unit volume is defined by the sum of the species rate of formation multiplied by their heats of formation, Eq. 2.2.29.

$$\dot{q}''' = \sum_\alpha \dot{m}_\alpha''' \Delta h_{f,\alpha} \quad (2.2.29)$$

The rate gaseous fuel enter the system is specified by the user by mean of the Mass Loss Rate per Unit Area (MLRPUA). The software uses this information to calculate the mixing and the rate of transformation of reactants into products. FDS has an alternative liquid pyrolysis model (LPM) that computes the evaporation rate of a liquid pool fire. To do so, the volume fraction of the fuel vapor above the pool surface is estimated by Clausius-Clapeyron relation, Eq. 2.2.30.

$$X_{F,l} = \exp\left[-\frac{h_v W_F}{R}\left(\frac{1}{T_s} - \frac{1}{T_b}\right)\right] \quad (2.2.30)$$

The rate of evaporation of the fuel is then calculated by the Stefan diffusion equation, Eq. 2.2.31:

$$\dot{m}'' = h_m \frac{\bar{p}_m W_F}{RT_g} \ln\left(\frac{X_{F,g} - 1}{X_{F,l} - 1}\right) \quad (2.2.31)$$

where:

$$h_m = \frac{Sh D_{l,g}}{L} \quad (2.2.32)$$

The liquid is modeled as a thermally-thick solid for the purpose of heat conduction and the convection within the pool is not considered. According to Hietaniemi et al. (2004) FDS has shown good agreement in the prediction of the burning rate of heptane pool fires. The authors point out, though, that reliable predictions of liquid fuels burning rates require roughly twice as fine a grid spanning the burner than it would be necessary to predict plume velocities and temperatures.

## Radiation

The thermal radiation contribution is introduced into FDS governing equations via a source term ( $\dot{q}_r'''$ ), defined by:

$$\dot{q}_r''' = -\nabla \cdot \dot{\mathbf{q}}_r''(\mathbf{x}) = \kappa(\mathbf{x})[U(\mathbf{x}) - 4\pi I_b(\mathbf{x})] : U(\mathbf{x}) = \int_{4\pi} I(\mathbf{x}, \mathbf{s}') d\mathbf{s}' \quad (2.2.33)$$

where  $\kappa(\mathbf{x})$  is the absorption coefficient,  $I_b(\mathbf{x})$  is the source term,  $I(\mathbf{x}, \mathbf{s}')$  is the solution of the radiation transport equation (RTE) for non-scattering gray gas:

$$\mathbf{s} \cdot \nabla I(\mathbf{x}, \mathbf{s}) = \kappa(\mathbf{x})[I_b(\mathbf{x}) - I(\mathbf{x}, \mathbf{s})] \quad (2.2.34)$$

# Chapter 3

## Materials and Methods

### 3.1 Experimental Work

The small-scale liquid pool fire tests were performed at Laboratório de Desenvolvimento de Processos Catalíticos (LDPC) – UNICAMP. The experimental apparatus consisted of a pan burner of 6.0 cm diameter (D) where 6.0 g of the fuel was completely burned. Three fuels were used: commercial hexane (Petrobras), hydrous ethanol (provided by a local petrol station) and type C gasoline (provided by a local petrol station). Table 3.1 shows the main characteristics of the tested fuels. The distillation ranges and vapor pressures were provided by the supplier. The distillation range for type C gasoline, however, was obtained experimentally by ASTM D86 methodology.

#### 3.1.1 Experimental setup

The burner made of stainless steel was placed inside of a fume hood of dimensions 160 cm x 80 cm x 110 cm. The side walls of the hood were at least 7.5 pool diameters from the pool centerline which was far enough to allow the flame to develop freely. The setup is represented in figures 3.1 and 3.2.

Table 3.1: Fuel properties

Property	Fuel		
	Commercial Hexane	Hydrous Ethanol	Type C Gasoline
Description	Mixture of hydrocarbon molecules	Mixture of ethyl alcohol (93.8% p/p) and water (6.2% p/p)	Mixture of anhydrous ethanol (25%) and Gasoline A <sup>a</sup> (75%)
Distillation range (°C)	66.5 to 71.9	78.2	38.5 to 191.3
Vapor pressure at 37.8 °C (kgf/cm <sup>2</sup> )	40	13	55

<sup>a</sup>Gasoline A is the gasoline obtained directly from oil refining. It is an extremely volatile and complex mixture of more than four hundred volatile, flammable, liquid petroleum-derived compounds with chain lengths ranging from C4 to C12



Figure 3.1: Experimental apparatus composed of a scale and a burner inside of a standard fume hood.

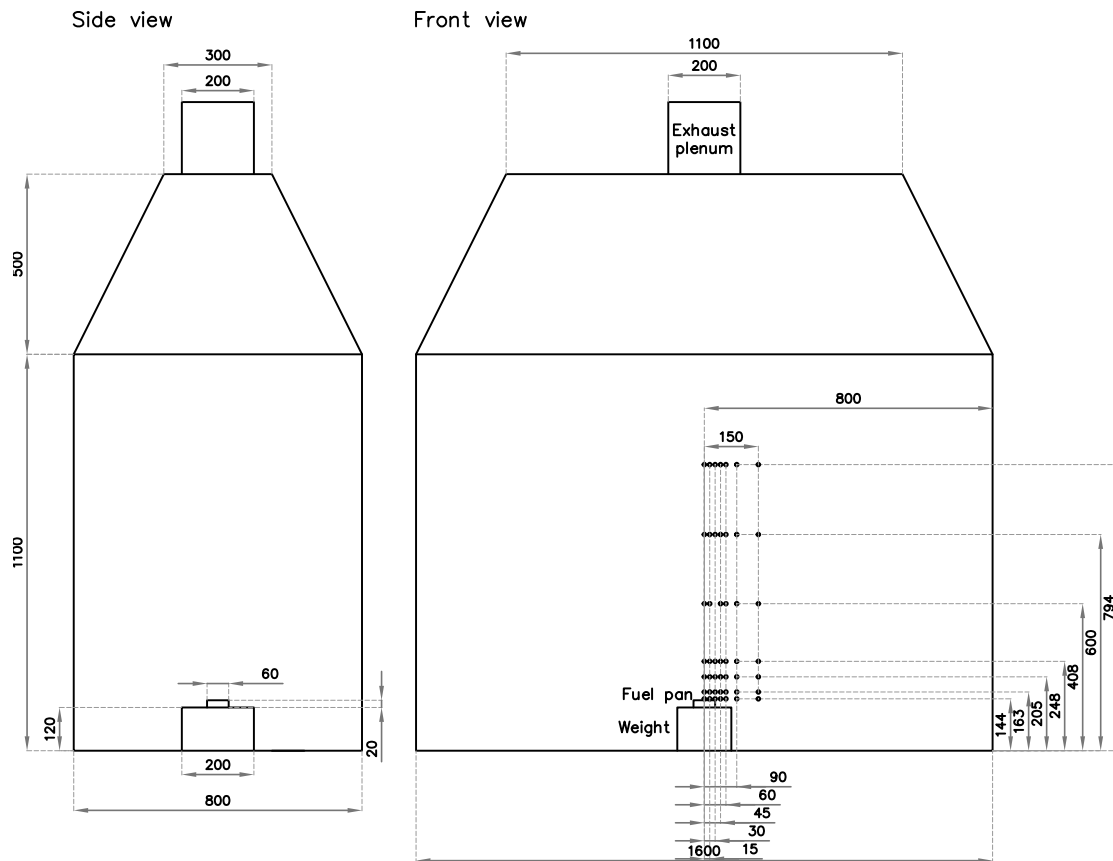


Figure 3.2: Schematic of the experiment set up considered.

The burner was disposed on the top of the weighing machine in the center of the working surface of the fume hood. A mass of 6.0 g of the fuel was added to the burner and it was ignited to start the experiment. Exhaustion was kept off during the entire experiment to prevent disturbance of the flame behavior. The fume hood was partially closed with an opening of 15 cm for safety reasons. Experiments were run in triplicates for each configuration and the generated data were averaged to check repeatability. The experimental scenario characterizes thin-layer pool fires where the liquid layer thicknesses were 3.2 mm, 2.8 mm and 2.8 mm for hexane, hydrous ethanol and gasoline, respectively.

Further details on the experimental apparatus and instrumentation are presented below:

### **3.1.2 Pan burner**

The burner consisted of a stainless steel petri dish with 60 mm diameter and 20 mm height.

### **3.1.3 Weight measurements (evaporation rate)**

The mass of the fuel was measured during the experiment by a scale device type MARTE, model AS2000C (precision 0.01 g). Data were registered manually every 10 seconds until the complete burning of the fuel.

### **3.1.4 Temperature measurements**

Temperatures were measured in seven radial distances from the pool centerline and seven heights, adding up to 49 measurement points. Two type-J and five type-K thermocouples were used. Figure 3.3 shows a schematic of the thermocouple tree that was built with the seven probes. The thermocouple three was moved along the x-axis and the experiment was repeated for seven different radial distances. Figure 3.2 shows the 49 temperature measurement positions and their positions relative to the burner centerline.

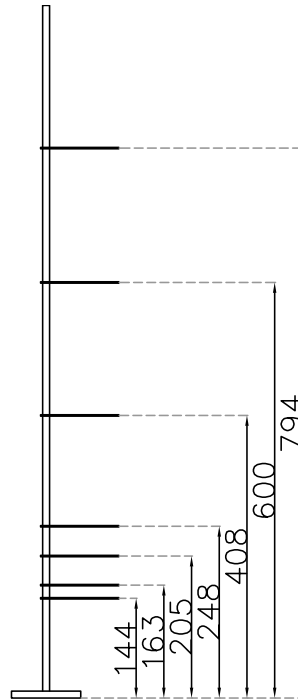


Figure 3.3: Sketch of the thermocouple tree.

The thermocouple positions were labeled according to their locations. The tags begin with letter “T” followed by a two-digit number (N-X) that represents its radial position and an one-digit number (N-Z) that represents its vertical position. N-X and N-Z indexes are presented in Table 3.2. As an example, the thermocouple located in the pool centerline ( $x=0$  cm) and height 16.3 cm is tagged T002.

Table 3.2: Indexes used for temperature tags

Axial position		Vertical position	
X (CM)	N-X	Z (cm)	N-Z
0.0	00	14.4	1
1.5	15	16.3	2
3.0	30	20.5	3
4.5	45	24.8	4
6.0	60	40.8	5
9.0	90	60.0	6
15.0	150	79.4	7

### 3.1.5 Data acquisition system

The thermocouples were connected to a data acquisition and registration module type FieldLogger/Novus. Data registration was treated with Fieldchart Lite®.

### 3.1.6 Flame height measurements

A DSLR camera, type Nikon D5200, was used in the flame height measurements. Average flame heights were obtained following the procedure of Zukoski et al. (1985). Figure 3.4 shows the used apparatus. A scale placed at the back wall of the exhaust hood allowed the measurement of the projected heights which were converted to flame heights by similarity of triangles.

Video recordings were digitally treated and a MATLAB algorithm was used to determine the position of the instantaneous upper limit of the flame. The algorithm uses a filter to separate bright and dark areas; hence, flame location is determined based on the pixel color. The time step was defined as 1 s and the fragments disconnected to the continuous flame were ignored.

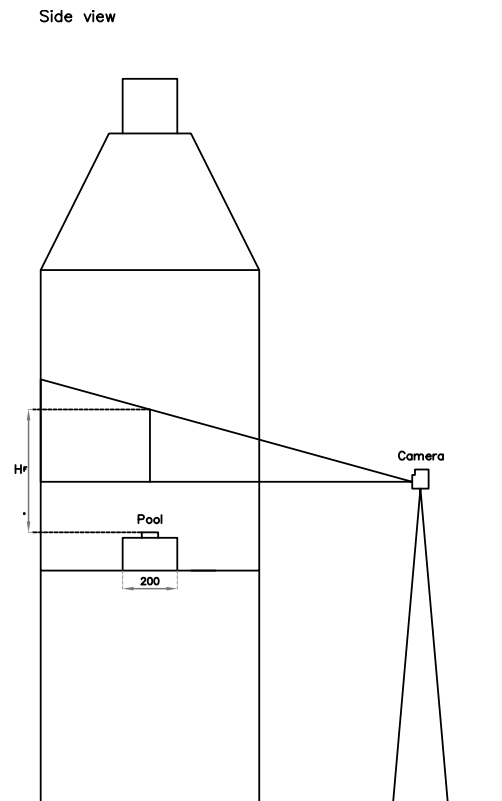


Figure 3.4: Apparatus for flame height measurement.

## 3.2 Simulations

### 3.2.1 Computational setup

The computational domain is a rectangular prism of 1.70 m in width, 0.90 m in depth and 1.60 m in height, to make sure the entire exhaustion hood was modelled. The upper part of the hood has the shape of a truncated rectangular pyramid (Figure 3.2). As FDS geometry can only be described in terms of rectangular forms, the upper part of the hood was divided vertically into 8 slices and the inclination of the walls was discretized by rectangular solids. The exhaust plenum was not modeled, but replaced by a rectangular opening at the top of the fume hood. Another opening in the front of the hood was used to model the sash window partially opened. Figure 3.5 shows the Smokeview visualization of the simulation field.

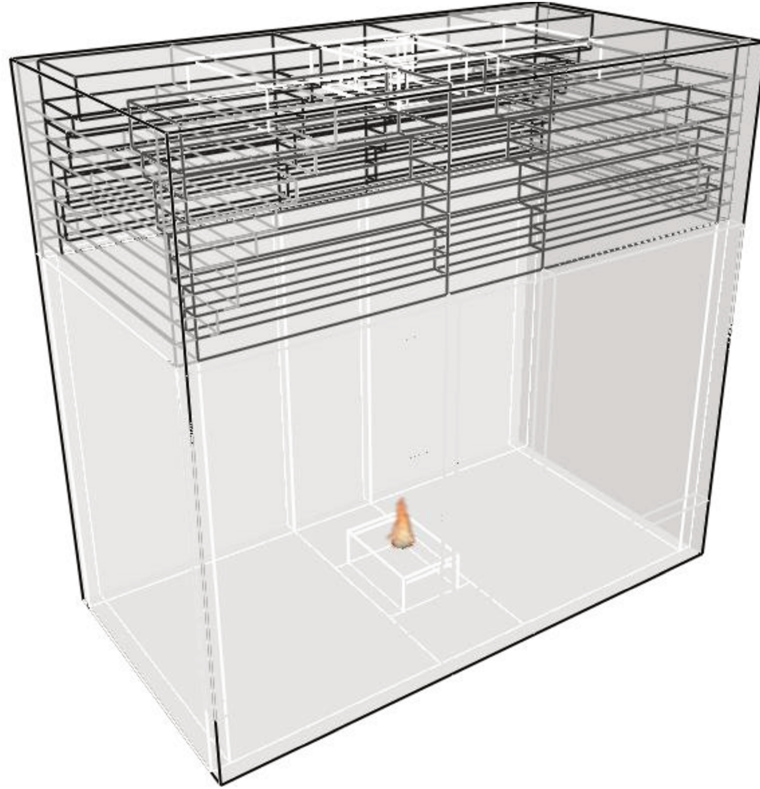


Figure 3.5: Smokeview visualization of the computational domain.

### 3.2.2 Computational Methods

The simulations were run with FDS major features in its default operation (McGrattan et al., 2015a): low Mach, large-eddy simulation (LES); explicit, second-order, kinetic-energy-conserving numerics; structured, uniform, staggered grid; simple immersed boundary method for the treatment of flow obstructions; generalised “lumped species” method; deardoff eddy viscosity subgrid closure; constant turbulent Schmidt and Prandtl numbers; eddy dissipation concept for single-step reaction between fuel and oxidizer; gray gas radiation with finite volume solution to the radiation transport equation.

### 3.2.3 Boundary Conditions

Table 3.3 show the main parameters used in each simulation. The initial temperature inside the hood body ( $T_{in}$ ) was considered as the average of the initial temperature at all thermocouples among all of the experiments performed for each fuel. The external temperature ( $T_{out}$ ) was not measured, therefore it was considered equal to the initial temperature. CO and soot yields values were taken from the Handbook of Fire

Protection Engineering - Appendix A (Hurley et al., 2015). For gasoline, CO and soot yield were obtained by the weight-average of its components properties as according to equation 3.2.1:

$$P = \sum m_i P_i \quad (3.2.1)$$

where  $P$  is the CO or Soot yield of the fuel,  $m_i$  is the mass fraction of the component  $i$  (obtained by the procedure described in Section 3.2.5) and  $P_i$  is the CO or Soot yield of the component  $i$  obtained from the literature (Hurley et al., 2015).

Table 3.3: Simulation parameters and boundary conditions

Grid	Structured, uniform, staggered grid Grid size as in table
Surface temperatures	The solid surfaces consists of smooth inert walls with temperature fixed at TMPA = (1) 29.2 °C; (2) 26.5 °C; 32.0 °C. <sup>1</sup>
Air temperatures	Surrounding temperature ( $T_{out}$ ) = (1) 29.2 °C; (2) 26.5 °C; 32.0 °C Initial temperature ( $T_{in}$ ) = (1) 29.2 °C; (2) 26.5 °C; (3) 32.0 °C
Co yield	(1) 0.009 g/g; (2) 0.001 g/g; (3) 0.017 g/g
Soot yield	(1) 0.031 g/g; (2) 0.008 g/g; (3) 0.050 g/g
External flows	Exterior boundary at the exhaustion exit and the window open were define as passive openings with outside temperatures $T_{out}$
Combustion	Fuel: (1) n-hexane; (2) 93.2% ethanol and 6.8% water; (3) 27.18% ethanol, 0.64% butane, 45.25% n-hexane, 5.01% n-octane, 4.10% dodecane and 17.82% Pool: radius 0.03 m; thickness 0.0032 m for hexane and 0.0028 for ethanol and gasoline (for LPM mode); initial temperature = $T_{in}$ ; burner material: steel; burner thickness 0.001 m.

<sup>1</sup>The indexes in Table 3.3 refer to (1) Hexane, (2) Hydrous Ethanol and (3) Gasoline

### 3.2.4 Burning rates

A default infinitely-fast reaction is used by FDS and the burning rate of a pool fire can be prescribed by the user or calculated by the software. In the first case, the user input can be given in terms of mass loss rate per unit area (MLRPUA) or heat release rate per unit area (HRRPUA). In the case of the burning rate calculated by FDS, the user must set the fuel properties and use the liquid pyrolysis model (LPM) which models the evaporation of the liquid fuel. LPM uses the Clausius-Clapeyron relation and calculates the evaporation rate by Stefan diffusion equation, as described in Section 7.2.4 of the FDS Technical Reference Guide (McGrattan et al., 2015b).

Since evaporation rates were measured directly from the experiments, the first approach is expected to be more accurate on setting the fuel burning rates. However, this approach does not take into account the heat transfer phenomena of the evaporation process. Both approaches were simulated and their agreement with experimental data are compared in Section 4.2.4.

### 3.2.5 Fuel descriptions

FDS requires the fuel properties to calculate the heat release rate per unit area (HRRPUA) and indicate how rapidly the material burns and heats up. The user can provide this properties manually or use FDS fuel library. The choice in this study was for the software library which is a more practicable way in the industry application because of the large variety of combustibles manipulated and stored in industrial units. This study will, therefore, indicate if this less precise route yields sufficient results for industrial usage.

When using the fuel library, the user need only specify the correct fuel ID and provide, if needed, the initial mass fraction. With these information, FDS uses precompiled data to compute the various thermophysical properties from 0 K to 5000 K (McGrattan et al., 2016). The library includes a list of widely used gaseous molecules such as hydrocarbons, alcohols, ketones, carbonyls, etc. In this work, Comercial hexane was described as pure n-hexane. Hydrous ethanol was simulated as a mixture of pure ethanol with 6.8% of water.

As type C gasoline is a complex mixture, a sample of the product was analyzed in an external laboratory following the ASTM D86 methodology and the obtained curve was used to determine the simulated fuel composition. A mixture of ethanol and hydrocarbons within FDS fuel library was obtained so that the distillation curve of the mixture was in accordance with the fuel analysis. Aspen HYSYS software (version 8.6), set with UNIQUAC fluid package was used for the calculation of the distillation curve of the modelled fuel. Figure 3.6 compares the D86 distillation curve for the sample of type C gasoline and the modeled fuel. The mass fraction of the molecules of the modeled gasoline is presented in Table 3.4.

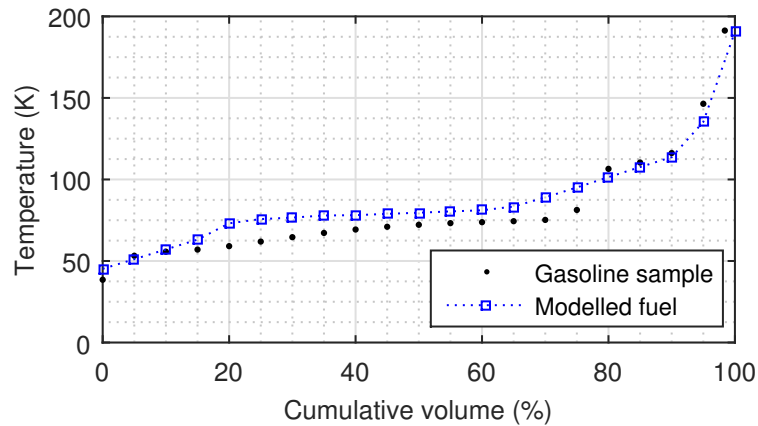


Figure 3.6: Comparison of D86 distillation curves (type C Gasoline).

Table 3.4: Modeled gasoline composition.

FDS fuel library molecule	Composition - % m/m
Ethanol	27.18%
n-Butane	0.64%
n-Hexane	45.25%
n-Octane	5.01%
n-Decane	4.10%
Toluene	17.82%

### 3.2.6 Mesh

Three different meshes were generated in order to pursue this study and Table 3.5 summarises the most important details of these meshes. The mesh grid was refined towards the centre of the domain in order to ensure a refined mesh region closer to the burner. The near field area is the region within  $0 < x < 15$  cm and  $0 < y < 15$  cm where most of the important phenomena occurs. This is also the region where all the thermocouples are located.

Table 3.5: Mesh descriptions.

Mesh	Far field mesh size (mm)	Near field mesh size (mm)	Number of cells (millions)
Coarse (C)	20 x 20 x 20	10 x 10 x 10	0.36
Medium (M)	20 x 20 x 20	5 x 5 x 5	0.80
Fine (F)	20 x 20 x 20	4 x 4 x 4	1.28

### 3.2.7 Temperature Measurement

Temperatures were calculated for the 49 positions shown in figure 3.2 using the FDS thermocouple model. The modelled temperature lags the true gas temperature due to the device’s dynamics. FDS modelling of thermocouples is described in Section 16.10.4 of FDS User’s Guide (McGrattan et al., 2016).

### 3.2.8 Flame Heights

The flame heights were obtained following the definition used in FDS Validation Guide (McGrattan et al., 2015a): “the distance above the pan, on average, at which 99% of the fuel has been consumed”. In this study flame heights were divided by the pool diameter (D) to yield dimensionless flame heights.

### 3.2.9 Mesh sensitivity analysis

Grid convergence is often used to validate results for RANS simulations and are used to show that the solution is insensitive to further refinement. Such analysis might be discussed carefully as long as LES approach is considered. Finer grids comprises greater fraction of the eddies directly calculated from the CFD fundamental equations instead of being modelled by the subgrid model. Therefore, finer grids allows the approach to rely less on the modelled part of the turbulence spectrum that is not resolved in the mesh.

Mesh sensitivity was evaluated by two criteria: the global temperature error (GTE) and the flame height. The global temperature error was defined as the arithmetic average of the differences between experimental ( $T_{exp,i}$ ) and simulated temperatures ( $T_{sim,i}$ ), as in equation 3.2.2.

$$GTE = \frac{\sum_{i=1}^{49} \frac{|T_{sim,i} - T_{exp,i}|}{T_{exp,i}}}{49} \quad (3.2.2)$$

The simulated flame heights were determined according to the definition used by FDS Validation Guide (McGrattan et al., 2015a): “the distance above the pan, on average, at which 99% of the fuel has been consumed”.

# Chapter 4

## Results and Discussion

This chapter presents the experimental work and the simulations results. In Section 4.1, the experimental results and errors are analyzed and extensively discussed. The simulation results are compared with the experimental data in Section 4.2 which leads to the analysis of how well FDS describes the studied fire scenarios.

### 4.1 Experimental work

#### 4.1.1 Evaporation results

As experiments were run in triplicates and the thermocouple tree was located in seven radial positions, 21 runs were performed with each fuel. The only exception was gasoline, for which the soot formation was intense and the laboratory was found to be inappropriate for its burning. Therefore, it was necessary to reduce the number of experiments for that fuel and the set of runs with the thermocouple tree axial position beyond 3 cm were performed only once. As a result, only 13 runs were performed with gasoline.

The mass loss data were evaluated for each experimental configuration and averaged to yield the curves shown in Figure 4.1. The statistical analysis performed by the evaluation of the standard deviations values, Figure 4.2, shows that the deviations grow with time until they reach a maximum and start to decrease. Two main reason might have caused this behavior: as mass loss rate grows, the time allowed for the mass mensuration is not enough to stabilize its value, which leads to measurement errors. Be-

sides that, human mistakes in registering the masses become more likely to happen and can lead to larger errors. In any case, the error were considered acceptable as they do not affect considerably the calculation of the burning rates.

The same behavior was observed for all analyzed fuels. Experimental errors became more important as fire grows and the mass loss rate increases. Maximum standard deviations were 0.23 g for hexane, 0.10 g for hydrous ethanol and 0.15 g for gasoline.

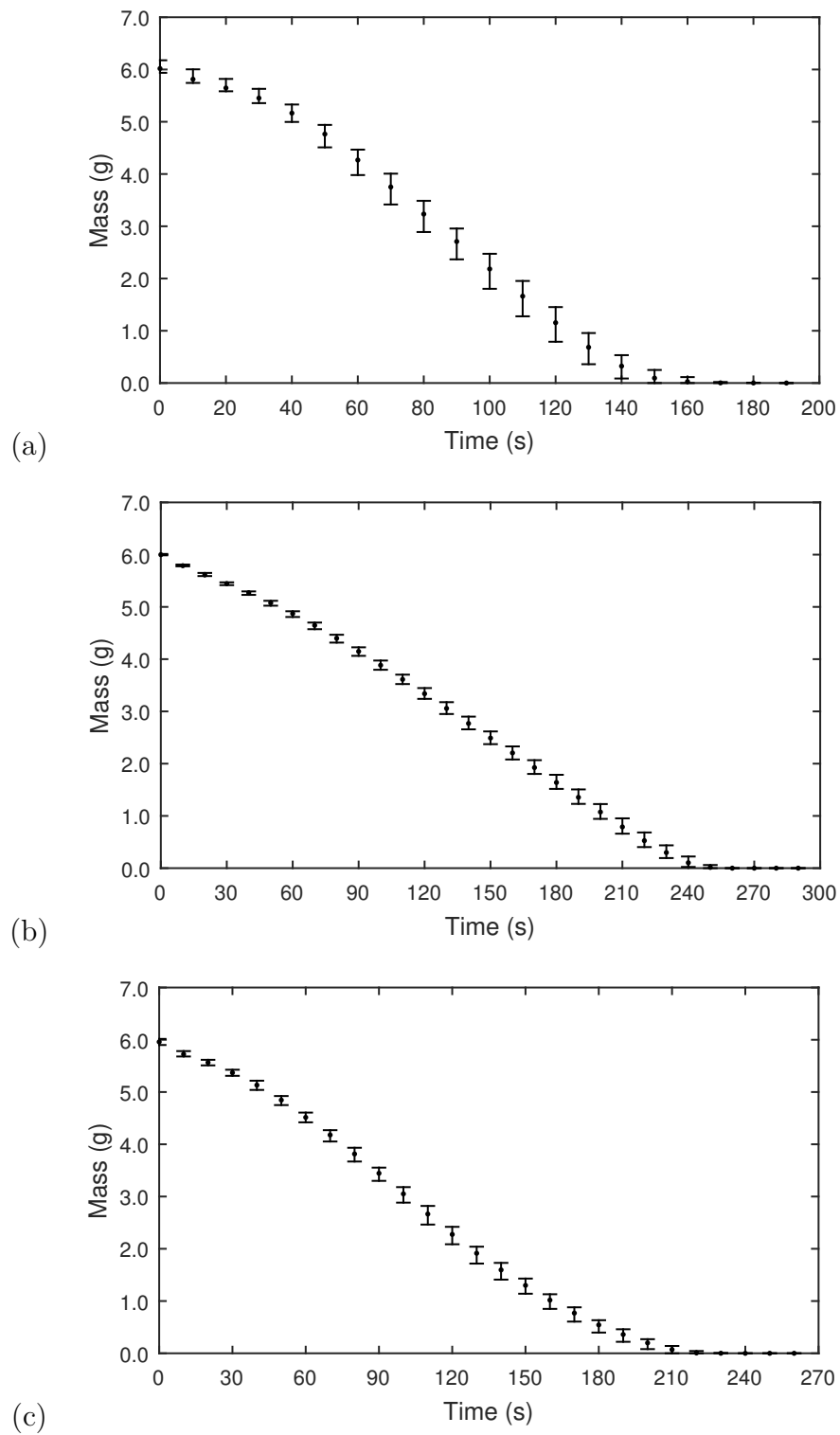
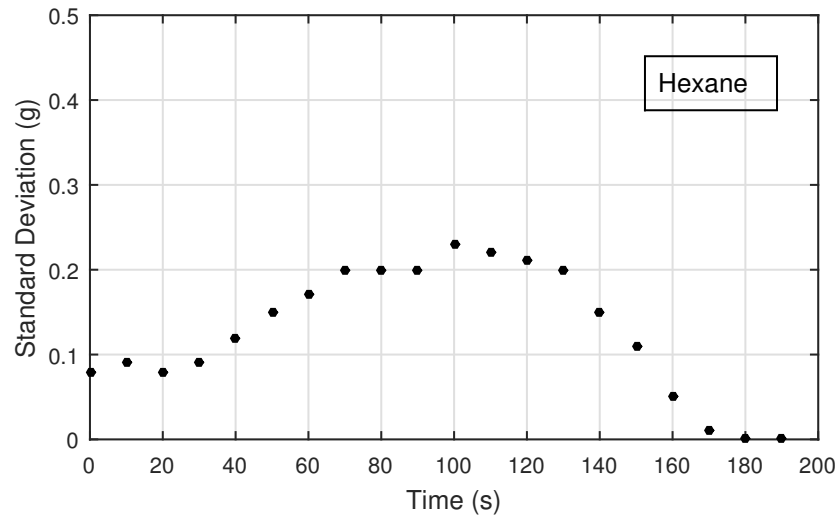
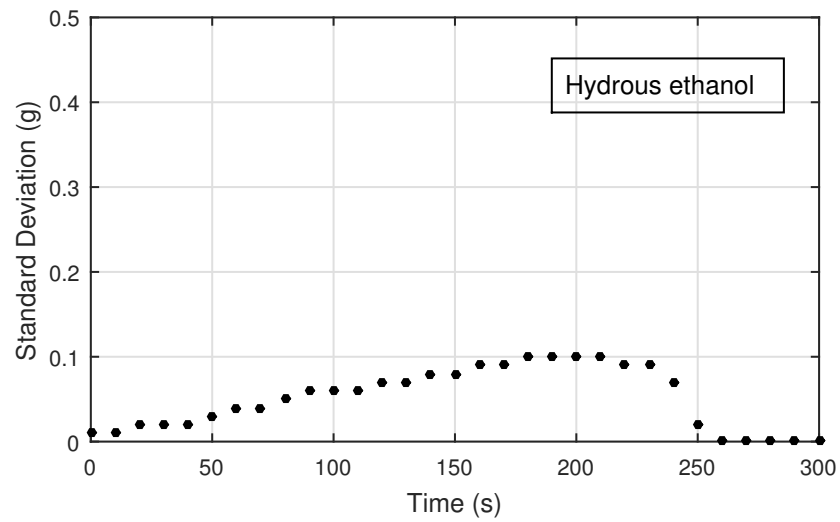


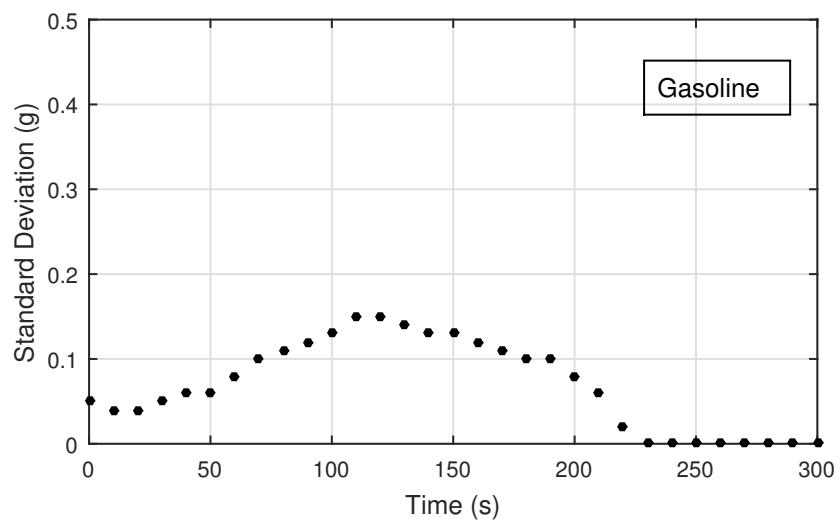
Figure 4.1: Experimental mass loss curves for the three fuels (a) hexane, (b) hydrous ethanol, (c) gasoline.



(a)



(b)



(c)

Figure 4.2: Experimental mass loss curves for the three fuels (a) hexane, (b) hydrous ethanol, (c) gasoline.

### 4.1.2 Mass Loss Rate per Unit Area

The burning rate is expressed in FDS by means of the Mass Loss Rate Per Unit Area (MLRPUA). Experimental MLRPUA was calculated from the mass measurements and plotted on Figure 4.3. The obtained curves presented the three regions described by Z. Chen, Wu, et al. (2014): a growth period, a stable burning period and a decay period.

Figure 4.3a shows a rapid increase on mass loss rate for hexane from 0 to 50 s when fire is initiated and grows. Beyond that, MLRPUA reaches its top value and is stable around that value from 50 to 120 s. Past 120 s, mass loss rate decreases continuously until the fire is extinguished.

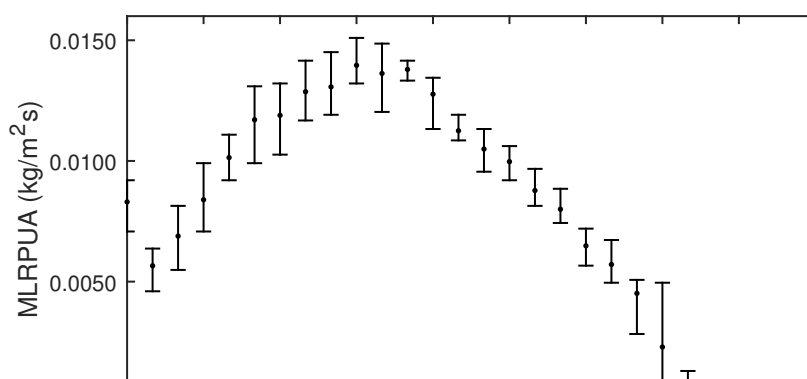
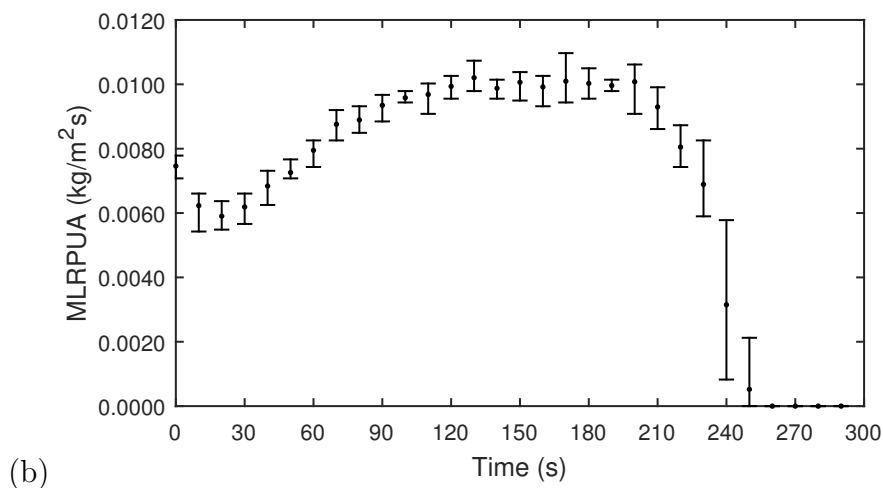
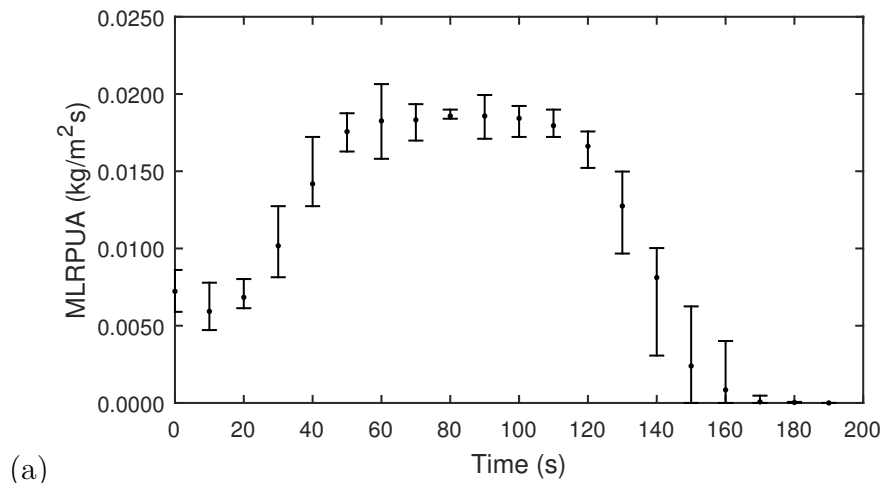
Hydrous ethanol curve (Figure 4.3b) presented a smooth growth and a moderate top value. The gasoline curve (Figure 4.3c) had a rapid climb but did not stabilize completely in the second burning stage. The complex composition of gasoline explains the less defined burning profile. This fuel has a wide distillation curve and is formed by a mixture of ethanol and hydrocarbon molecules from C4 to C12, which evaporate at different rates.

In the present work, it was not observed a second steady burning rate commonly observed in thin pool fires. The reason for that was attributed to the small thickness of the pool layer ( $< 10\text{mm}$ ).

The general results from evaporation measurements have been compiled in Table 4.1. The quasi-steady burning period was defined for each fuel and the averaged MLRPUA were calculated within this time window. Both information are shown in Table 4.1.

Table 4.1: General results of evaporation measurements

Property	Fuel		
	Commercial Hexane	Hydrous Ethanol	Type C Gasoline
Sample mass (g)	$5.98 \pm 0.03$	$6.00 \pm 0.01$	$5.96 \pm 0.05$
MLRPUA quasi-steady burning period (s)	60 to 110	120 to 200	70 to 120
Averaged MLRPUA at steady burning period ( $\text{kg}/\text{m}^2\text{s}$ )	$0.0184 \pm 0.0002$	$0.0100 \pm 0.0001$	$0.0133 \pm 0.0005$
Burnout time (s)	$157 \pm 6$	$260 \pm 4$	$230 \pm 8$



We can notice that the experimental MLRPUA values are considerably smaller than those in Table 2.2. The main reason for that is the different sizes of the fires, whereas Babrauskas reports data for large pool fires, this work's experiments are small-scale ones. Nevertheless, we can notice that the hexane flame has presented the highest experimental MLRPUA value and hydrous ethanol, the lowest, which is in accordance with the literature.

### 4.1.3 Flame height results

Figure 4.4 shows eight frames of the hexane flame during the quasi-steady burning period and illustrates the flame behaviour observed experimentally. We can notice that the flame fluctuations occur within the intermittent flame region. Other phenomena such as flame necking and flame separation can also be visualized in these frames.

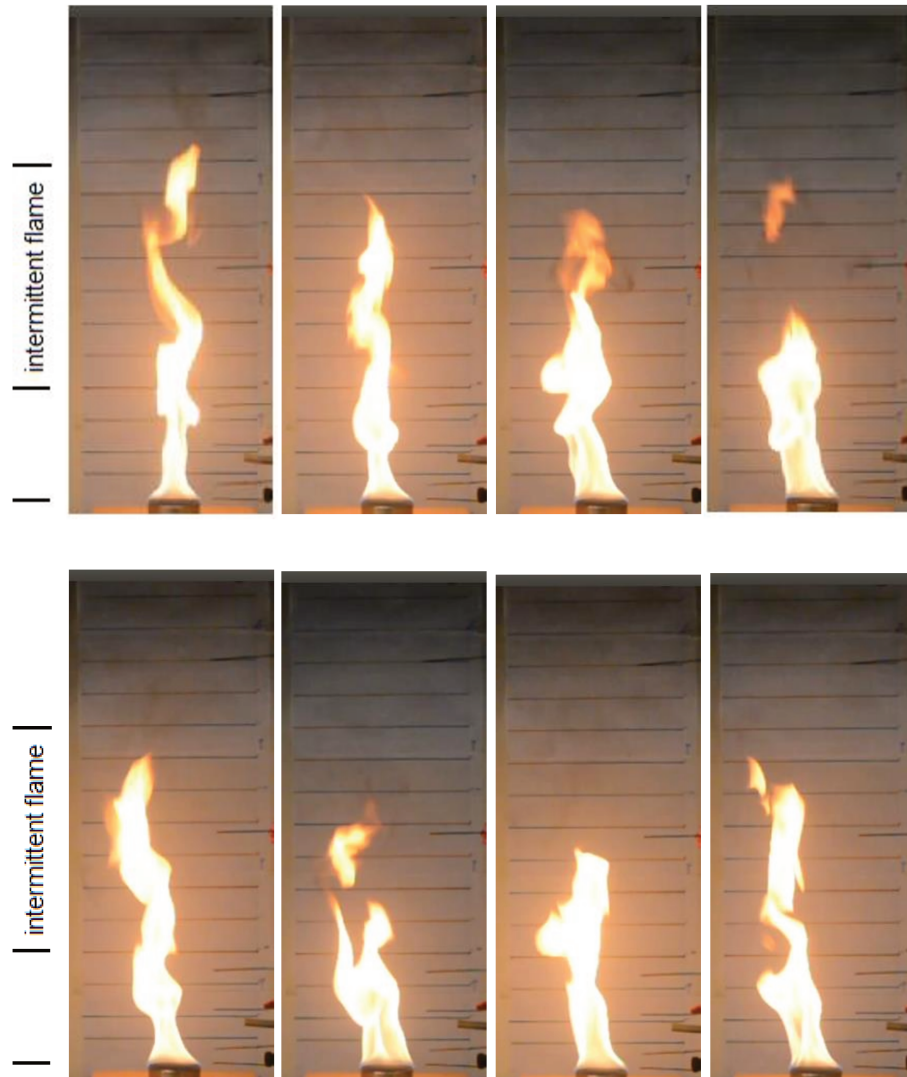


Figure 4.4: Frames of the hexane fire during the quasi-steady burning period.

The records of the flames were treated with a matlab routine (described in Section 3.1.6) to provide the intermittency data. Figure 4.5 shows the experimental intermittency curves for the tested fuels during the quasi-steady burning period.  $Z/D$  is the dimensionless flame height obtained through the division of flame height by the pool diameter and  $I$  is the intermittency. The obtained curves are compatible with the profile obtained by Zukoski et al. (1985). The intermittent zone for the hexane flame occurs between  $Z/D=2.86$  ( $I=95\%$ ) and  $Z/D=5.50$  ( $I = 5\%$ ). Hydrous ethanol flame is intermittent between  $Z/D=1.97$  ( $I=95\%$ ) and  $Z/D=3.30$  ( $I = 5\%$ ). Gasoline intermittent flame occurs between  $Z/D=2.64$  ( $I=95\%$ ) and  $Z/D=4.58$  ( $I=5\%$ ).

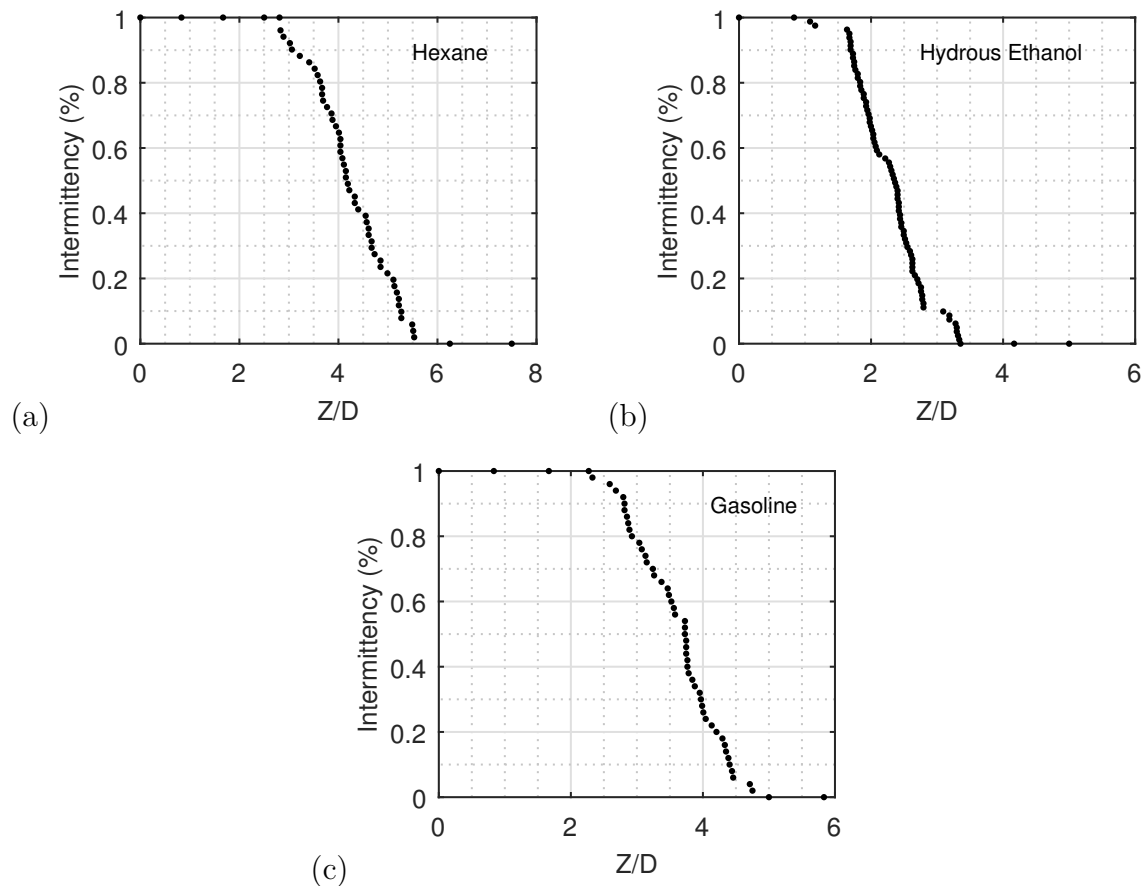


Figure 4.5: Intermittency curves for the three fuels (a) hexane, (b) hydrous ethanol, (c) gasoline.

Table 4.2 shows the flame heights obtained experimentally with the 50% intermittency method and the flame heights obtained by the Heskestad correlation. Calculated flame heights were obtained using equation 2.1.3 with the heat of combustion of similar fuels available in literature (Hurley et al., 2015) as indicated in the notes of Table 4.2. Experimental flame heights had good agreement with the Heskestad correlation, for hexane and hydrous ethanol. The experimental flame height for gasoline was 17.2% higher than the correlation. The difference between experimental and Heskestad gasoline flame heights might be associated with the complexity of the gasoline composition and the modeling strategy adopted in the correlation calculation, based on literature data. This matter will be better explored further, in Section 4.2.1.

Table 4.2: Average flame heights and heats of combustion

	Hexane	Hydrous ethanol	Gasoline
Experimental dimensionless flame height	4.17	2.35	3.73
Experimental average flame height ( $H_{fl}$ ) - cm	25.02	14.10	22.38
Heskestad flame height - cm	26.10	13.90	19.10
Heat of combustion (kJ/g)	44.7	26.8 <sup>b</sup>	43.7 <sup>c</sup>

<sup>b</sup>To account for the water content in hydrous ethanol, the heat of combustion was multiplied by 0.938 to calculate the equivalent heat of combustion:  $26.8 \times 0.938 = 25.1$  kJ/g.

<sup>c</sup>To account for the ethanol content in gasoline, the equivalent heat of combustion was obtained by mass averaging the heat of combustion for gasoline and ethanol:  $0.75 \times 43.7 + 0.25 \times 26.8 = 39.5$  kJ/g.

#### 4.1.4 Temperature results

One major issue associated with experimental studies of laboratory-scale pool fires is the difficulty of obtaining accurate measurements in the developing region of the fire. Large temperature variations are normally established within the flame envelope. Furthermore, thermal equilibrium is not fully achieved and the measured temperature may not be the actual one.

According to Weckman & Strong (1996), uncertainties as high as 25%-30% are associated with using thermocouples to obtain measurements of fluctuating temperatures. This is a consequence of the thermal inertia of the thermocouple bead that leads to a phase lag and amplitude attenuation of the thermocouple signal. In pool fires, temperature undergoes large, cyclical fluctuations with time. However, in the absence of a practical alternative, wire thermocouple measurements remain a crucial tool for characterizing the fire profile. It must be considered though, that high uncertainties may be associated with those measurement points located at the developing region of the fire.

The great difficulties associated to the measurement of the flame temperature is one of the reasons why experiments were run in triplicates. Figure 4.6 shows examples of the experimental temperature curves obtained for the hexane flame. The triplicate curves obtained for each measurement point had the same general behavior and devia-

tions were attributed the random behavior of the flame.

Good reproducibility was obtained for most of the triplicate pairs. However some curves present peaks that differ strongly from other runs (see curve T002-2 at 40s in Figure 4.6a). This might be caused by minor experimental disturbances and the random behavior of the flame.

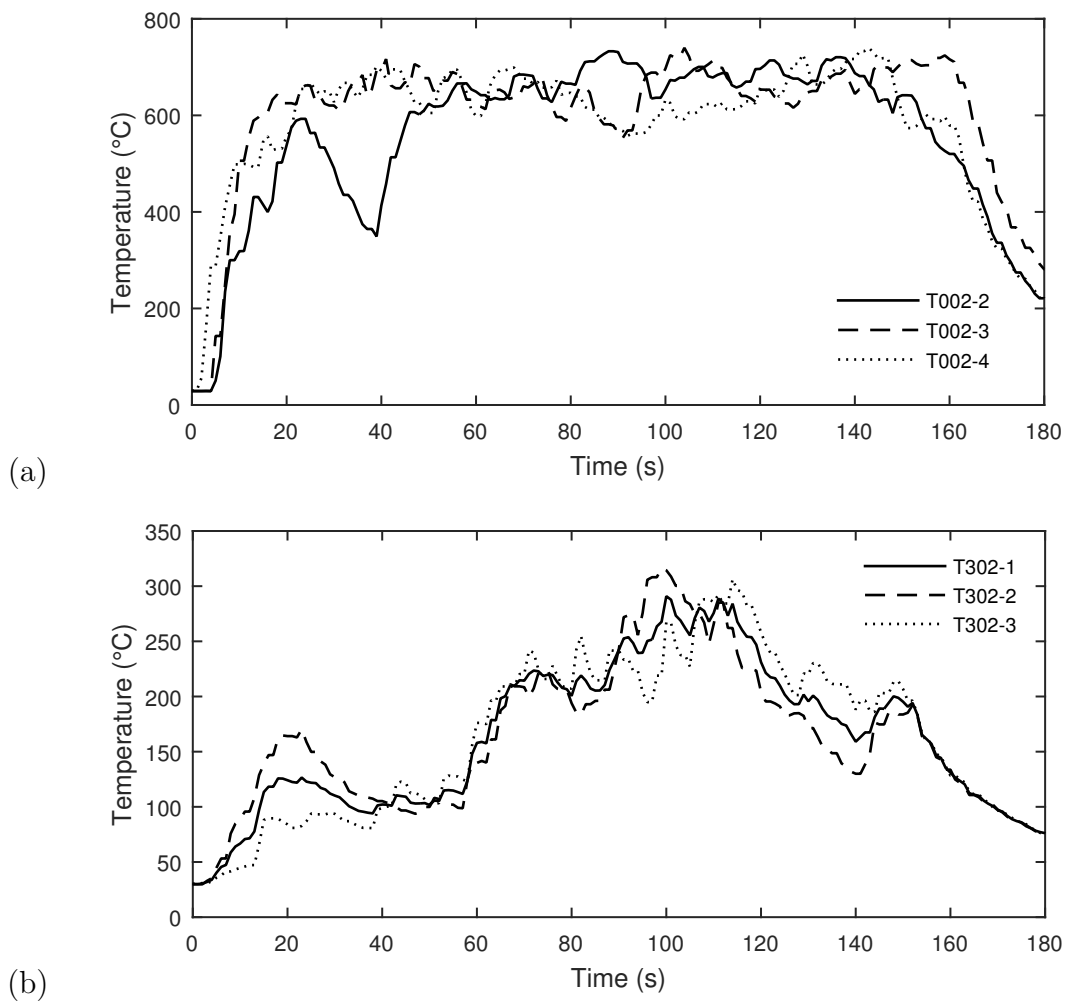


Figure 4.6: Experimental temperature measurements at positions (a) T002 and (b) T302.

To reduce the effect of aleatory experimental disturbances and provide the average behavior of the temperature field, each measurement point was associated with one single time-averaged temperature. Figure 4.7 shows the process to obtain the time-averaged temperatures. First, we calculated the average temperature within the quasi-steady burning period for each triplicate curve. Then we calculated the average of these

averages and the standard deviation among them.

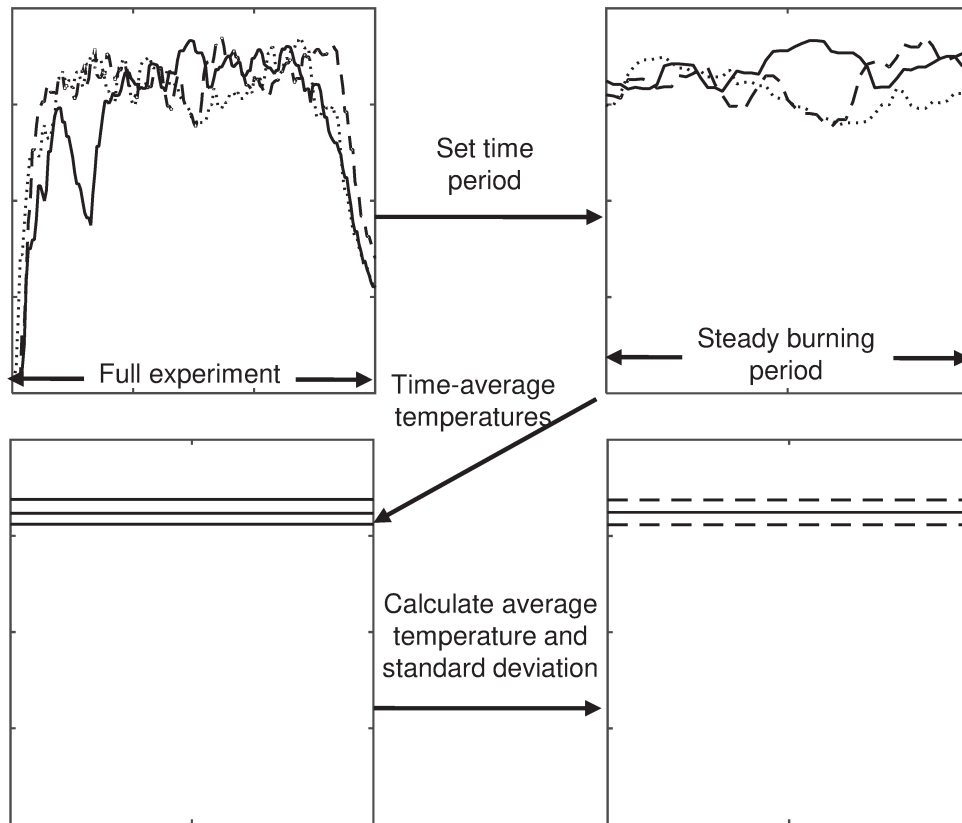


Figure 4.7: Process to obtain time-averaged temperatures.

The statistical analysis performed by plotting the standard deviation against the average temperature for all measurement points is shown in Figure 4.8. For the tested fuels, most standard deviation values lay below 20%, however, higher values are observed in some points.

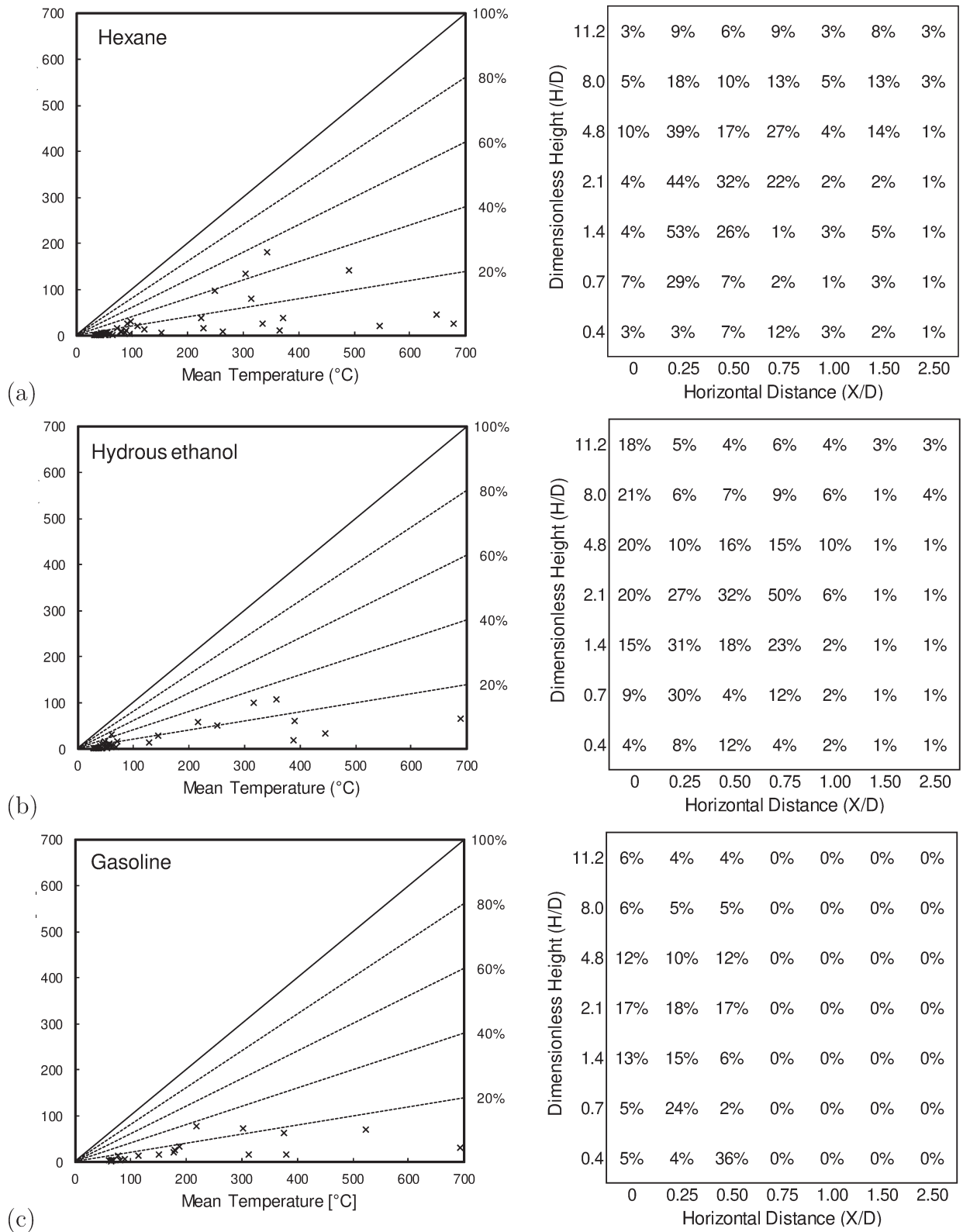


Figure 4.8: Temperature standard deviation analysis for (a) hexane, (b) hydrous ethanol and (c) gasoline.

The right side of Figure 4.8 shows the percentage ratio of standard deviation

and average temperature values for the 49 measurement positions. Note that gasoline presented no deviations for points between  $X/D = 0.75$  and  $2.5$ , as these experiments were run only once. As discussed before, the points within the developing region of the fire were associated with the greater difficulty for the temperature measuring; as a consequence this points had largest standard deviations. Maximum deviation in hexane experiments reached 53% at measurement point T203. Ethanol experiments deviations reached 50% at T454. Gasoline presented lower deviation values, reaching a maximum of 36% at T301.

Hexane produced the most unstable flame, which is a probable reason why it was associated with the highest standard deviations. For the three fuels, it is noticeable that the deviations are lower at points more distant from the flame. Maximum deviations occur at distances  $X/D = 0.25$  and  $X/D = 0.50$ .

The present work did not intend to study the time dependent behavior of the temperatures, only the mean temperatures at the quasi-steady burning period were analyzed. Despite that, Appendix A presents the mean temperature history curves, which were obtained by the averaging of the triplicate measured curves.

Figures 4.9-4.14 show the mean temperatures within the quasi-steady burning period grouped by two different ways. On figures 4.9, 4.11 and 4.13, the temperature results are grouped by their heights ( $Z/D$ ), whereas 4.10, 4.12 and 4.14 show the same results grouped by axial positions ( $X/D$ ). The error bars in these figures indicate the maximum and minimum values obtained among the triplicate data.

Analysis of Figure 4.9 shows that the highest temperatures in the hexane experiments were reached at the centerline and decreased with the distance to the fire for all heights. The vertical profiles (Figure 4.10) however, changed considerably with the axial distance ( $X/D$ ). The centerline ( $X/D=0$ ) was characterised by a lower temperature near the burner exit which increased until it reached a maximum value that oscillates between  $Z/D=0.7$  and  $Z/D=2.1$  and then it decreased with the increase in height.

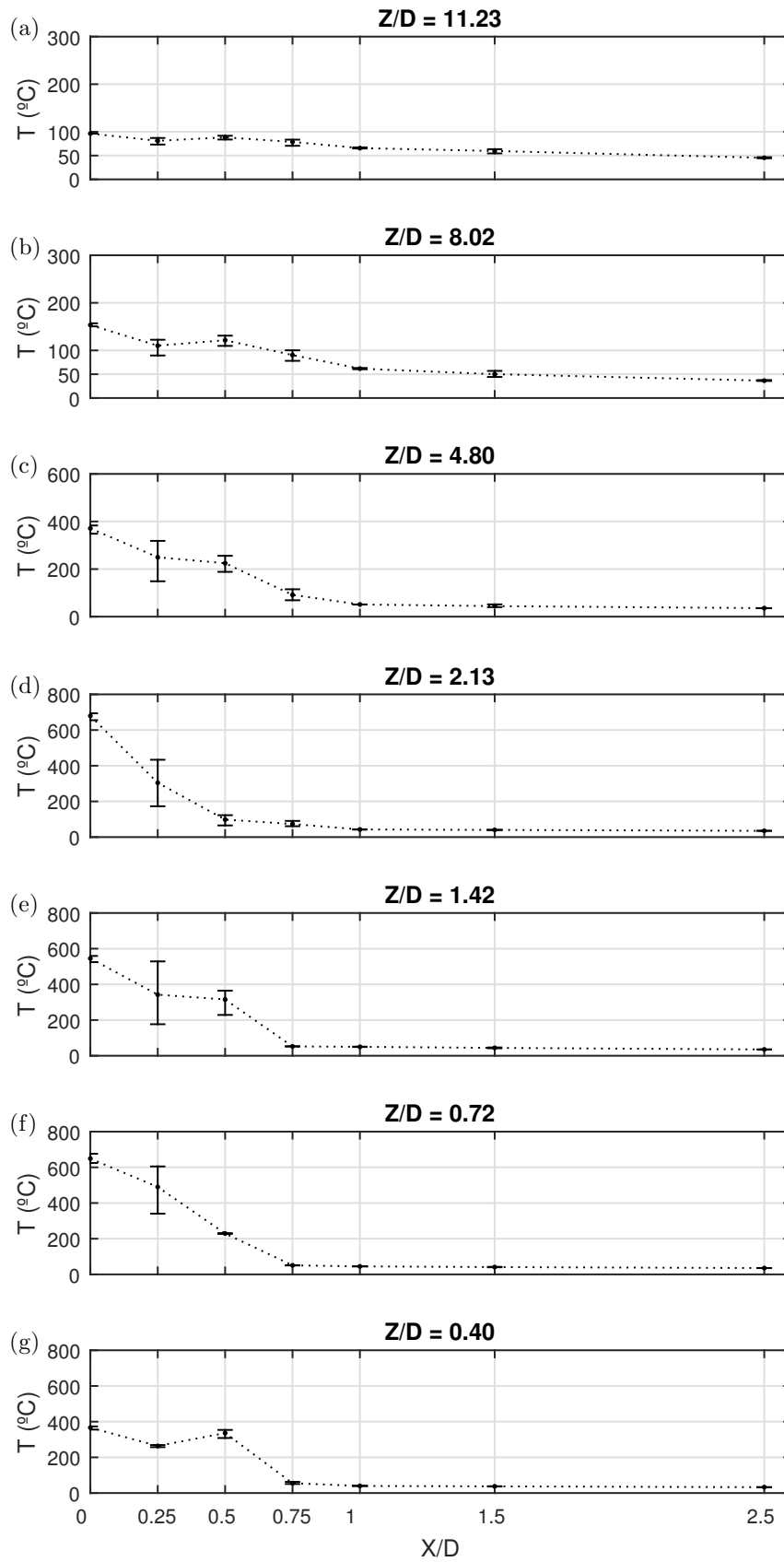


Figure 4.9: Mean temperatures for hexane experiments during steady burning period (from  $t = 60$  s to  $t = 110$  s) - Horizontal profiles.

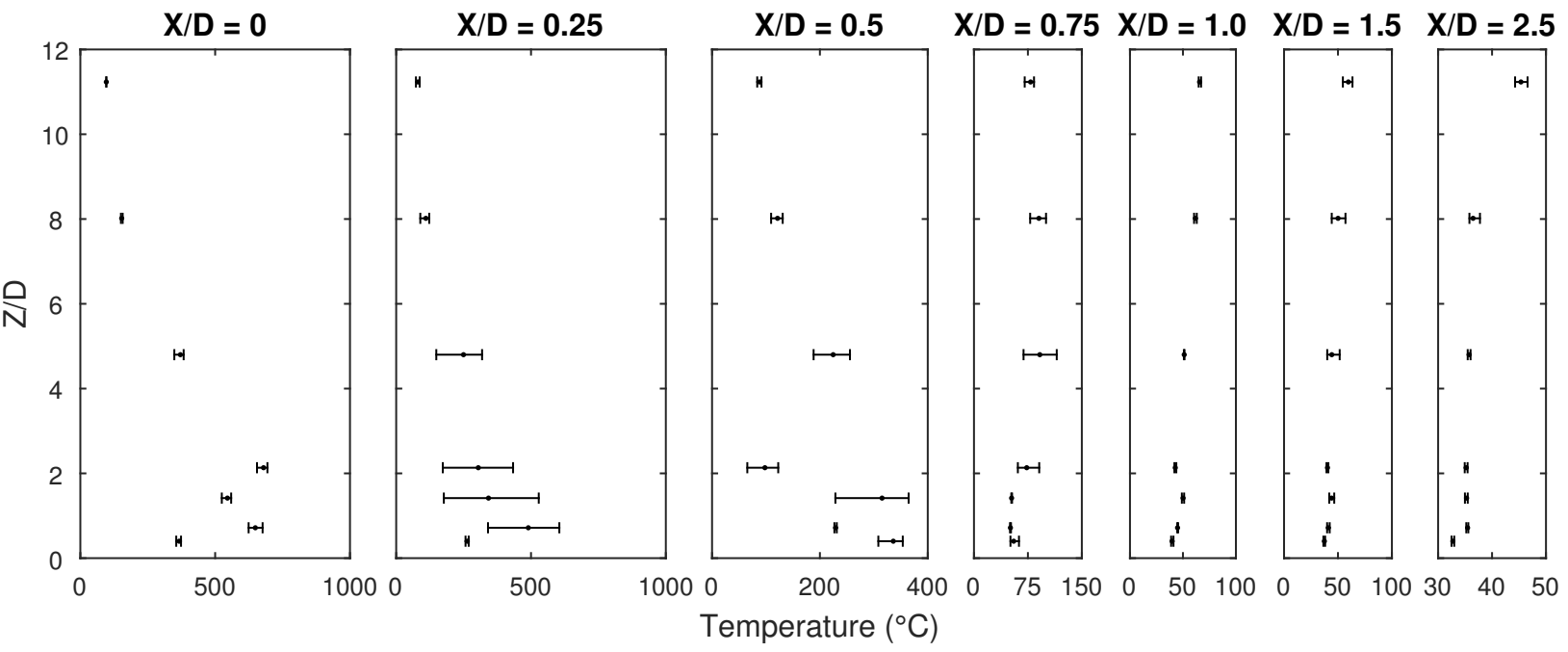


Figure 4.10: Mean temperatures for hexane experiments during steady burning period (from  $t = 60$  s to  $t = 110$  s) - Vertical profiles.

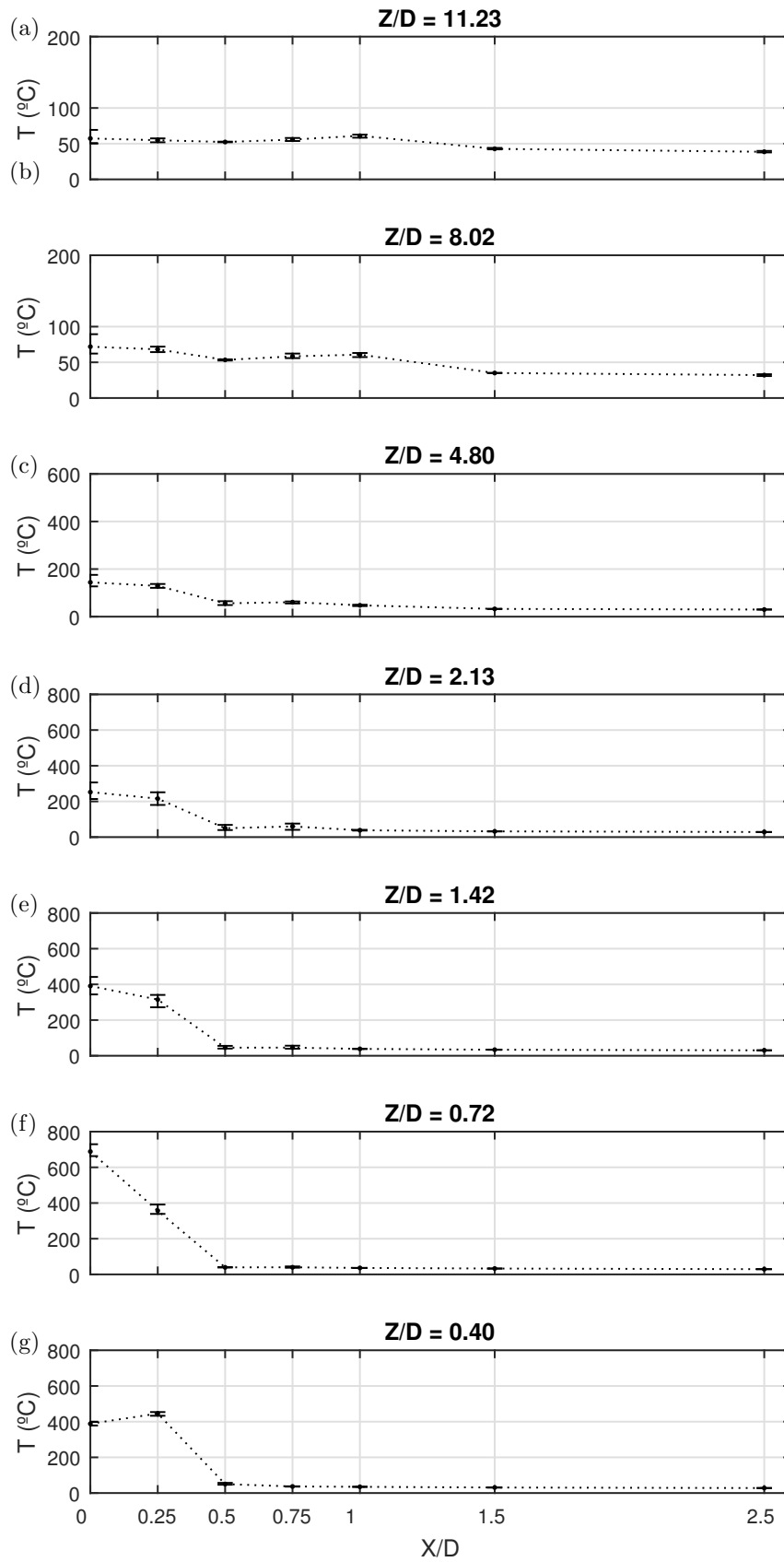


Figure 4.11: Mean temperatures for ethanol experiments during steady burning period (from  $t = 120$  s to  $t = 200$  s) - Horizontal profiles.

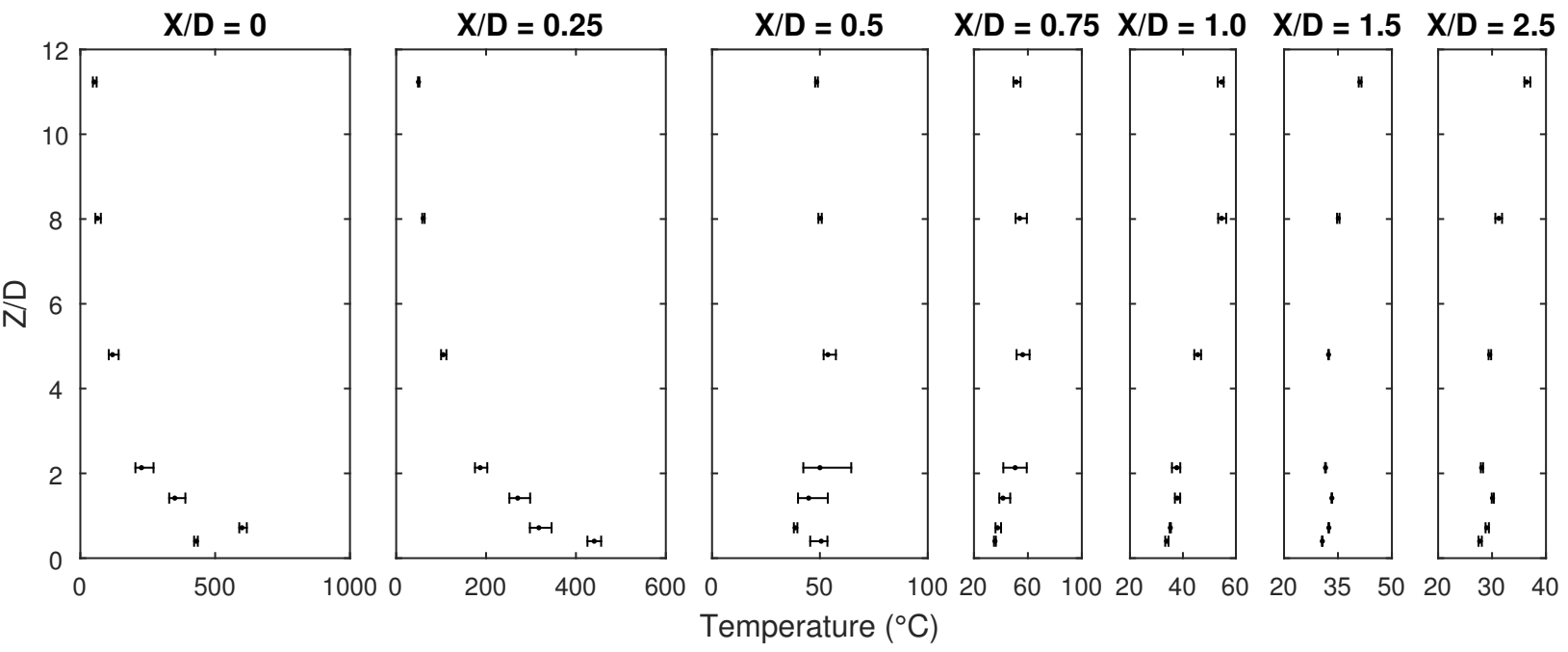


Figure 4.12: Mean temperatures for ethanol experiments during steady burning period (from  $t = 120$  s to  $t = 200$  s) - Vertical profiles.

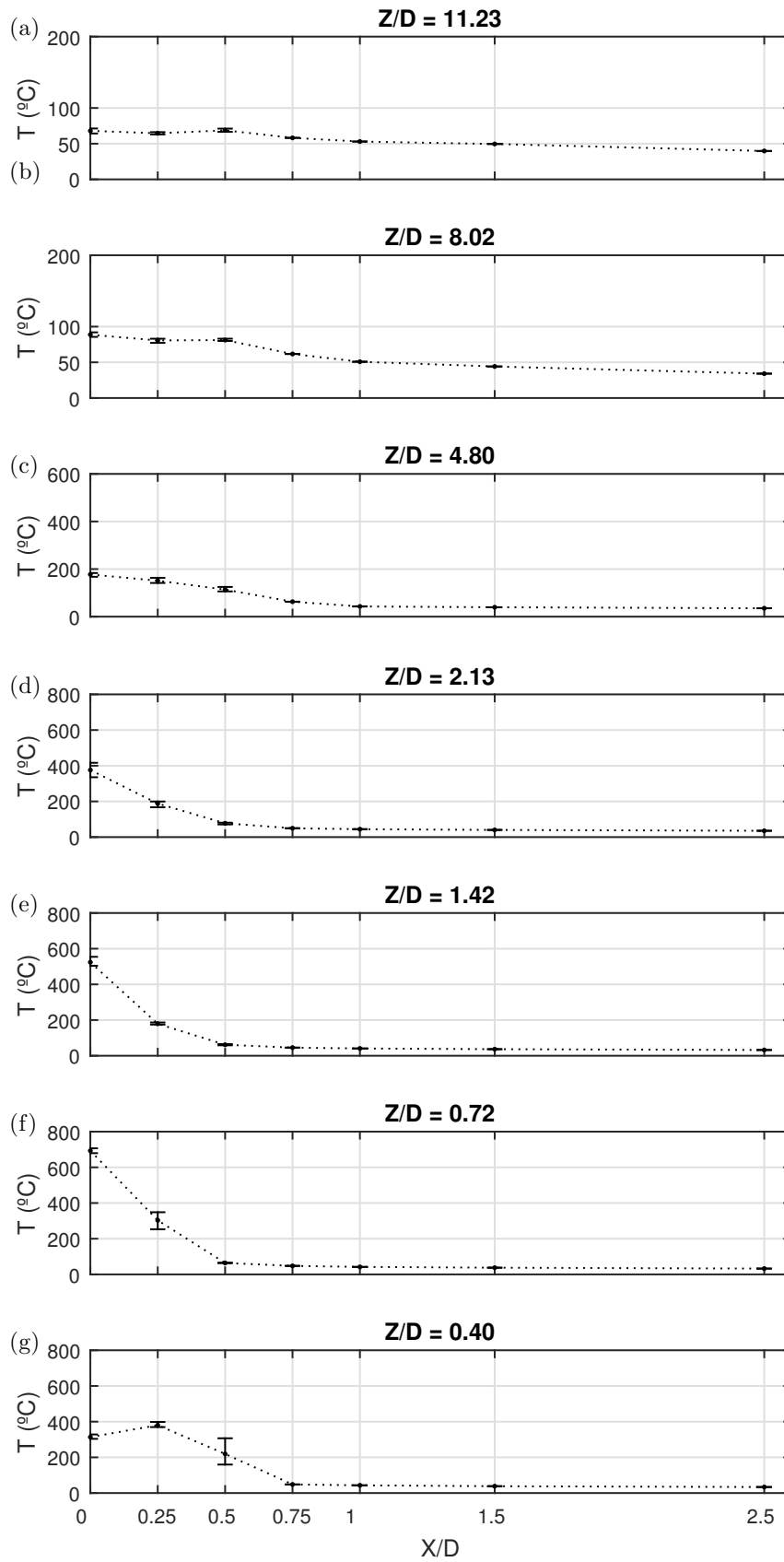


Figure 4.13: Mean temperatures for gasoline experiments during steady burning period (from  $t = 70$  s to  $t = 120$  s) - Horizontal profiles.

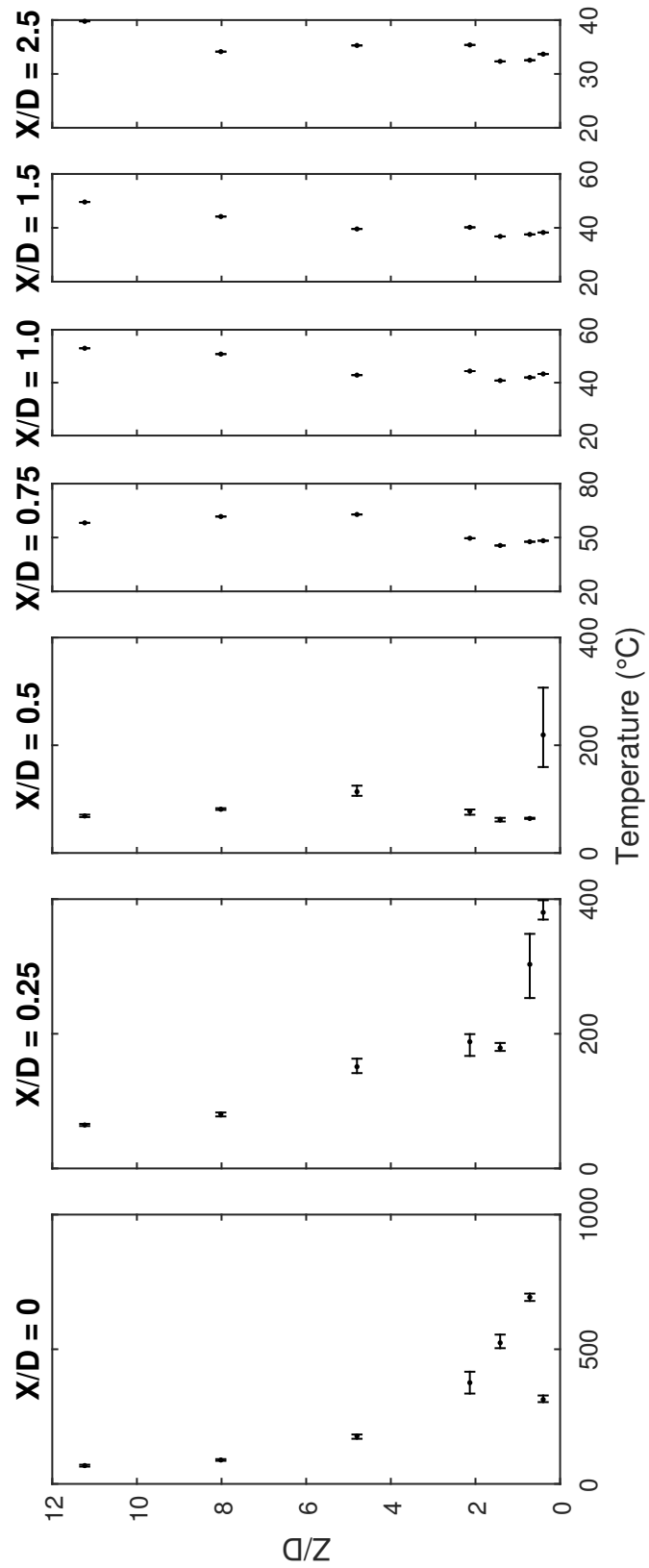


Figure 4.14: Mean temperatures for gasoline experiments during steady burning period (from  $t = 70$  s to  $t = 120$  s) - Vertical profiles.

In intermediate axial distances within the pool radius ( $X/D = 0.25$  and  $0.5$ ),

maximum temperatures laid between  $Z/D=0.4$  and  $Z/D=1.4$ . However, at the pool boundary ( $X/D=0.5$ ), a pronounced reduction of temperature was observed at  $Z/D=2.1$  and the temperature rose again at  $Z/D=4.8$ . Above this point, temperature decreases with height. Analysis of the intermittency curve for hexane (Figure 4.5) shows that the low temperature area observed at  $Z/D=2.1$  is in the upper part of the continuous flame zone, where flame necking occurs, which might explain the temperature minimum at this height.

Another approach that might justify this profile is attributed to the movement of the hot gases in the intermittent zone. Considering only the conductive heat, temperature should decrease with height in the upper part of the intermittent zone and in the plume zone, as the heat source, i.e. the region where the combustion reaction takes place, becomes more distant. However, the gases formed in the flame by the combustion reaction move upwards, and mix with the air by convection in a three-dimensional movement causing efficient heat exchange in this area. The result is that heat is more efficiently dissipated and the temperature profile is flatter. In fact, Figure 4.9 shows that the temperature curve is very sharp at  $Z/D = 2.13$  but it becomes flatter for  $Z/D > 4.8$ . This could explain why the temperature rises at  $Z/D=4.8$  in the pool boundary: the effect of convection is more relevant in this region than at  $Z/D = 2.13$ .

The effect of convection was observable in regions far from the flame ( $X/D > 0.5$ ). Figure 4.10 shows that the peak temperature moved up with the increase of the radial distance: at  $X/D = 0.75$  profile the peak temperature occurs at  $Z/D = 4.8$ , whereas at  $X/D = 2.5$  profile, the maximum temperature occurs at  $Z/D = 11.23$ . This is also associated with the earlier discussion about the flatter profiles observed for  $Z/D > 4.8$  in Figure 4.9.

Figure 4.15 presents a temperature map for hexane in the XZ plane, obtained by plotting the mean temperature values with ParaView® (Ahrens et al., 2005), a data analysis and visualization application that uses linear interpolation to build a color map for a data field. In Figure 4.15, ParaView output was mirrored to simulate a full cross section at the flame center.

The temperature profile presented a higher temperature region formed at the pool base that becomes more concentrated in the centerline with height. A temperature neck was noticeable around 12 cm height ( $Z/D = 2$ ). Between  $Z/D = 3$  and  $Z/D = 7$ , the higher temperatures are less concentrated in the centerline, as the predominant means of heat transfer transits to convection, which leads to a three-dimensional heat spread. The flame neck formation, which occurs in the upper part of the continuous flame, might also be caused by the flame instability in the intermittent area, where flame separation constantly occurs and the flame might move away from the centerline depending on instantaneous oxygen availability. As a consequence the reaction is less concentrated in the centerline and the temperature profile is flatter in this region.

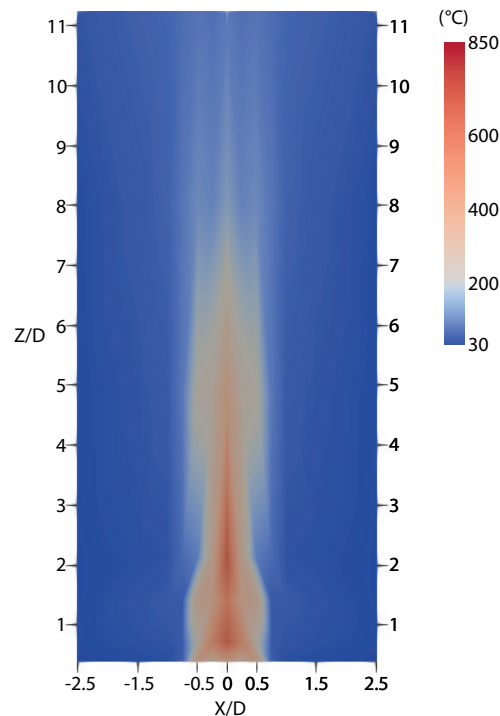


Figure 4.15: Experimental temperature map (hexane).

Figures 4.11 and 4.12 present the ethanol mean temperature plots. General behavior was similar to the hexane flame: maximum temperatures are concentrated in the centerline, but temperatures decreased more rapidly with height and maximums were more moderate and occurred at lower heights ( $Z/D=0.40$  to  $0.72$  cm). A second temperature peak occurred at  $Z/D=4.8$  for the radial distances of  $0.5$  and  $0.75$  (Figure 4.12), similarly to what was observed for the hexane flame. Beyond  $X/D = 0.75$ , the peak temperatures moved up as radius distance increased.

The mean temperature map for ethanol is presented in Figure 4.16. The temperature map suggests a stable flame with smooth spatial distribution of temperatures.

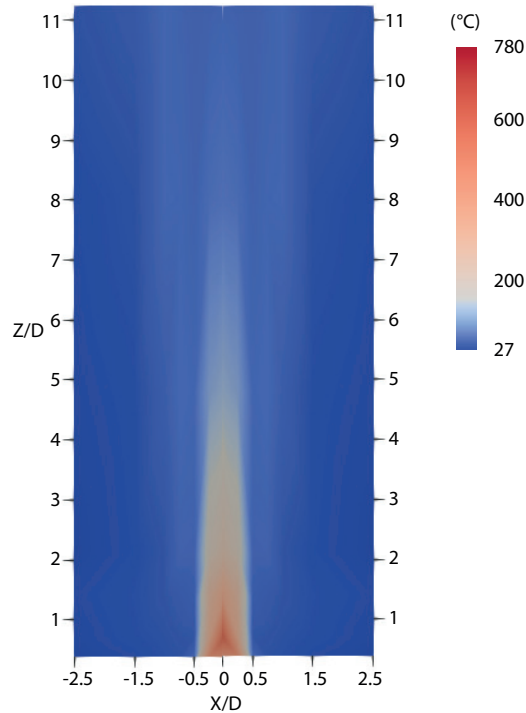


Figure 4.16: Experimental temperature map (hydrous ethanol).

Gasoline mean temperature plots are presented in figures 4.13 and 4.14. The general behavior was similar to the hexane and the ethanol flames. The highest temperatures were concentrated at the centerline. The temperatures decreased with height for small radial distances and it increased with the elevation for the largest radial distances. For radial distances higher than  $X/D = 0.5$  temperatures present a peak of temperature at  $Z/D = 4.8$ .

Gasoline presented a smooth and elongated temperature distribution as shown in Figure 4.17.

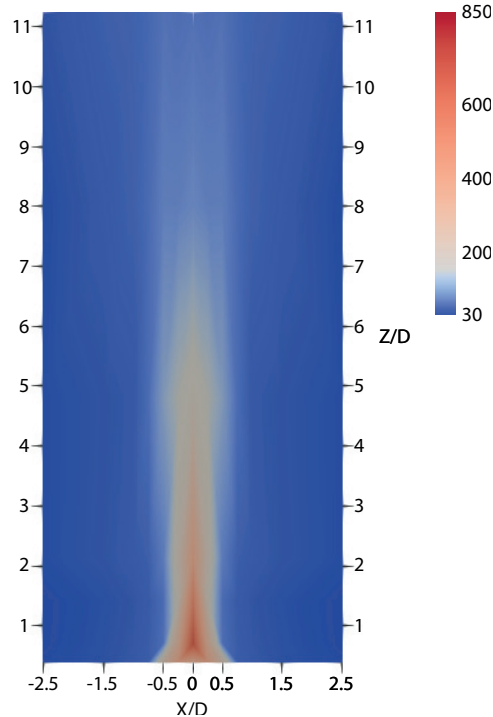


Figure 4.17: Experimental temperature map (gasoline).

## 4.2 Simulation results

FDS simulations were compared with experiments presented in Section 4.1. The main purpose of these simulations was to investigate how well FDS model predicts the pool fires, comparing the results for temperature field and flame heights. Section 4.2.1 compares the simulation outputs when MLRPUA was defined by the user with the experimental results. Section 4.2.2 discusses the influence of CO and soot modelling in the simulation results, whereas Section 4.2.3 investigate the roll of the sub-grid scale turbulence modelling. Finally, Section 4.2.4 analysis the results when the liquid pyrolysis model (LPM) is used.

### 4.2.1 Prescribed MLRPUA results

The simulations were performed with a prescribed MLRPUA, which means that the gaseous fuel liberated from the pool fires was defined by the user. To do so, the experimental MLRPUA curves from Figure 4.1 were used as an input parameter to FDS; thereby, these simulations were called “prescribed MLRPUA”, in contrast to the

“calculated MLRPUA” simulation discussed in Section 4.2.4. It is worthy noting that the heating up of the liquid fuel and the evaporation are neglected in this approach. No ignition source is needed in the modelling as FDS will burn any fuel gases regardless of that. Thus, as long as a liquid fuel is specified, the fuel begins burning at once (McGrattan et al., 2016).

Mesh sensitivity was evaluated by the simulated flame heights. Figure 4.18 shows that the simulated flame heights has an asymptotic behaviour showing better convergence with the experimental data for the finest meshes.

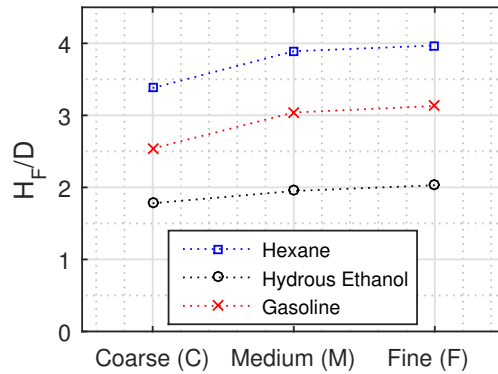


Figure 4.18: Simulated flame heights.

As shown in Table 4.3, the simulations times increase considerably with the mesh refinement. The medium (M) mesh took 58 to 59% less CPU time than the fine (F) mesh, which is a consequence of the lower number of computational cells. Among the simulations, the medium mesh (M) was selected to undergo a more detailed temperature analysis due to its good response in comparison with the computation cost involved.

Table 4.3: Computational cost

Mesh	Processors	Total CPU time (h)		
		Hexane	Hydrous ethanol	Gasoline
Coarse (C)	4	43.1	57.4	41.0
Medium (M)	4	306.7	448.3	299.6
Fine (F)	4	737.1	1,070.3	727.1

Figure 4.19 compares the simulated flame height with the experimental data and the calculated height obtained with Heskestad correlation. The differences between the experimental and numerical results with the fine (F) mesh for hexane, hydrous ethanol and gasoline were 5%, 14% and 16% respectively.

Gasoline simulated flame height has a better agreement with the Heskestad calculation than with the experimental data. The description of gasoline used in both Heskestad and FDS calculations was modelled as a composition of simple substances which yields a distillation curve similar to the experimental. This result suggests that the differences between experimental and simulated values might be due to the modelling approach to describe the fuel rather than a failure in FDS and Heskestad calculations. It is possible that if these calculations are made based on an experimental analysis of the gasoline sample, such as heat of reaction, specific heat, absorption coefficient and boiling temperature, both FDS and Heskestad results could have better agreement with the experimental data.

The global temperature error provides an overview of how FDS simulations correlates with experimental data. GTE values for the Medium (M) mesh simulations is shown in Table 4.4. The hydrous ethanol simulations presented lower GTE value compared to hexane and that gasoline simulations presented the highest GTE value. The high GTE values observed for all fuels ( $> 39.4\%$ ) imply that the predicted temperatures have large quantitative differences with the experimental data. As discussed earlier temperature measurements in laboratory-scale pool fires are normally associated with high errors caused by the large temperature variations within the flame envelope. This could explain partially why GTE values reach the order of magnitude shown in Table 4.4. The qualitative behaviour of simulated temperature profile and the analysis of which points and regions presented better agreement between simulated and experimental temperatures will be discussed further.

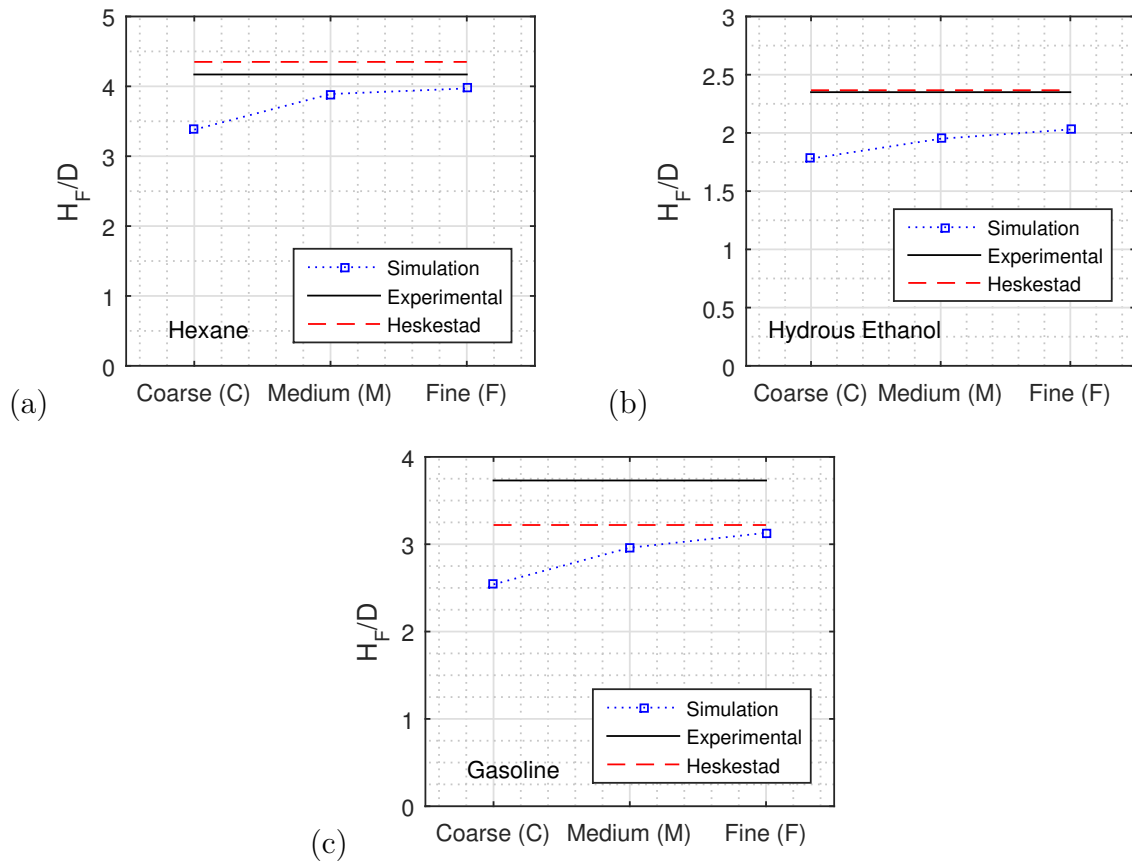


Figure 4.19: Comparison of simulated, experimental and Heskestad flame heights (a) hexane, (b) hydrous ethanol, (c) gasoline.

Table 4.4: Global Temperature Errors (GTE)

Fuel	GTE (%)
Hexane	40.7
Hydrous ethanol	39.4
Gasoline	53.6

Figures 4.20, 4.21 and 4.22 show the comparison of experimental and the simulated temperature profiles with the medium (M) mesh. Analysis of the temperature fields shown in these figures reveals that the qualitative behavior of the pool fires was well captured by FDS. However, the simulations overpredicted the temperatures at most of the measurement points, which justify the high GTE values discussed earlier.

The temperature profiles change with the radial distance. The simulated pro-

file in the centerline for the hexane flame, shown in Figure 4.20, is characterized by a lower temperature near the burner exit which increases until it reaches a maximum value at  $Z/D = 1.4$  and then it decreases with height. The experimental and simulated temperatures follow the same trend, however, the simulation reaches higher values (up to 804 °C) than the experiment (maximum of 679 °C).

At a radial distance ( $X/D$ ) of 0.5, the experimental temperature reached its maximum value and oscillated between  $Z/D=0.4$  and  $Z/D=1.4$ . A pronounced neck was observed at  $Z/D=2.1$  and the temperature reached a second peak at  $Z/D=4.8$  above which temperature decreased again. The simulation presented an oscillation at  $Z/D=1.4$ , however it was considerably less pronounced than the neck observed in the experimental profile. In the far field ( $X/D > 1.5$ ) both experimental and simulated temperatures presented similar trends.

Large deviations between experimental and simulated temperatures occurred in radial distances near the pool rim, between  $X/D=0.25$  and  $X/D=0.50$  and heights below  $Z/D=5.0$ . This region comprises the continuous and intermittent zones for the hexane flame. As discussed in Section 4.1.4, the randomic behavior of the flame and the flame tilting is believed to cause high oscillations on the temperatures in this region. As a consequence, it was also observed that this region presented high experimental errors.

We must also consider that FDS attributes one single temperature value for each computational cell, therefore, cells with high temperature gradient will be associated with a mean temperature that might not reflect correctly a specific point inside it. The results show that FDS describes reasonably well the downstream regions ( $X/D > 1.5$  or  $Z/D > 4.8$ ), with lower temperature gradients.

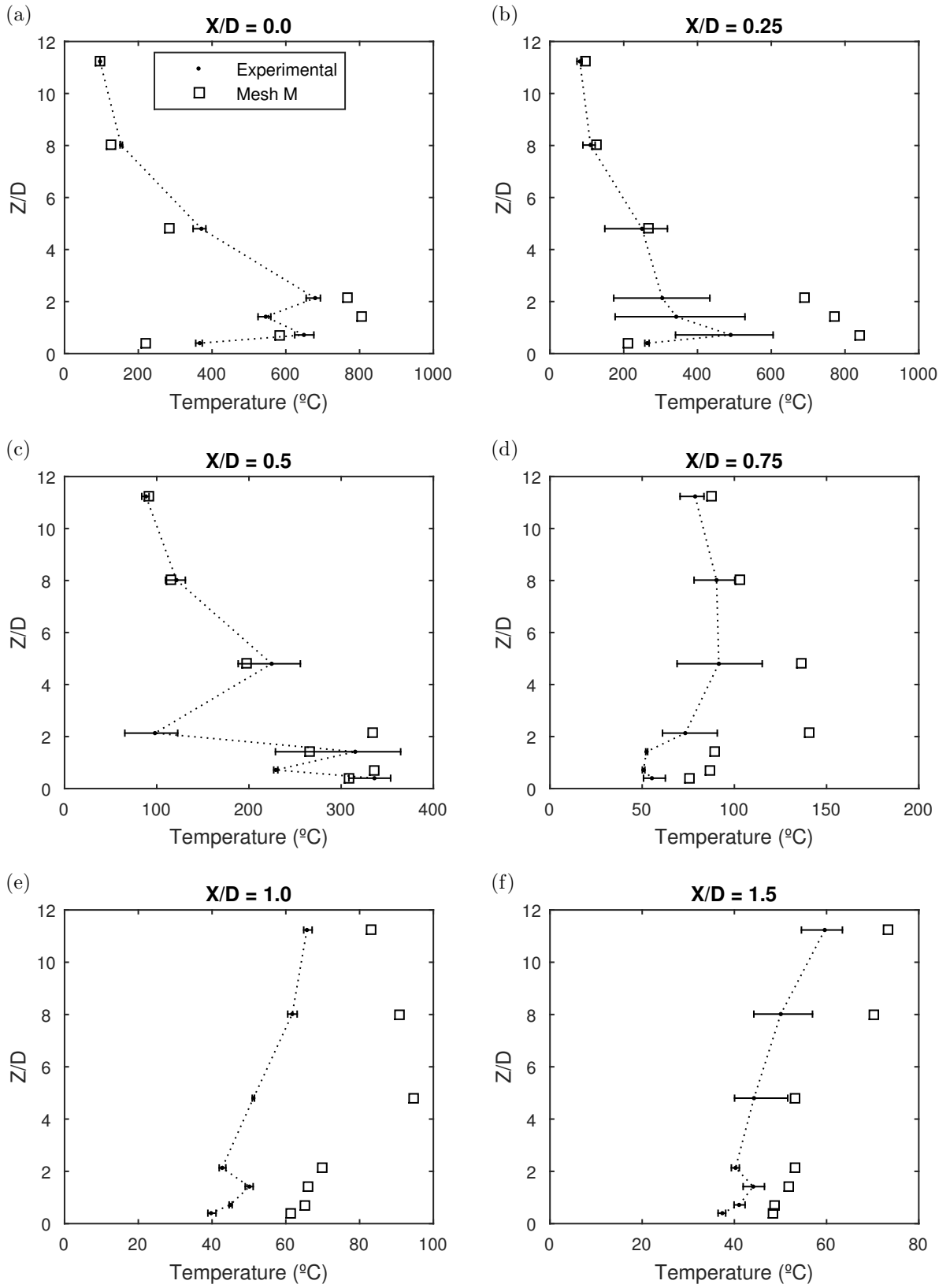


Figure 4.20: Time-averaged temperature profiles (hexane).

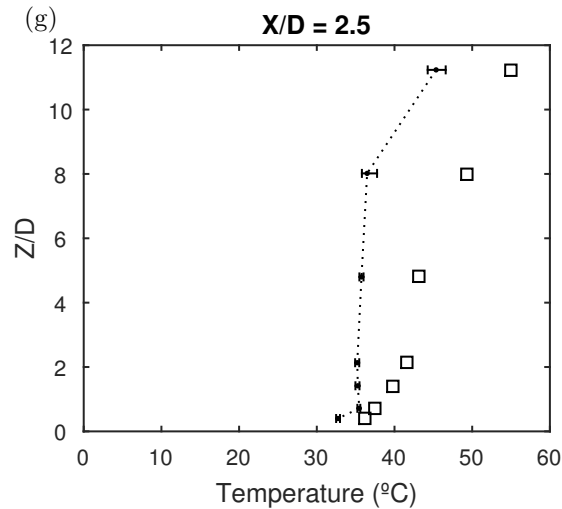


Figure 4.20: Cont. Time-averaged temperature profiles (hexane).

The hydrous ethanol simulation has good agreement with the experimental data (Figure 4.21) except for points in low heights ( $Z/D \leq 2.1$ ) in the planes  $X/D=0.0$  and  $X/D = 0.25$  and for all the point below  $Z/D = 4.8$  in the plane  $X/D=0.5$ , at the pool boundary, for which temperatures are highly overpredicted. Once again, the region associated with the highest errors is within the flame envelope, where the instability is more pronounced.

The simulation for gasoline (Figure 4.22) shows good agreement with the experimental data only for the centerline and the planes  $X/D = 0.25$  and  $X/D = 0.50$  for the highest points ( $Z/D \geq 4.8$ ). Points located at intermediate and further distances from the flame show poor agreement with the experimental data. Gasoline has shown the worst fit with the experimental temperature profile within the tested fuels which might be related with the manner the fuel was modelled in FDS. The description of the fuel using FDS substance library with mass fractions adjusted to match the fuel distillation curve did not yield a proper description of the fuel burning behaviour.

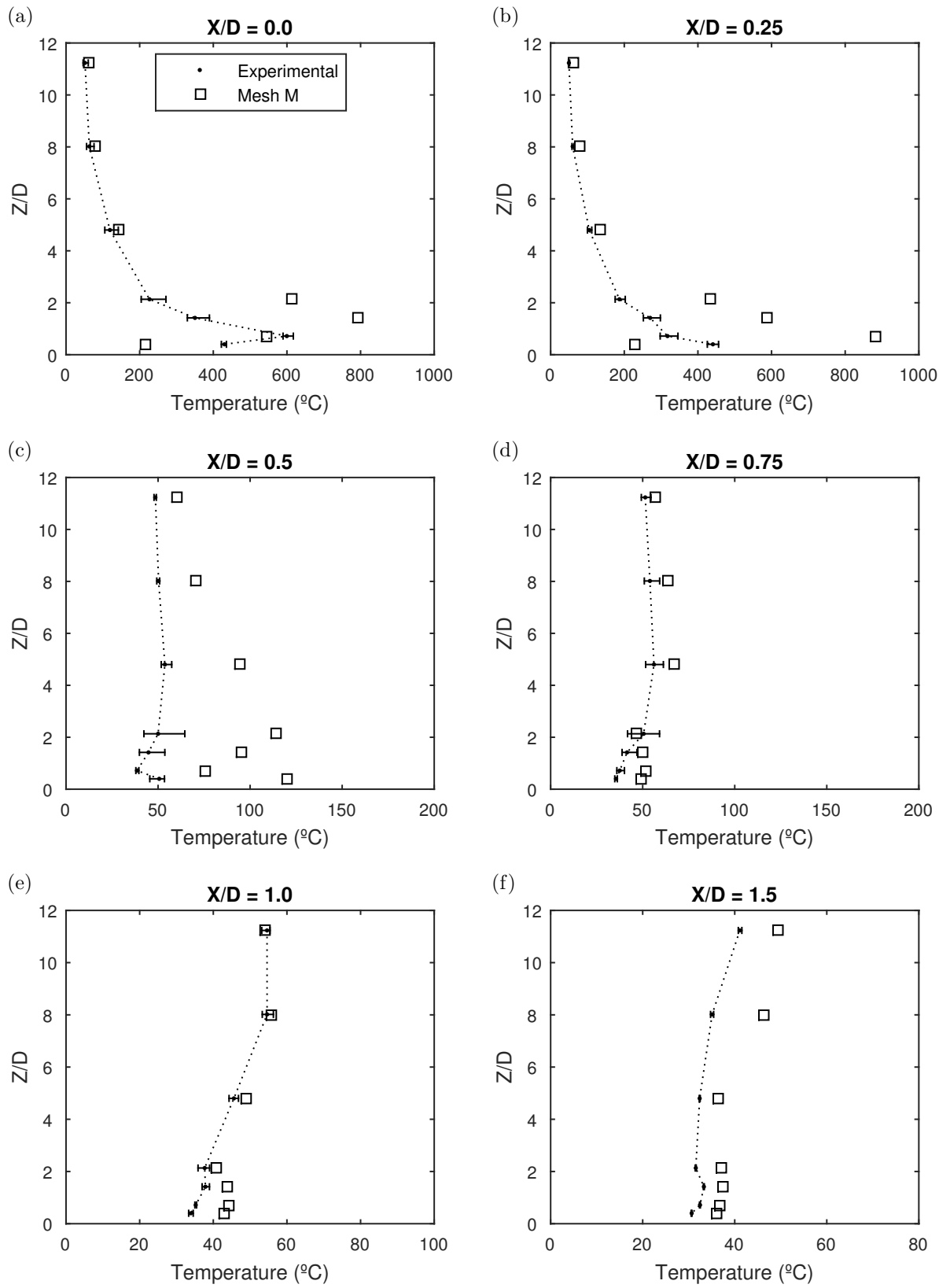


Figure 4.21: Time-averaged temperature profiles (hydrous ethanol).

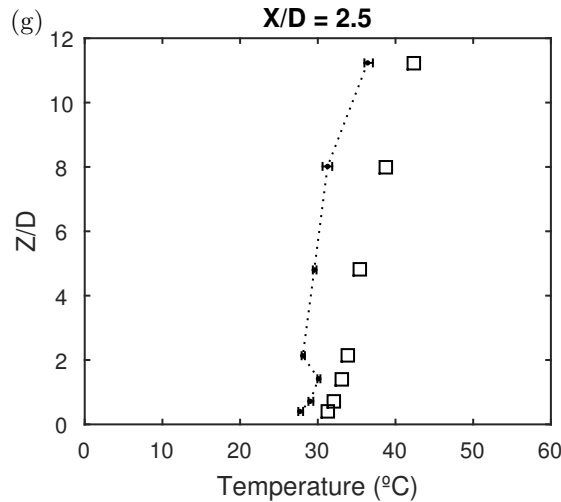


Figure 4.21: Cont. Time-averaged temperature profiles (hydrous ethanol).

Better description of the gasoline pool fire could be obtained by ensuring the heat release rate (HRR) is properly simulated. Two routes could be adopted: experimentally measuring HRR, by the cone calorimeter method, or by using a chemical characterization of a sample of the fuel used in the experiments. Both methods dismiss the usage of FDS substance library. The downside of using this methodology is that extra information from experimental measurements is required, whereas using the software library, which was found to be reasonable for the other fuels, is more straightforward.

The results in figures 4.20-4.22 show that the major difficulty of the FDS simulations to describe the temperature profile around the flame are in the region next to the pool rim, between  $X/D=0.25$  and  $X/D=0.75$ , and with heights below 5.0 diameters. This region comprises the continuous and intermittent zones for the fuel flames. The randomic behaviour of the flame and flame tilting are believed to cause high oscillations on the temperatures in this region which results in large deviations between experimental and simulated temperatures. As a consequence, it is also observed that this region presented high experimental errors.

As a general result FDS has captured the qualitative behaviour of the temperature fields around the pool fires. Quantitative agreement is better in the far field, where temperature gradients are smaller. Temperatures tend to be overpredicted by FDS, which in terms of safety, is better than underpredictions, which only occurred in few points.

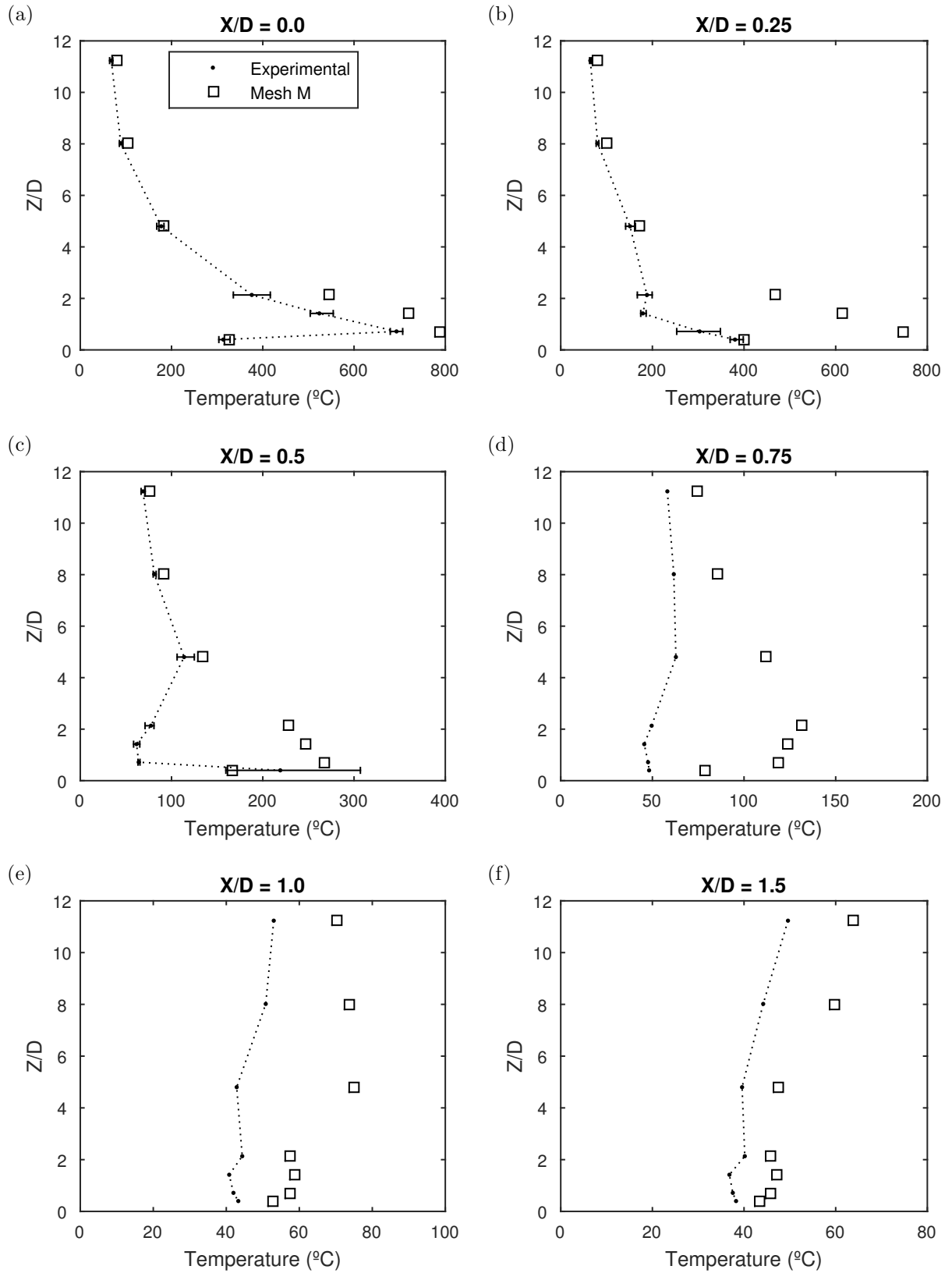


Figure 4.22: Time-averaged temperature profiles (gasoline).

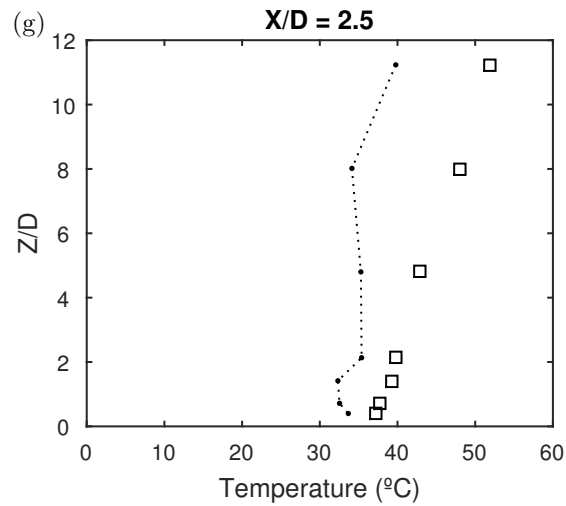


Figure 4.22: Cont. Time-averaged temperature profiles (gasoline).

Figure 4.23 shows the comparison of the time averaged temperature contours in the midplane for the experimental and simulated data. The simulations have a qualitative agreement with the experimental profile and the temperature contours have similar heights and widths. However, the simulated profiles are characterized by high temperatures, which dissipates smoothly with the radius whereas experimental profiles reach lower temperatures and have steep gradients of temperature. Furthermore, Figure 4.23a shows that the simulated profile did not account for the neck observed experimentally in hexane flame on the elevation of  $Z/D=2$ .

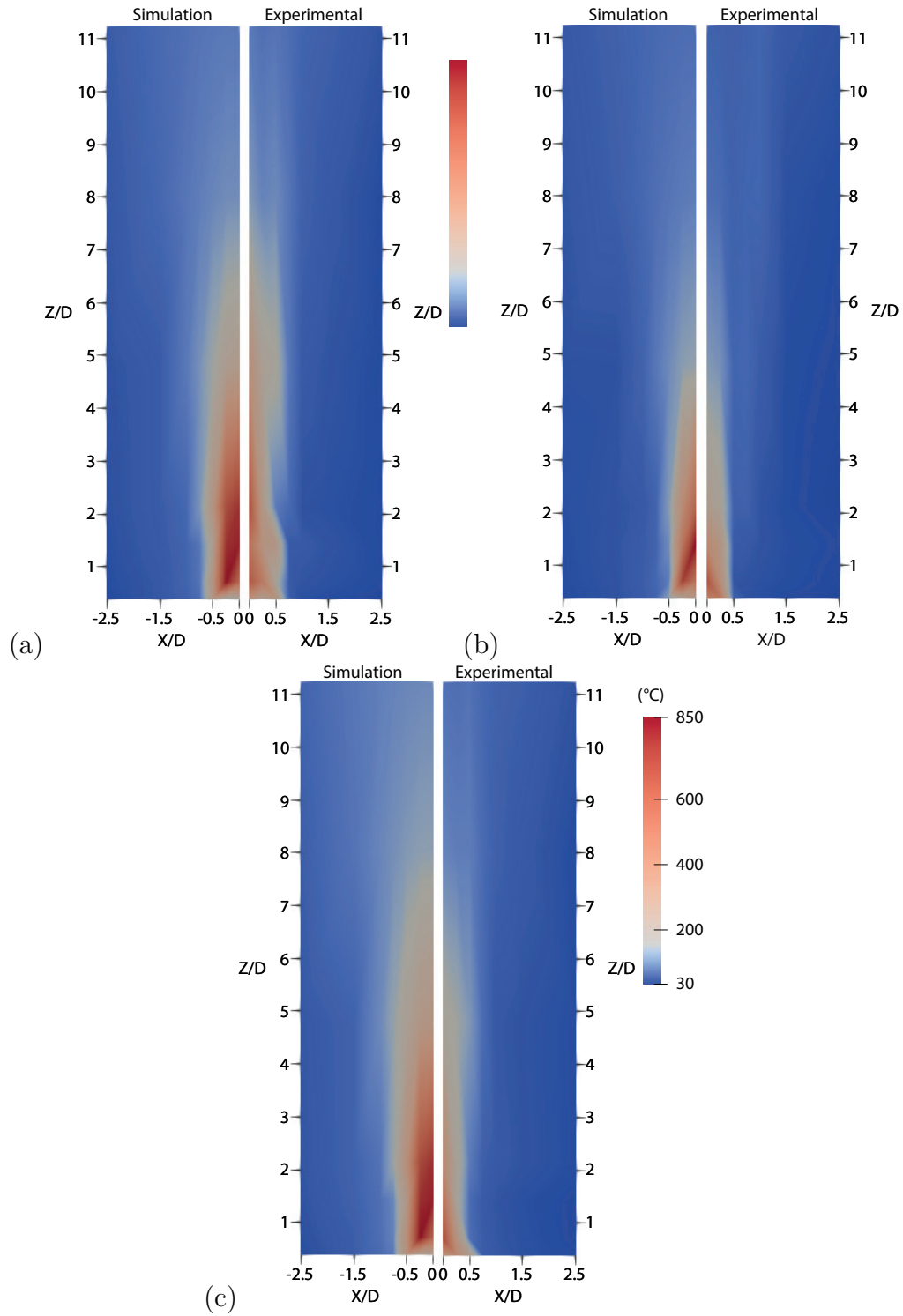


Figure 4.23: Time averaged temperature contours at the middle plane of the domain (left side) and experimental (right side) for (a) commercial hexane, (b) hydrous ethanol and (c) type C gasoline.

## 4.2.2 Influence of CO and soot modelling

The modelling of carbon monoxide and soot formation have a large impact in the energy balance of a fire simulation. CO formation is caused by incomplete combustion which is associated with low oxygenation in the reaction zone and results in the reduction of the heat release rate. HRR is also reduced by the soot production, whereas soot is also known to strongly emit thermal radiation. In FDS model, the soot yield only affects the energy balance by the calculus of HRR.

The influence of the CO and soot modelling were evaluated by comparing simulations where CO and soot yields were annulled with simulations where these values were modelled. The comparison between these simulation conditions for the hexane flame with the Medium (M) mesh is shown in Figure 4.24. The results reveals that the CO and soot yields had very little effect on the temperature profiles. Therefore, improvements in the modeling of these values will not result in significantly better temperature results.

Table 4.6 shows that the computational cost for the zero CO and soot yields simulation was slightly reduced compared to the standard simulation condition. FDS does not change the number of lumped species when CO and soot formation are taken into account in the simulation, however, the number of primitive species in the products is changed which affects the computational cost.

Table 4.5: Computational cost for the simulations with different CO and soot modelling conditions

	Zero CO and soot yields	Adjusted CO and soot yields
Computational Cost (h)	38.4	41.4

The results in this section show that CO and soot modelling have very little effect on the temperature profiles and computational costs. In the next section we investigate the effects of the turbulence models in the simulation results.

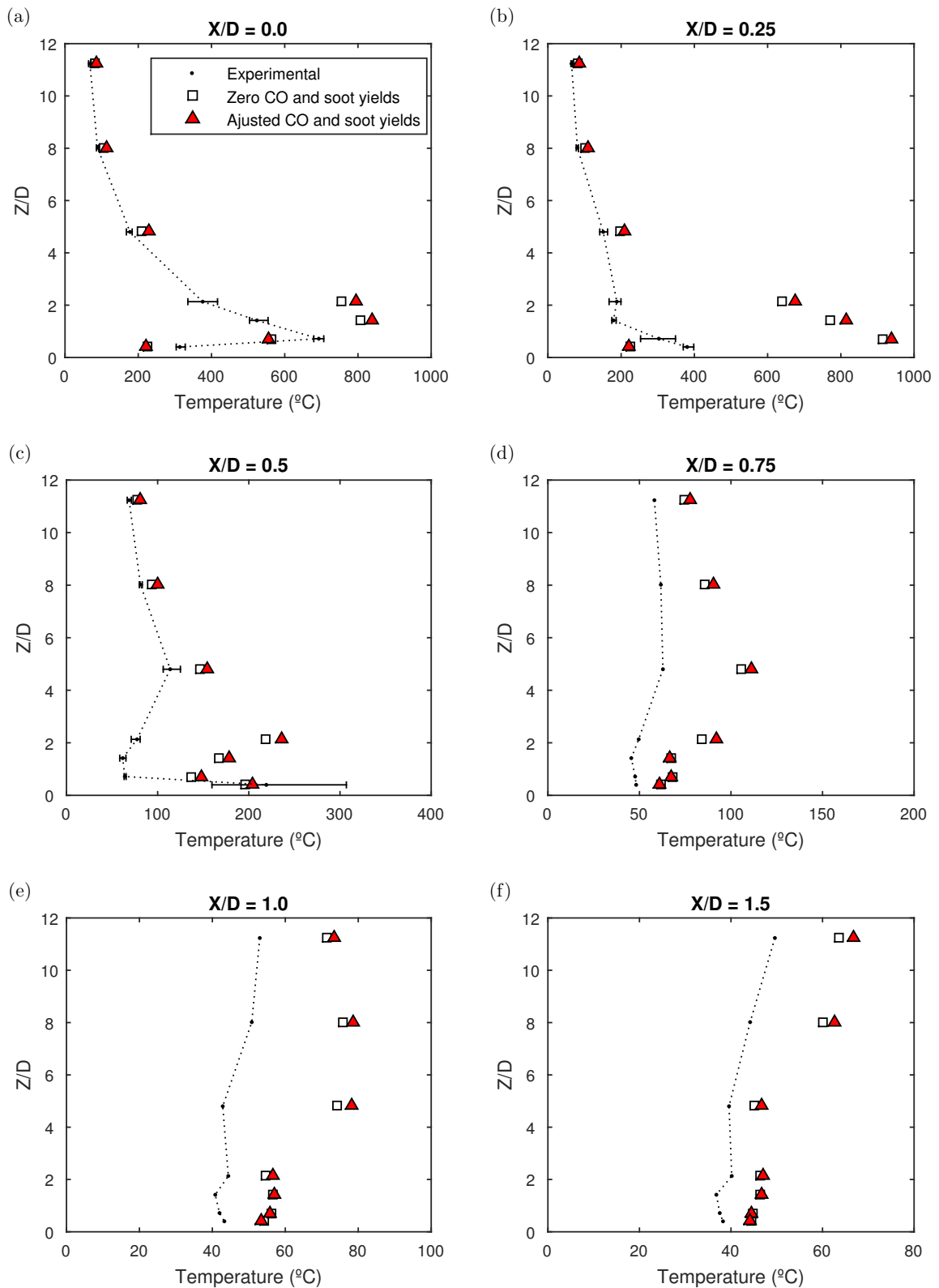


Figure 4.24: Comparison between experimental temperature profiles with the simulated profiles obtained with zero CO and soot yields and with modelled CO and soot yields (hexane).

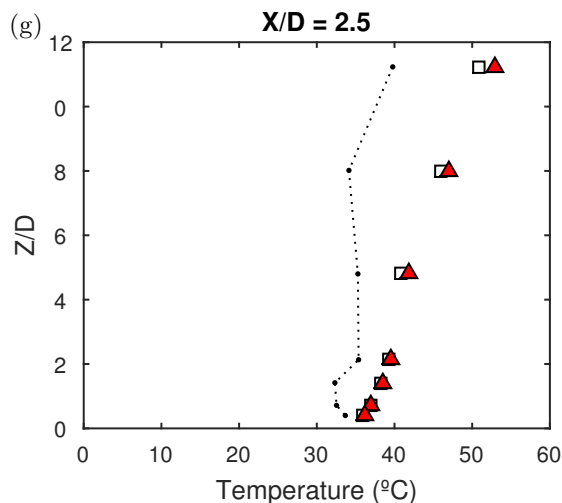


Figure 4.24: cont. Comparison between experimental temperature profiles with the simulated profiles obtained with zero CO and soot yields and with modelled CO and soot yields (hexane).

### 4.2.3 Influence of the turbulence sub-grid model

The usage of Large Eddy Simulation (LES) in CFD modelling requires an appropriate choice of the turbulence sub-grid model, which ensures a proper modeling of the eddy viscosity and its associated dissipative effects. The influence of the turbulence model on the simulated temperature field was evaluated in this study and Figure 4.25 shows the results of simulations with the Deardorff turbulence model (DTM) for the hexane flame with the Coarse (C) mesh compared to the standard Smagorinsky model (SM) and the Dynamic Smagorinsky model (DSM). Bear in mind that both SM and DTB make use of a constant value. FDS default value for these constants are  $C_s = 0.20$  and  $C_v = 0.1$  respectively. Differently, DSM allows the Smagorinsky constant  $C_s$  to vary in time and space. As a result, DSM simulations have predicted a maximum temperature of  $694^{\circ}\text{C}$ , which is much closer to the experimental value ( $679^{\circ}\text{C}$ ) than what was obtained with the other models.

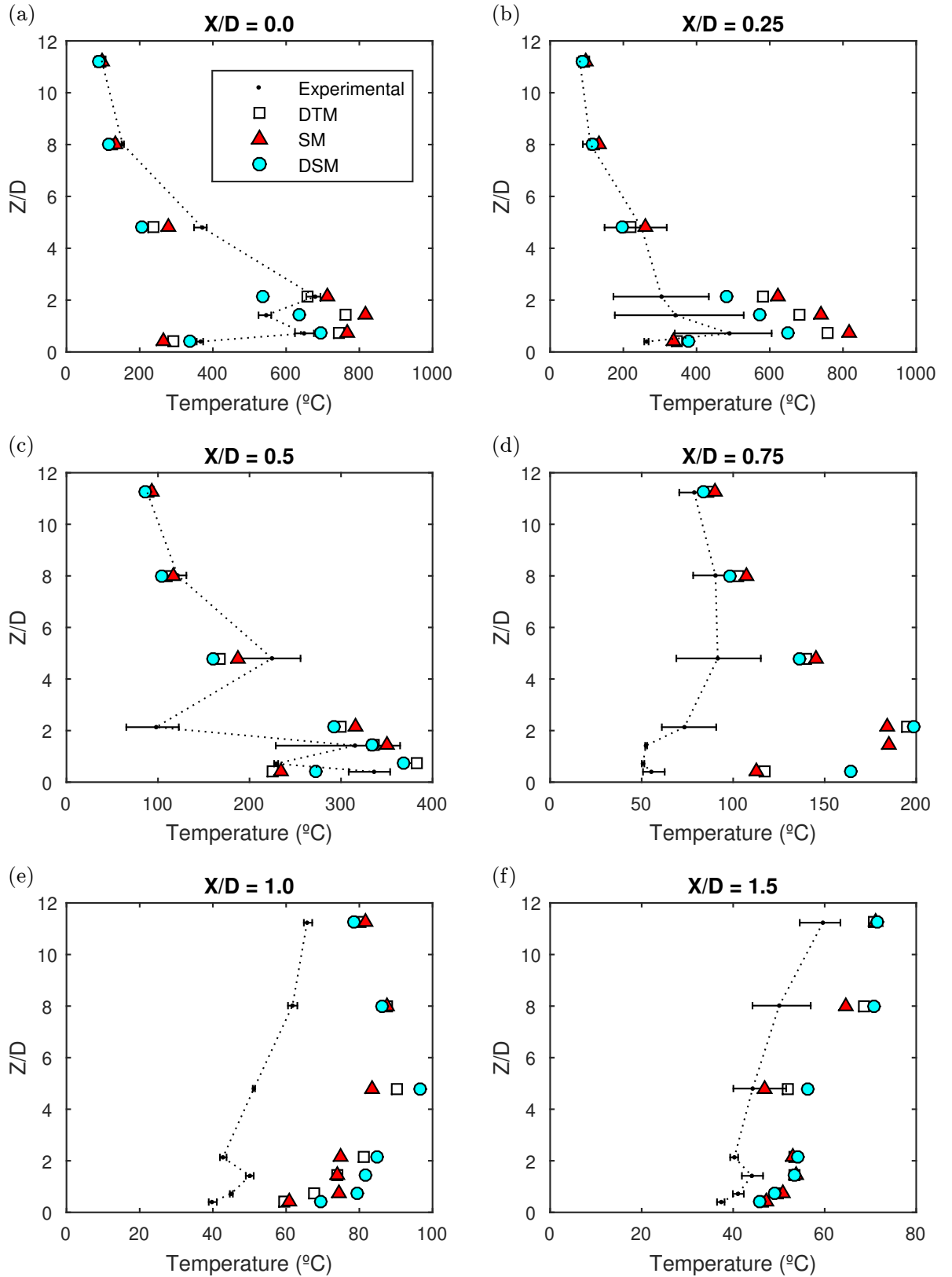


Figure 4.25: Simulated temperature profiles with three turbulence models: Deardorff (DTM), Smagorinsky (SM) and Dynamic Smagorinsky (DSM).

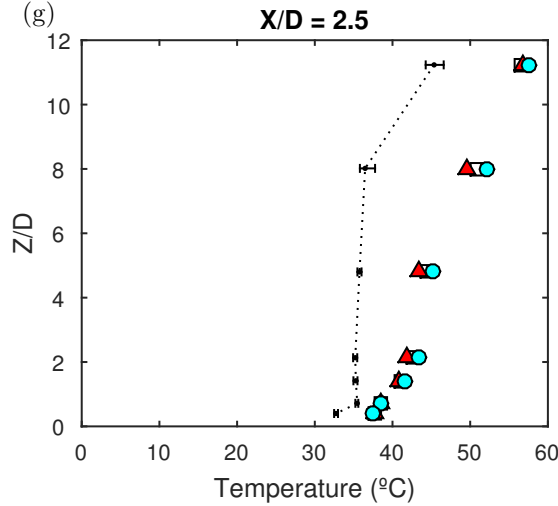


Figure 4.25: cont. Simulated temperature profiles with three turbulence models: Deardorff (DTM), Smagorinsky (SM) and Dynamic Smagorinsky (DSM).

Figure 4.25 shows that DSM improved the temperature profile in the  $X/D = 0.25$  profile. On the other profiles, however, no clear improvement was observed by the change of the turbulence models. The computational cost was similar for all the tested models, see Table 4.6.

Table 4.6: Computational cost for the simulations with different turbulence models

	DTM	SM	DSM
Computational Cost (h)	43.0	44.6	48.0

#### 4.2.4 Analysis of the Liquid Pyrolysis Model

As mentioned before, FDS has an evaporation prediction model, named Liquid Pyrolysis Model (LPM), which simulates the mass loss rate based on the fuel properties. In this section, LPM was used to perform a comparative analysis of simulated and experimental MLRPUA.

Figures 4.26 and 4.27 show the results for the three mesh grids (C, M and F). Figure 4.26 shows that the fuel was consumed approximately three times faster when MLRPUA was predicted by FDS and little improvement was obtained with the refinement of the mesh grid. The burn out was achieved in 60 s for the fine (F) mesh simulation against 157 s obtained experimentally. The quasi-steady period was associated with the

period between 10 and 43 s (Figure 4.27) and the average mass loss rate per unit area for the fine (F) mesh in this period was  $0.0620 \text{ kg/m}^2\text{s}$ , which is 337% higher than the experimental value. As discussed in Section 4.2.1, even when the burning rates is set by the user, FDS overpredicts temperatures, specially in the region next to the burner, this might lead LPM, when activated, to calculate higher heat transfer to the liquid pool causing overpredicted evaporation and burning rates.

It is worthy noting that FDS Validation guide (McGrattan et al., 2015a) shows good agreement between the predicted burning rate for a variety of liquid fuels, including heptane and ethanol, confined within a 10 cm deep, 1 m square tray compared to experimental values and empirical correlations. The high burning rates obtained with the predicted MLRPUA model seen in Figure 4.27, however indicate that the Liquid Pyrolysis Model is unable to account for the physics of small pool fires such as the experiment used in this work.

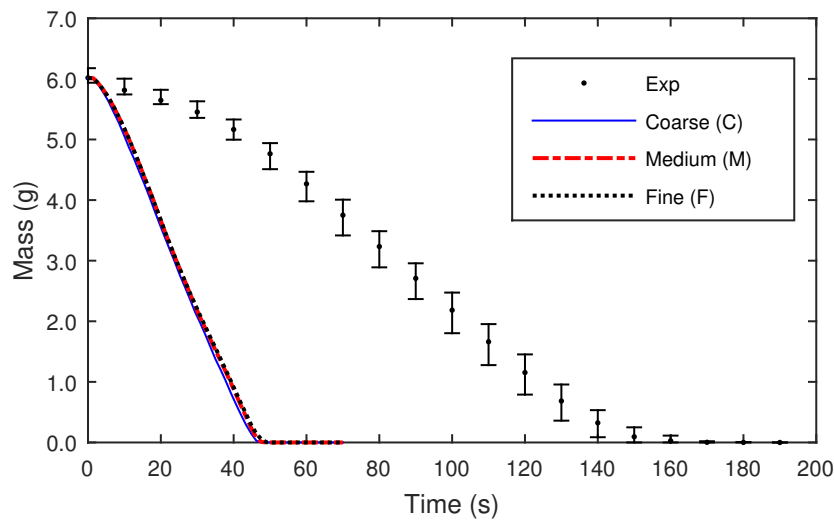


Figure 4.26: Comparison of mass loss curves (hexane).

Table 4.7: GTE, Flame height and Computational cost

Mesh	Processors	Global Temperature Error – GTE (%)	Dimensionless Flame Height	Total CPU time (h)
Coarse (C)	4	148.5	5.41	26.1
Medium (M)	4	165.6	5.66	172.5
Fine (F)	4	185.6	5.66	388.5
Experimental	-	-	4.17	-
Heskestad	-	-	4.35	-

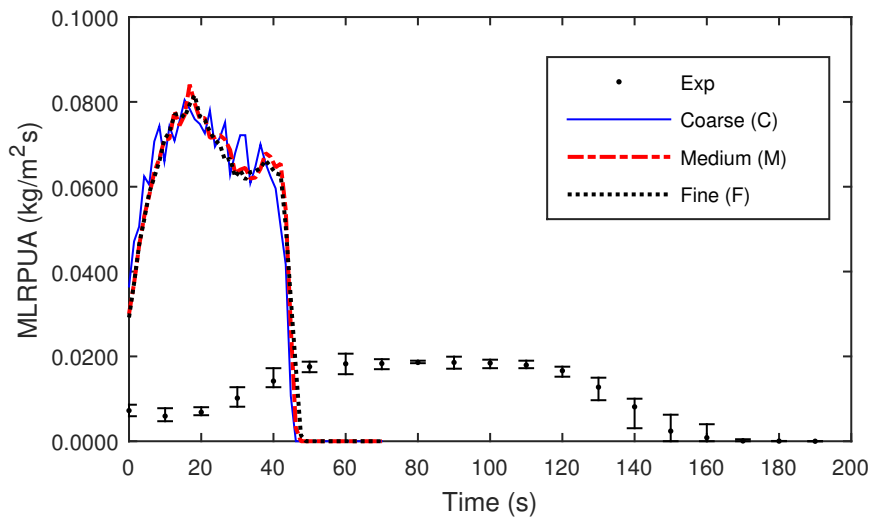


Figure 4.27: Mass loss rate per unit area (hexane).

As a result of the high burning rates obtained by the LPM simulation, Table 4.7 shows that the GTE were over 148.5% for all the grid resolutions simulated and that little improvement was obtained with mesh refinement. The simulated flame height with the fine (F) mesh was overpredicted in 36% compared to the experimental data.

Figure 4.28 shows the comparison between the temperature profiles of prescribed and calculated MRLPUA simulations both with the Coarse (C) mesh. The temperature profiles calculated by LPM have a poor agreement with the experimental data, the temperature values are highly overpredicted and errors are much higher compared to the simulation where a Prescribed Burning Rate (PBR) approach is used. PBR is the methodology used in the previous sections, where the burning rate was fixed by the user and not calculated by FDS.

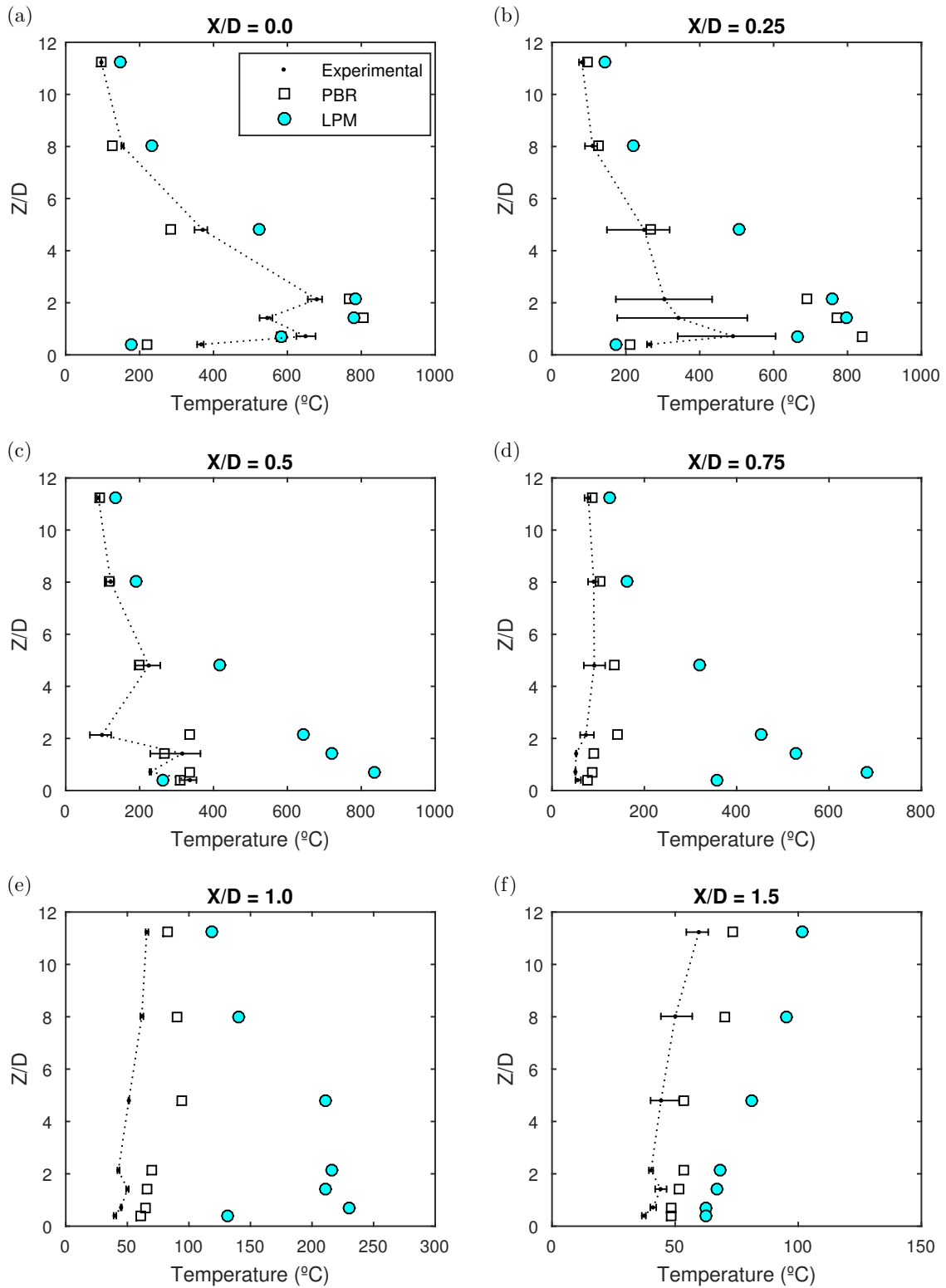


Figure 4.28: Comparison between experimental temperature profiles with simulated profiles obtained with the prescribed burning rate model (PBR) and with the liquid pyrolysis model (LPM).

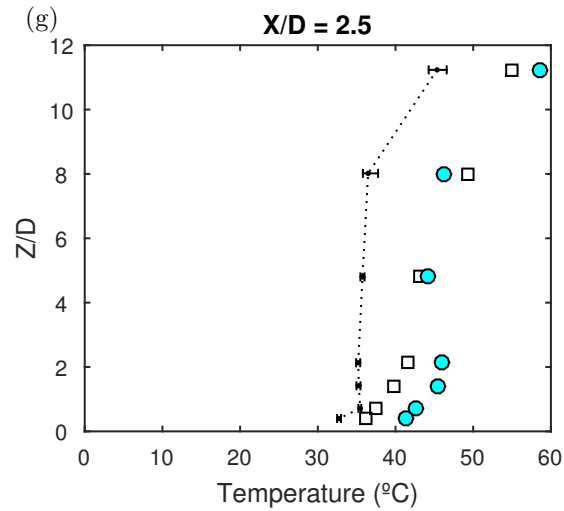


Figure 4.28: cont. Comparison between experimental temperature profiles with simulated profiles obtained with the prescribed burning rate model (PBR) and with the liquid pyrolysis model (LPM).

The results in this section showed that LPM solver was unable to predict the burning rate in the tested configuration. The LPM simulations yielded overpredicted temperatures and flame heights even for the finer grid resolutions.

## Chapter 5

# Conclusions

This work has been performed in order to evaluate how FDS simulations correlates with experimental pool fire temperature field and flame heights. Small scale pool fires of commercial hexane, hydrous ethanol and type C gasoline were reproduced experimentally and FDS simulations were compared with the experimental data. The major findings of this work are presented in this section.

The tested fuels presented burning behaviors divided in three stages: growth, stable burning and decay. It was not distinguished a bulk boiling burning stage due to the extremely thin layer of the pools.

The simulations have good agreement with the experimental data when MLR-PUA is prescribed by the user, and even when quantitative agreement with experimental data is not good, the trends are well reproduced in the simulations. FDS predicts flame heights with errors below 16% compared to the experimental results.

The qualitative behaviour of the temperatures field is well captured by the simulator, but overpredictions occur in a given number of probes. Quantitative agreement is better in the downstream regions, where temperature gradients are smaller. Therefore, FDS describes better the plume region rather than the temperatures within the flame envelope.

High measurement errors are observed in the region next to the burner exit

( $X/D < 0.5$  and  $Z/D < 4.8$ ) which are associated with the high oscillations and large temperature gradients. The major discrepancies between simulation and experimental data occur in this area, however, it is unclear whether this is a consequence of the high experimental errors or a software failure to characterize this region.

The description of gasoline using FDS substance library with the concentrations of the components adjusted to match the fuel distillation curve does not yield a proper description of the fuel burning behaviour. As a result, gasoline temperature profile has poor agreement with the experimental data.

The influence of CO and soot parameters used in FDS simulations on the temperature field was found to be very little. Whether the tests with different turbulence models revealed that the Dynamic Smagorinsky model improves the prediction of the temperature profile in  $X/D = 0$  and  $0.25$  profiles compared to the Constant Coefficient Smagorinsky model and the Deardorff model with small impact on the computational cost.

When predicted by FDS, the evaporation rate is highly overpredicted suggesting that the Liquid Pyrolysis Model is unable to account for the small-scale pool fire physics. The high burning rates obtained in these simulations causes the overprediction of the flame heights and the temperature profile have large errors compared to the experimental data.

Further research can be developed to complement the results obtained in this work. The author suggestions are described below:

- Further investigation of the temperature profile next to the burner exit is needed in order to identify whether the high errors in this area are caused by the measurement errors due to the unstable behaviour of the flame or by a failure of the software to characterize this region.
- Evaluation of how FDS describes the velocity field around the pool fire compared with experimental measurements and investigation of how the software predicts the

convection and buoyancy phenomena.

- Evaluation of how FDS simulations correlate with a medium and a large scale pool fires with the same fuels. Investigate how the scale of the pool fire affects the simulation results.
- Comparative study of gasoline simulations with different characterization methods: by the fuel distillation curve and by chemical analysis of a sample of the fuel.
- Study of the time-dependent behaviour of the FDS simulations during the burning stages of growth and decay.
- Evaluation of how FDS predicts scenarios of confined compartment pool fires, such as tunnel or indoors fires.

# Bibliography

- Abbott, M. B., & Basco, D. R. (1989). Computational fluid dynamics-an introduction for engineers. *NASA STI/Recon Technical Report A, 90*.
- Ahrens, J., Geveci, B., Law, C., Hansen, C., & Johnson, C. (2005). Paraview: An end-user tool for large-data visualization. *The visualization handbook, 717*.
- Babrauskas, V. (1983). Estimating large pool fire burning rates. *Fire technology, 19*(4), 251–261.
- Barr, J. (1953). Diffusion flames. In *Symposium (international) on combustion* (Vol. 4, pp. 765–771).
- Baum, H. R., & McGrattan, K. B. (1999). Simulation of oil tank fires. *National Institute of Standards and Technology, Gaithersburg, Maryland, USA*.
- Brzezinska, D., & Markowski, A. S. (2017). Experimental investigation and cfd modelling of the internal car park environment in case of accidental lpg release. *Process Safety and Environmental Protection, 110*, 5–14.
- Chang, J. I., & Lin, C.-C. (2006). A study of storage tank accidents. *Journal of loss prevention in the process industries, 19*(1), 51–59.
- Chen, B., Lu, S., Li, C., Kang, Q., & Yuan, M. (2012). Unsteady burning of thin-layer pool fires. *Journal of fire sciences, 30*(1), 3–15.
- Chen, Z., Wen, J., Xu, B., & Dembele, S. (2014a). Extension of the eddy dissipation concept and smoke point soot model to the les frame for fire simulations. *Fire Safety Journal, 64*, 12–26.

- Chen, Z., Wen, J., Xu, B., & Dembele, S. (2014b). Large eddy simulation of a medium-scale methanol pool fire using the extended eddy dissipation concept. *International Journal of Heat and Mass Transfer*, *70*, 389–408.
- Chen, Z., Wu, X. N., Song, W. H., Lv, L. Y., & Wang, X. D. (2014). Applicability analysis of mathematical models for the combustion characteristics in the pool fire. *Combustion, Explosion, and Shock Waves*, *50*(3), 290–299.
- Cook, A. W., & Riley, J. J. (1998). Subgrid-scale modeling for turbulent reacting flows. *Combustion and Flame*, *112*(4), 593–606.
- Cox, G., & Chitty, R. (1980). A study of the deterministic properties of unbounded fire plumes. *Combustion and Flame*, *39*(2), 191–209.
- Drysdale, D. (2011). *An introduction to fire dynamics*. John Wiley & Sons.
- Fortuna, A. d. O. (2000). *Técnicas computacionais para dinâmica dos fluidos: conceitos básicos e aplicações*. Edusp.
- Germano, M., Piomelli, U., Moin, P., & Cabot, W. H. (1991). A dynamic subgrid-scale eddy viscosity model. *Physics of Fluids A: Fluid Dynamics*, *3*(7), 1760–1765.
- Gottuk, D. T., & Lattimer, B. Y. (2016). Effect of combustion conditions on species production. In *Sfpe handbook of fire protection engineering* (pp. 486–528). Springer.
- Hamins, A. P., Yang, J. C., & Kashiwagi, T. (1999). *Global model for predicting the burning rates of liquid pool fires (nistir 6381)* (Tech. Rep.).
- Hayasaka, H. (1997). Unsteady burning rates of small pool fires. *Fire Safety Science*, *5*, 499–510.
- Heskestad, G. (1983). Luminous heights of turbulent diffusion flames. *Fire safety journal*, *5*(2), 103–108.
- Heskestad, G. (1984). Engineering relations for fire plumes. *Fire Safety Journal*, *7*(1), 25–32.
- Hietaniemi, J., Vaari, J., & Hostikka, S. (2004). *Fds simulation of fire spread: Comparison of model results with experimental data*. VTT.

- Hostikka, S., McGrattan, K. B., & Hamins, A. (2003). Numerical modeling of pool fires using les and finite volume method for radiation. *Fire Safety Science*, 7, 383–394.
- Hu, L. (2017). A review of physics and correlations of pool fire behaviour in wind and future challenges. *Fire Safety Journal*, 91, 41–55.
- Hurley, M. J., Gottuk, D. T., Hall Jr, J. R., Harada, K., Kuligowski, E. D., Puchovsky, M., ... others (2015). *Sfpe handbook of fire protection engineering*. Springer.
- Jiang, C., Li, Y., Huang, H., Zhao, J., Wang, Z., & Zhang, J. (2016). Experimental study of burning rate in large-scale rectangular pool fire. *Journal of Fire Sciences*, 34(4), 323–334.
- Joulain, P. (1998). The behavior of pool fires: state of the art and new insights. In *Symposium (international) on combustion* (Vol. 27, pp. 2691–2706).
- Kang, Y., Wen, J., McGrattan, K., & Baum, H. (2001). The use of a laminar flamelet approach in the large eddy simulation of flame structure at the base of a pool fire.
- Kang, Y., & Wen, J. (2004). Large eddy simulation of a small pool fire. *Combustion science and technology*, 176(12), 2193–2223.
- Li, Y. Z., & Ingason, H. (2018). Overview of research on fire safety in underground road and railway tunnels. *Tunnelling and Underground Space Technology*, 81, 568–589.
- Loy, Y., Rangaiah, G., & Lakshminarayanan, S. (2018). Surrogate modelling of net radiation flux from pool fires in a hydrocarbon storage facility. *Process Safety and Environmental Protection*, 114, 296–309.
- Ma, T., & Quintiere, J. (2003). Numerical simulation of axi-symmetric fire plumes: accuracy and limitations. *Fire Safety Journal*, 38(5), 467–492.
- McCaffrey, B. (1983). Momentum implications for buoyant diffusion flames. *Combustion and Flame*, 52, 149–167.
- McDermott, R. J. (2009). *Fds wall flows part i: Straight channels*. US Department of Commerce, National Institute of Standards and Technology.

- McGrattan, K., Hostikka, S., Floyd, J., Baum, H., Rehm, R., Mell, W., & McDermott, R. (2015a). Fire dynamics simulator (version 6), technical reference guide. *NIST special publication*(6).
- McGrattan, K., Hostikka, S., Floyd, J., Baum, H., Rehm, R., Mell, W., & McDermott, R. (2015b). Fire dynamics simulator (version 6), technical reference guide. *NIST special publication*(6).
- McGrattan, K., Hostikka, S., McDermott, R., Floyd, J., Weinschenk, C., & Overholt, K. (2016). Fire dynamics simulator, user's guide. *NIST special publication*, 20.
- Novozhilov, V. (2001). Computational fluid dynamics modeling of compartment fires. *Progress in Energy and Combustion science*, 27(6), 611–666.
- Patankar, S. V. (1980). *Numerical heat transfer and fluid flow, series in computational methods in mechanics and thermal sciences, minkowycz and sparrow eds.* Mc Graw Hill.
- Quintiere, J. (1984). A perspective on compartment fire growth. *Combustion Science and Technology*, 39(1-6), 11–54.
- Rehm, R. G., & Baum, H. R. (1978). The equations of motion for thermally driven, buoyant flows. *Journal of Research of the NBS*, 83(297-308), 2.
- Sahu, D., Kumar, S., Jain, S., & Gupta, A. (2016). Experimental and numerical simulation studies on diesel pool fire. *Fire and Materials*, 40(8), 1016–1035.
- Skarsbø, L. R. (2011). *An experimental study of pool fires and validation of different cfd fire models* (Unpublished master's thesis). The University of Bergen.
- Smagorinsky, J. (1963). General circulation experiments with the primitive equations: I. the basic experiment. *Monthly weather review*, 91(3), 99–164.
- Venkatesh, S., Ito, A., Saito, K., & Wichman, I. S. (1996). Flame base structure of small-scale pool fires. In *Symposium (international) on combustion* (Vol. 26, pp. 1437–1443).
- Versteeg, H., & Malalasekera, W. (1995). Computational fluid dynamics. *The finite volume method*.

- Wahlqvist, J., & van Hees, P. (2016). Implementation and validation of an environmental feedback pool fire model based on oxygen depletion and radiative feedback in fds. *Fire Safety Journal*, *85*, 35–49.
- Wang, C., Guo, J., Ding, Y., Wen, J., & Lu, S. (2015). Burning rate of merged pool fire on the hollow square tray. *Journal of hazardous materials*, *290*, 78–86.
- Weckman, E., & Strong, A. (1996). Experimental investigation of the turbulence structure of medium-scale methanol pool fires. *Combustion and Flame*, *105*(3), 245–266.
- Wen, J., Kang, K., Donchev, T., & Karwatzki, J. (2007). Validation of fds for the prediction of medium-scale pool fires. *Fire Safety Journal*, *42*(2), 127–138.
- Wendt, J. F. (2008). *Computational fluid dynamics: an introduction*. Springer Science & Business Media.
- Xin, Y., Filatyev, S., Biswas, K., Gore, J., Rehm, R., & Baum, H. (2008). Fire dynamics simulations of a one-meter diameter methane fire. *Combustion and Flame*, *153*(4), 499–509.
- Xin, Y., Gore, J. P., McGrattan, K. B., Rehm, R. G., & Baum, H. R. (2005). Fire dynamics simulation of a turbulent buoyant flame using a mixture-fraction-based combustion model. *Combustion and Flame*, *141*(4), 329–335.
- Yuan, L., & Smith, A. C. (2015). Numerical modeling of water spray suppression of conveyor belt fires in a large-scale tunnel. *Process safety and environmental protection*, *95*, 93–101.
- Zukoski, E., Cetegen, B., & Kubota, T. (1985). Visible structure of buoyant diffusion flames. In *Symposium (international) on combustion* (Vol. 20, pp. 361–366).

# Appendix A

## Average temperature curves

The average temperature curves for the hexane, hydrous ethanol and gasoline flames are presented in this annex.

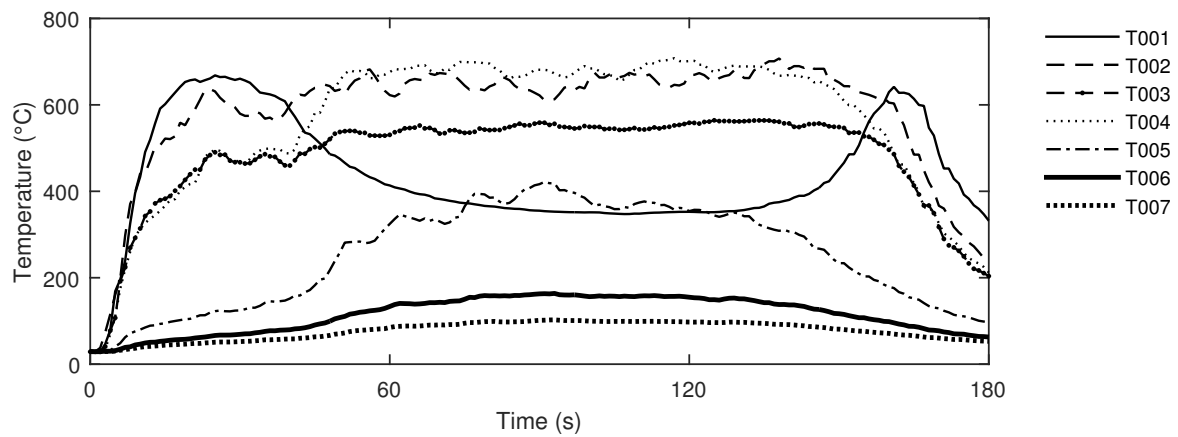


Figure A.1: Average temperature curves for the hexane flame for X/D=0.0

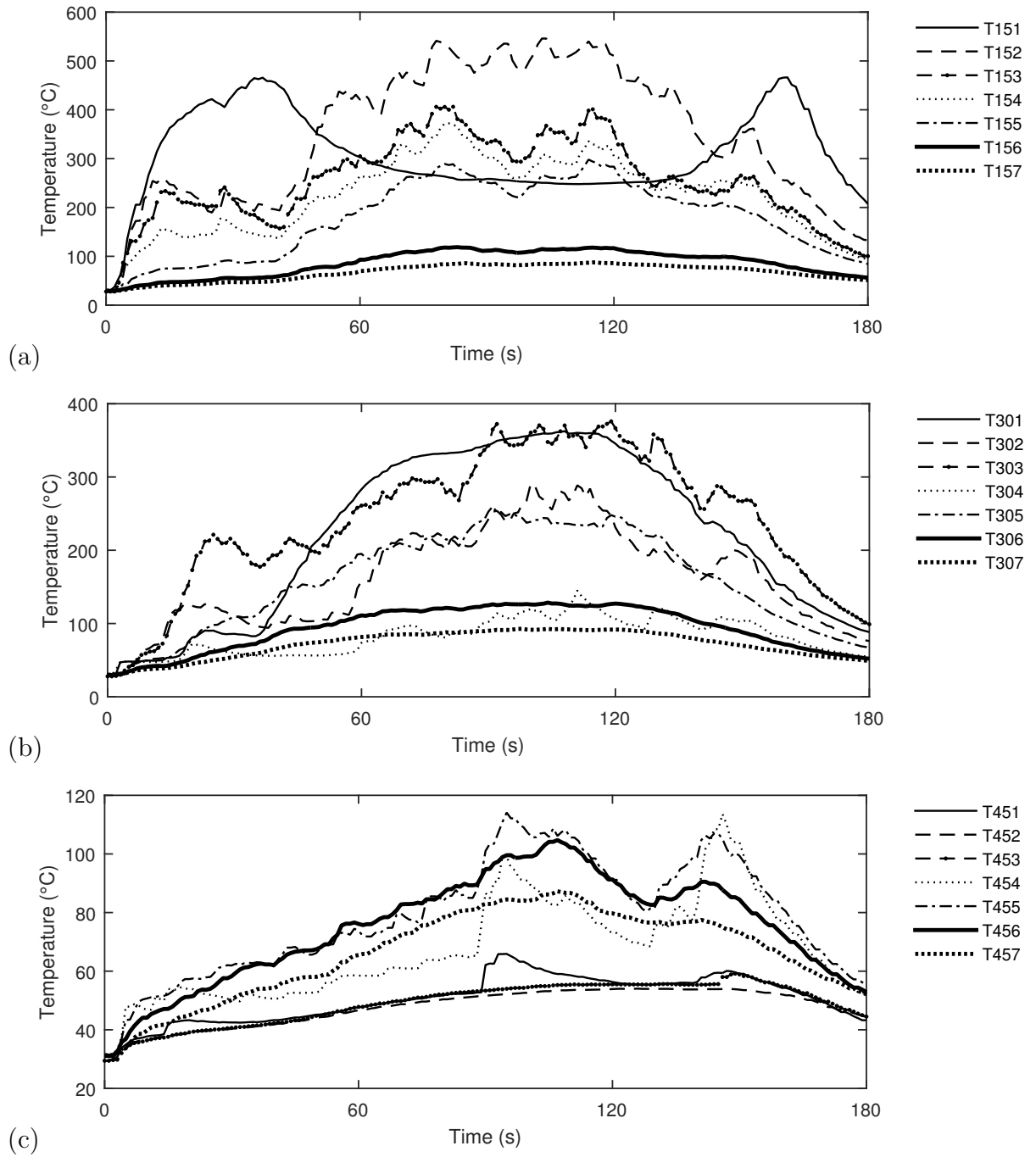


Figure A.2: Average temperature curves for the hexane flame for (a)  $X/D=0.25$ , (b)  $X/D=0.50$  and (c)  $X/D=0.75$ .

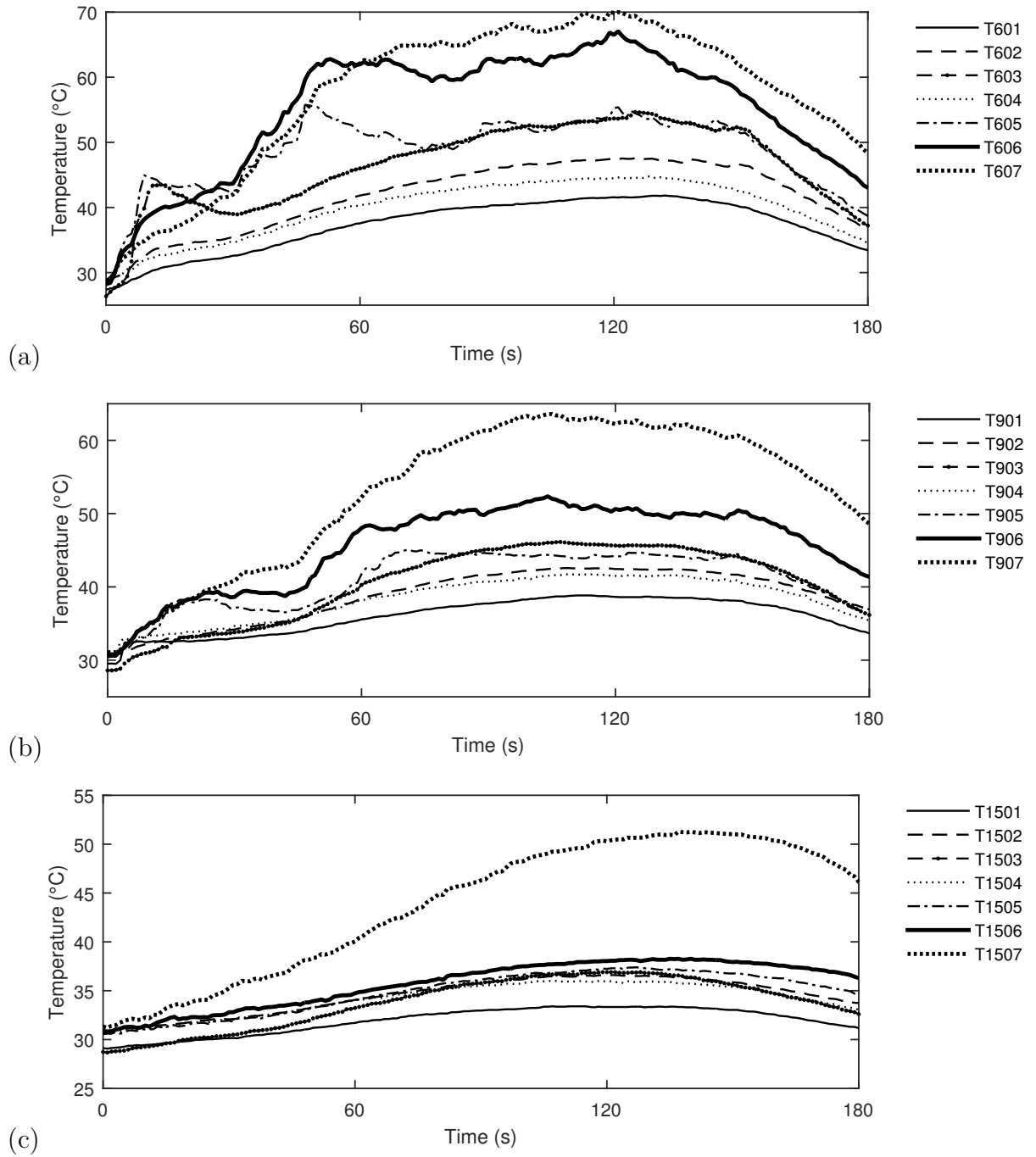


Figure A.3: Average temperature curves for the hexane flame for (d)  $X/D=1.00$ , (e)  $X/D=1.50$  and (f)  $X/D=2.50$ .

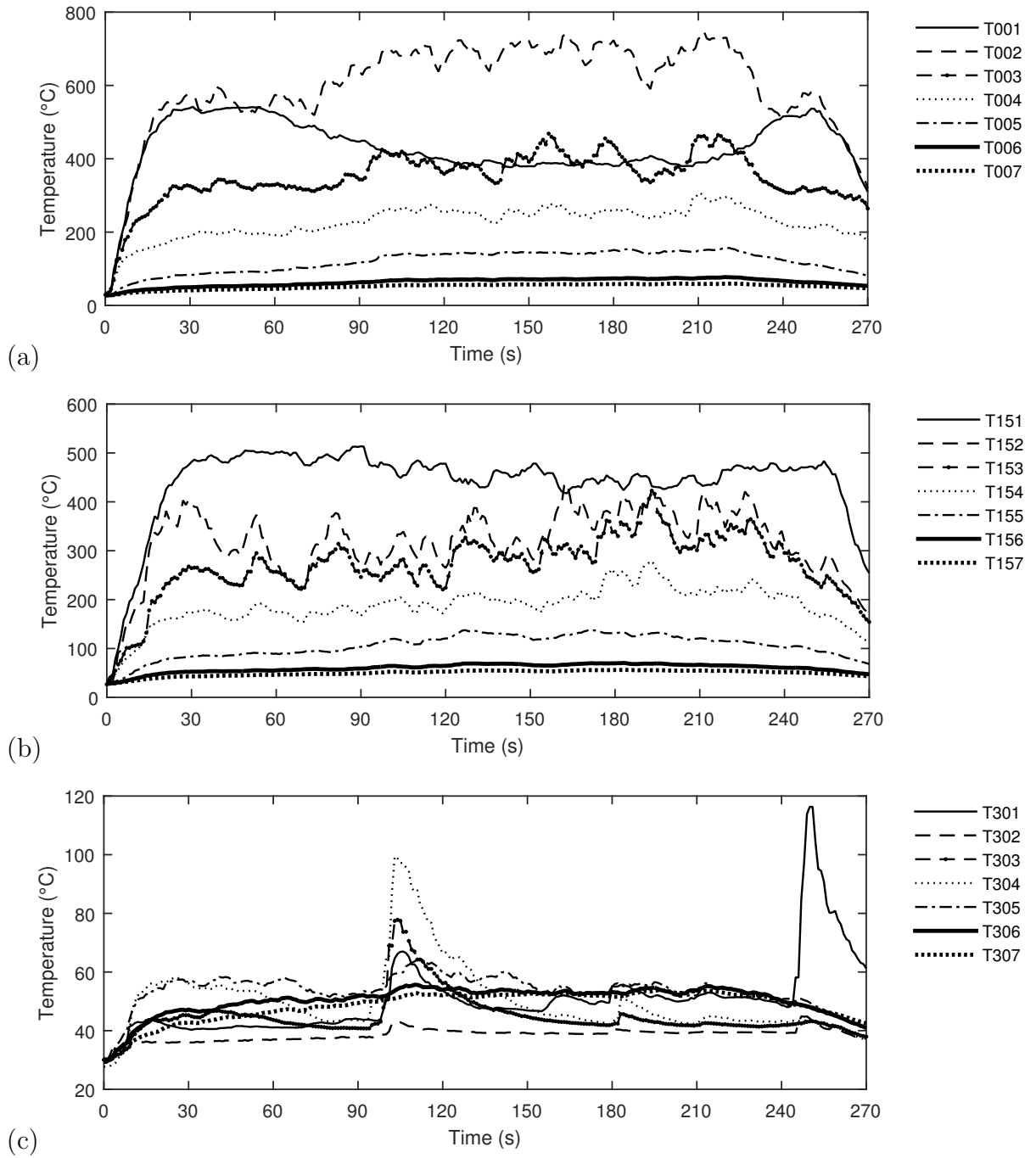


Figure A.4: Average temperature curves for the hydrous ethanol flame for (a)  $X/D=0.0$ , and (b)  $X/D=0.25$ , (b)  $X/D=0.50$ .

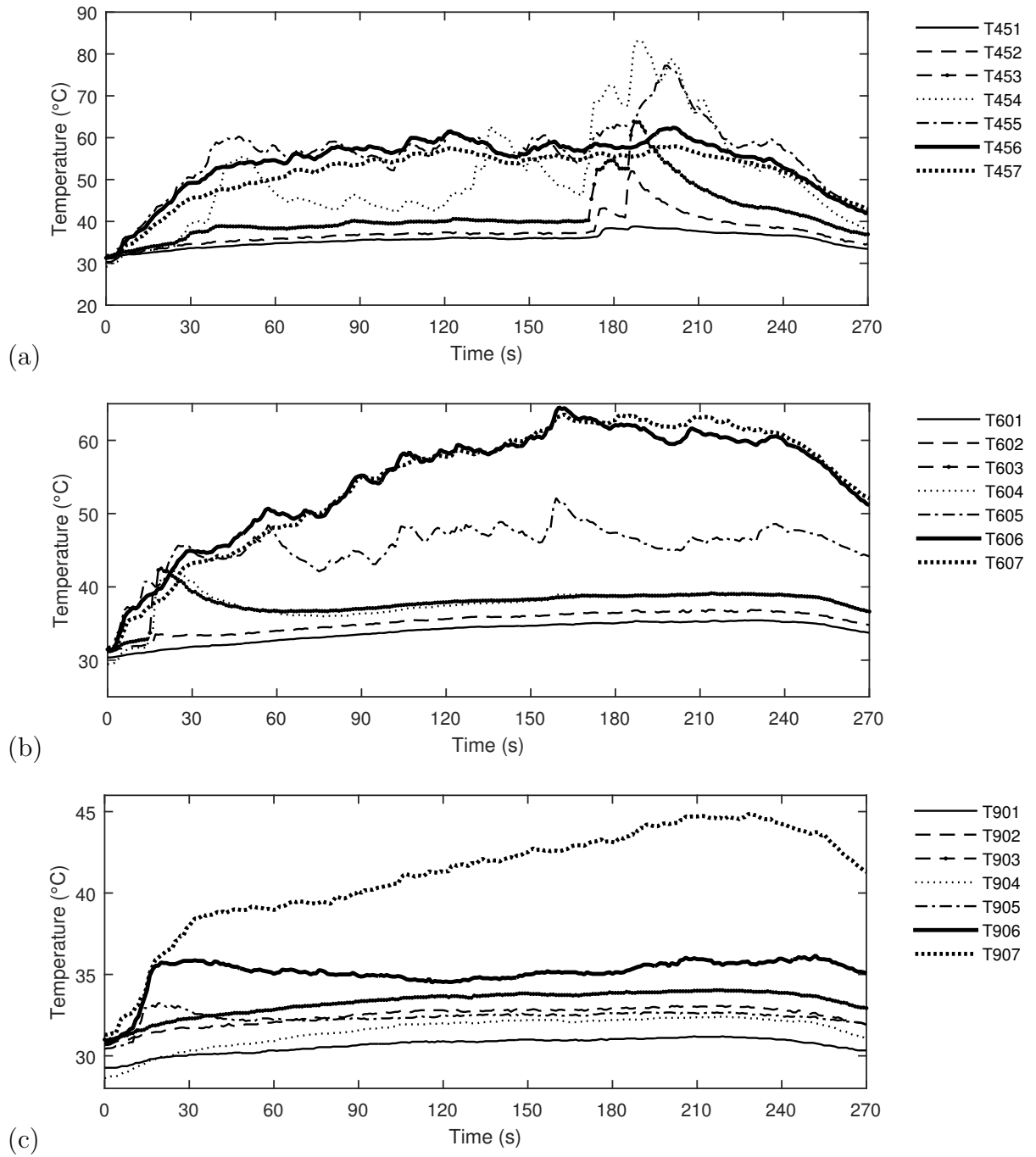


Figure A.5: Average temperature curves for the hydrous ethanol flame for (a)  $X/D=0.75$ , and (b)  $X/D=1.00$ , (c)  $X/D=1.50$ .

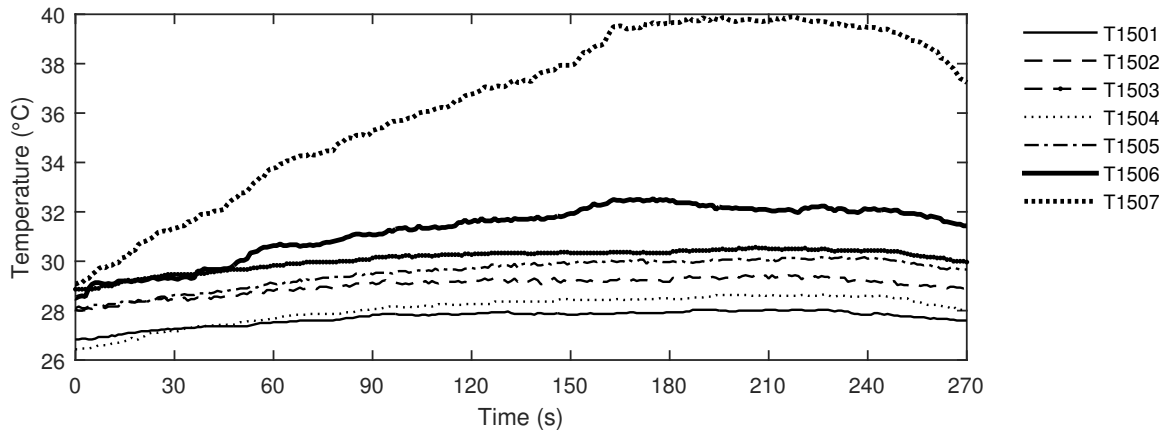


Figure A.6: Average temperature curves for the hydrous ethanol flame for  $X/D=2.50$ .

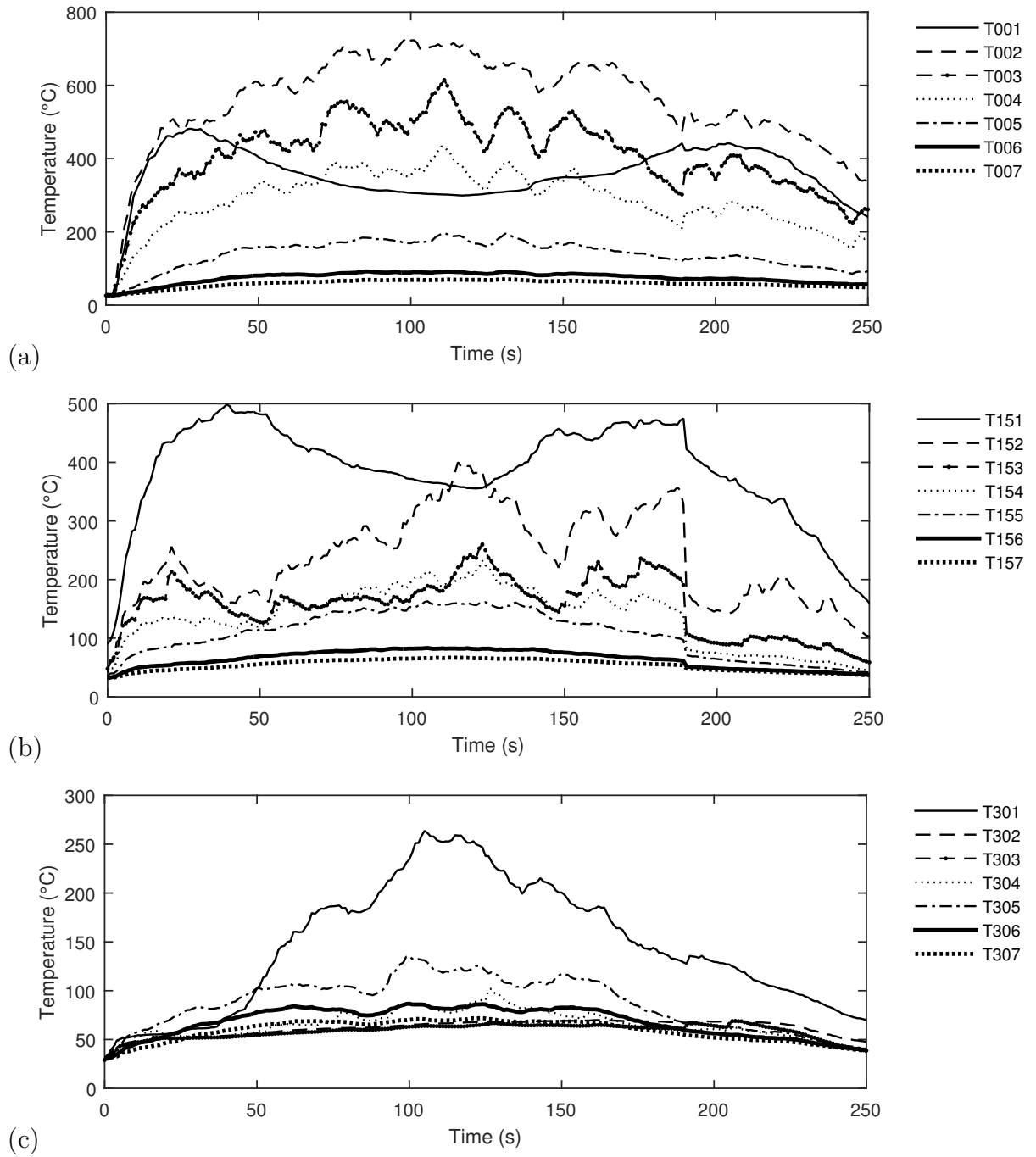


Figure A.7: Average temperature curves for the gasoline flame for (a)  $X/D=0.0$ , and (b)  $X/D=0.25$ , (c)  $X/D=0.50$ .

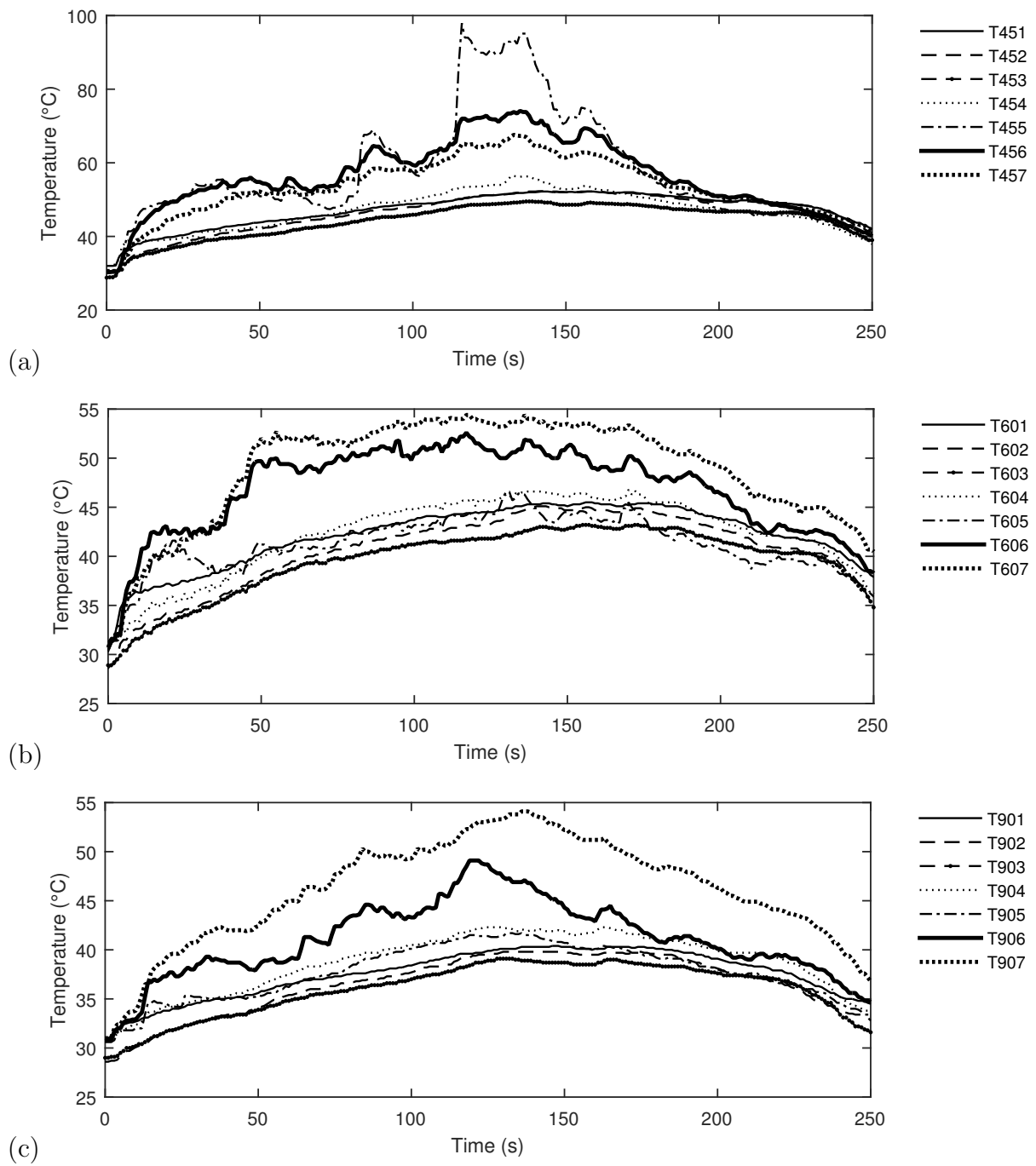


Figure A.8: Average temperature curves for the gasoline flame for (a)  $X/D=0.75$ , and (b)  $X/D=1.00$ , (c)  $X/D=1.50$ .

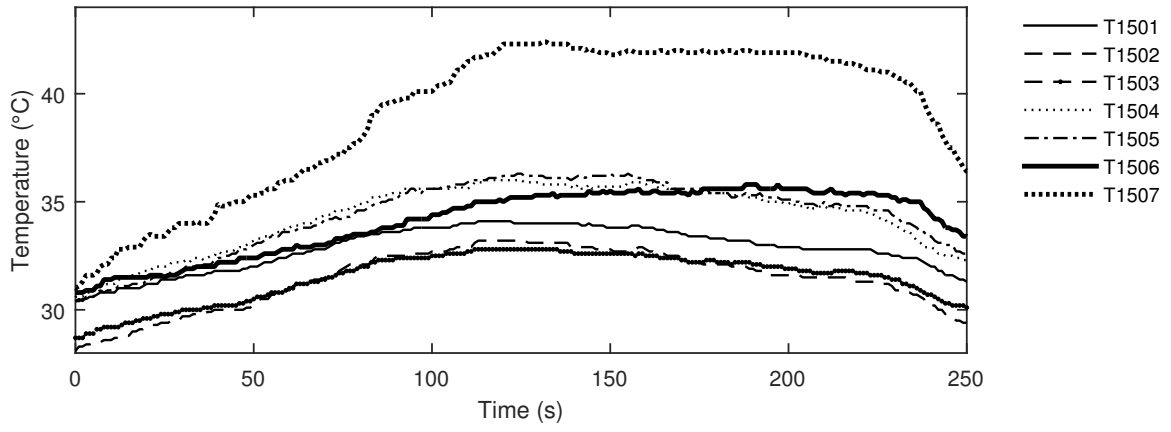


Figure A.9: Average temperature curves for the gasoline flame for  $X/D=2.50$ .